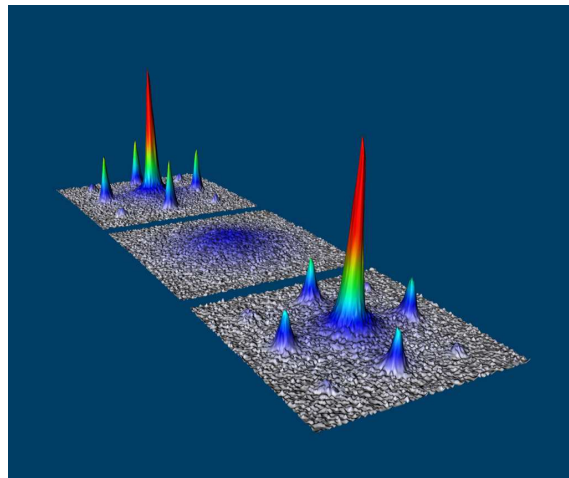


ULTRACOLD ATOMS IN AN OPTICAL LATTICE: A NUMERICAL APPROACH

LODE POLLET



Promotoren:

Dr. STEFAN ROMBOUTS

Prof. Dr. KRIS HEYDE

Proefschrift ingediend tot het behalen van de graad van
Doctor in de Wetenschappen: Natuurkunde

Universiteit Gent

Faculteit Wetenschappen

Vakgroep Subatomaire en Stralingsfysica

Academiejaar 2004-2005



Cover: *Restoring coherence (1)*

Multiple matter wave interference pattern of a quantum gas released from a 3D optical lattice with more than 100.000 occupied lattice sites. From left to right: High contrast interference pattern in the superfluid regime; Quantum phase transition to the Mott Insulator regime with no phase coherence; Restored coherence after the transition back into the superfluid regime.

Courtesy of Prof. Dr. Immanuel Bloch, Ultracold quantum gases, Quantum/Exakt group, Johannes Gutenberg University, Mainz, Germany.

<http://www.physik.uni-mainz.de/quantum/bec/gallery/index.html>

To Leen, Annie and Stephaan

Preface

I wish to thank my parents for having given me the opportunity to spend all my time working on this thesis for so many years. To them, and to my sister I want to dedicate this thesis, for their endless support and love.

I wish to thank my supervisor Dr. Rombouts for the many concepts he has introduced to me. His insight was vital for many of the ideas presented in this work. I also wish to thank my supervisor Professor Kris Heyde for his enthusiastic and inspiring way of talking about physics. I also thank Kris Van Houcke for his very accurate way of working, and for the many questions we posed each other.

I want to thank P. Denteneer and J. Dukelsky for collaborating on a joint project and co-authoring a paper. I thank professor H. T. C. Stoof for allowing me to stay at the university of Utrecht, and professor M. Troyer for having invited me to ETH Zürich. Thanks goes to all former and current members of their groups for sharing so many interesting ideas.

I am also grateful to all professors, post-docs, visitors, technical staff and students in Gent and to everyone playing indoor soccer with me on Wednesdays. To Veerle, Stijn, Pascal, Klaas, Tim and Cristina : a special thanks for the many years of friendship!

The central results of this thesis appeared in:

- L. Pollet, S. Rombouts, K. Heyde, and J. Dukelsky, *Phys. Rev. A* **69**, 043601 (2004).
- L. Pollet, S. M. A. Rombouts, K. Van Houcke, and K. Heyde, *Phys. Rev. E* **70**, 056705 (2004).
- L. Pollet, S. M. A. Rombouts, and P. J. H. Denteneer, *Phys. Rev. Lett.* **93**, 210401 (2004).

In addition, the thesis contains unpublished material which will be submitted for publication soon.

Finally a word on notation: normally we work in units $\hbar = 1$, but when comparison is made with published results where the factors \hbar appear, we have put them too.

Contents

Preface	i
Table of Contents	iii
1 Introduction	1
1.1 Ultracold atoms and optical lattices	1
1.1.1 Bose-Einstein condensation	1
1.1.2 Optical Lattice	4
1.1.3 A new generation of experiments	5
1.2 Quantum Monte Carlo World Line Algorithms	9
1.3 Outline of the thesis	12
2 Bose-Hubbard model	15
2.1 Wannier states	15
2.2 Physics of the Bose-Hubbard model	20
2.3 Mean-field theory	21
2.4 Mott phase	23
2.5 The superfluid phase	25
2.5.1 The definition of superfluidity	25
2.5.2 The Bogoliubov approximation	26
2.6 Continuum Quantum Field Theories	28
2.7 Physics in one dimension	30
2.7.1 Harmonic Fluid approach	30
2.7.2 Tonks-Girardeau gas	31
2.7.3 Can we see strongly interacting bosons as fermions?	32

3	Numerical Renormalization Group	35
3.1	Experimental parameters and results	35
3.2	Numerical Renormalization Group	36
3.2.1	The method	38
3.2.2	Validation	41
3.3	Results	49
3.3.1	Results in one dimension	49
3.3.2	Results in two dimensions	50
3.3.3	Results in three dimensions	52
4	Exact numerical methods	59
4.1	Lanczos diagonalization	59
4.2	Monte Carlo Strategies	61
4.2.1	Monte Carlo Techniques	61
4.2.2	Markov Chains	63
4.2.3	Efficiency	64
4.2.4	Peskun ordering	65
5	Quantum Monte Carlo algorithms	71
5.1	Stochastic Series Expansion: representation	73
5.2	Directed loop algorithm	75
5.2.1	Diagonal update	76
5.2.2	Off-diagonal update	76
5.3	Observables	86
5.4	Application	87
5.5	Worm algorithm : a locally optimal formulation	90
5.6	Is the hybrid-worm algorithm efficient?	93
6	Tonks gas	99
6.1	Experiments	100
6.2	Simulations	102
6.2.1	Homogeneous system	103
6.2.2	Inhomogeneous system.	105
6.3	Conclusions and Outlook	110

7	Canonical algorithms	113
7.1	Canonical Worm algorithm	113
7.1.1	Sampling with a constant number of interactions	115
7.1.2	Sampling with a varying number of interactions	117
7.1.3	Optimizing the sampling parameters	119
7.1.4	Application: the bosonic Hubbard model	120
7.2	Application: study of the Berezinskii-Kosterlitz-Thouless transition .	126
7.3	Canonical or grand-canonical Monte Carlo simulations?	128
8	Mixtures of bosons and fermions in a one-dimensional optical lattice	133
8.1	The Bose-Fermi Hubbard Hamiltonian	134
8.2	General properties of the Bose-Fermi Hubbard Hamiltonian	135
8.3	Canonical boson-fermion worm	137
8.4	Monte Carlo simulations	140
8.4.1	Half filling	140
8.4.2	Doped system	141
8.4.3	Bosons at integer filling	142
8.5	Outlook	143
9	Conclusions	145
A	Bosonizing one-dimensional bosons in a nutshell	149
A.1	Hamiltonian	149
A.2	Correlation function	151
B	Renormalization Group Approach to the superfluid-Mott transition	153
B.1	Commensurate case	153
B.2	Commensurate-Incommensurate transition. Doping	157
C	Nederlandstalige Samenvatting	159
	Bibliography	165

Chapter 1

Introduction

This thesis focuses on two different topics that are hotly debated in present literature, namely on the physics of ultracold bosonic atoms in an optical lattice and on a numerical technique called the quantum Monte Carlo method. It is the hope of many physicists that ultracold atoms in optical lattices provide the ultimate testing ground for many models of condensed matter physics. The first part of the introduction gives a short overview of the experiments on ultracold atoms in an optical lattice. Second, the history of quantum Monte Carlo methods based on the world line representation is discussed. This chapter is mainly intended for the non-specialist reader or for the reader who has experience in only one of the fields. The aim of the present chapter is to show why the problems that are addressed in this work are interesting, and that they are part of the ongoing developments in the field.

1.1 Ultracold atoms and optical lattices

1.1.1 Bose-Einstein condensation

The idea of Bose-Einstein condensation (BEC) dates back to 1925 when A. Einstein predicted the occurrence of a phase transition in a gas of noninteracting atoms, on the basis of a paper by the Indian physicist S. N. Bose. The experimental discovery of superfluidity in liquid helium showed the close connection between condensation and superfluidity. In 1947 Bogoliubov developed the first microscopic theory of weakly-interacting Bose gases, for which it was argued that spin-polarized hydrogen would be a good candidate. Spin-polarized hydrogen was first stabilized

using a high magnetic field gradient to force hydrogen atoms against a cryogenically cooled surface. Interactions with the surface limited the achieved densities, prompting researchers to develop methods for trapping atoms purely magnetically. Laser-based techniques allowed to trap and to cool alkali atoms (but not hydrogen) from the 1980s on. The atoms can be further cooled using evaporative cooling, and this led ultimately to the observation of Bose-Einstein condensation in dilute, ultracold alkali gases in 1995 [1]. In the sequel of the thesis, we will consider atoms that are trapped in a fixed hyperfine level and that form a BEC. These two concepts will briefly be discussed next.

First, we discuss the hyperfine structure of ^{87}Rb atoms. The interaction between the magnetic moment related to the nuclear spin of the atom and the magnetic flux created by the atomic electrons gives rise to the hyperfine structure. Rb atoms have an electronic spin $J = 1/2$ and a nuclear spin $I = 3/2$. The total atomic spin $F \equiv I + J$ is thus $F = 2$ or $F = 1$. The projection m_F on the axis of an external magnetic field is a good quantum number since the Hamiltonian (including the Zeeman effect) commutes with F_z . We can thus label the levels by the hyperfine magnetic numbers. Most experiments have been performed with low magnetic fields. When the small nuclear Zeeman energy is neglected, the energies of various hyperfine sublevels are given as a function of the magnetic-field magnitude B by the Breit-Rabi formula [2]. They are shown in Fig. 1.1. For low magnetic fields, the degeneracy of the $(2F + 1)$ states in the multiplet is lifted by $g_F \mu_B B m_F$ [3], where μ_B is the Bohr magneton and g_F is the Landé g-factor, which is positive for the $F = 2$ state of Rb and negative for the $F = 1$ state. From Fig. 1.1, we see that only the states $F = 2, m_F = 2, 1$ or 0 and $F = 1, m_F = -1$ are low-field seekers (that is, minimum energy is found for minimal magnetic field) and atoms in these states will be attracted to the origin of the trap. Most experiments have been carried out using one of the states, $F = 2, m_F = 2$ and $F = 1, m_F = -1$. In this thesis, the atoms will always be trapped in a fixed hyperfine level and can thus be considered as spinless.

Second, we recall some of the standard results on Bose-Einstein condensates. Quantum effects are expected to arise when the interatomic distance becomes of the

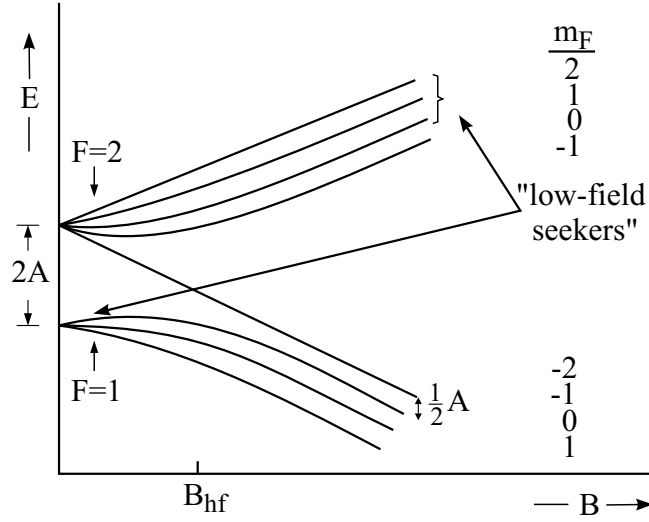


Figure 1.1 The energies of the different hyperfine-Zeeman states as a function of magnetic field. The zero-field splitting $E(F=2) - E(F=1)$ is defined as $2A$. Most experiments have been performed with values B of the magnetic field lower than the value B_{hf} corresponding to the characteristic hyperfine crossover field, $B_{hf} = \frac{A}{\mu_B}$, with μ_B the Bohr magneton. Diagram taken from Ref. [2].

same order as the finite extent of the atoms. More precisely, condensation occurs when the density reaches the value [3]

$$n = \frac{2.6}{\lambda_{dB}^3}, \quad (1.1)$$

where λ_{dB} is the value of the thermal de Broglie wavelength,

$$\lambda_{dB} = \frac{h}{\sqrt{2\pi m k_B T}}, \quad (1.2)$$

with m the mass of the bosons, k_B the Boltzmann constant and T the temperature. The transition temperature is found when the total number N of atoms obeys $k_B T_C = \hbar \bar{\omega} N^{1/3}$, where $\bar{\omega} = (\omega_x \omega_y \omega_z)^{1/3}$ is the geometrical mean of the harmonic trapping frequencies. Bose-Einstein condensation can thus occur in the absence of interactions, in contrast to any other phase transition. A condensate of ultracold bosonic alkali-atoms is described by the Gross-Pitaevskii equation [4],

$$\left(-\frac{\hbar^2}{2m} \nabla^2 + V(r) + g|\psi|^2 \right) \psi = \mu \psi, \quad (1.3)$$

where the energy from the interactions is proportional to $|\psi|^2$ and the coupling constant g is related to the scattering length. The scattering length is a single number that describes the low-energy physics of collisions between ultracold atoms. Trapped atoms experience a harmonic potential,

$$V(r) = \frac{1}{2}m (\omega_x^2 x^2 + \omega_y^2 y^2 + \omega_z^2 z^2). \quad (1.4)$$

When the temperature is sufficiently low and the density sufficiently high, the kinetic energy can be neglected. In this Thomas-Fermi regime the density is given by an inverted parabola,

$$n(r) = n_0 \left(1 - \frac{x^2}{R_x^2} - \frac{y^2}{R_y^2} - \frac{z^2}{R_z^2} \right), \quad (1.5)$$

with $n_0 = N\mu/g$ the density at the center of the condensate, and where the ellipsoidal axes are defined by $\frac{1}{2}m\omega_i^2 R_i^2 = \mu$. The chemical potential is fixed by the normalization of the wavefunction. Outside the ellipsoid, the density is zero.

Specific for a set of one million ^{87}Rb atoms in a typical magnetic trap, the transition occurs at 500 nK. In temperature units we have that the (photonic) recoil energy is 200 nK, the mean-field energy amounts to 100 nK and the zero-point energy in a harmonic well amounts to 5 nK. The size of the condensate is of the order of 10 μm , and the peak density is of the order of 10^{14}cm^{-3} . The zero-field hyperfine splitting is 0.3 K and the energy of the fundamental $ns \rightarrow np$ transition $\sim 10^4$ K. All these numbers show that it is a very good approximation to represent a bosonic alkali atom by a single operator, acting on a single point [5].

1.1.2 Optical Lattice

An electric field E induces a dipole moment of $-er = \epsilon_0\chi_a E$ on an atom with a scalar polarizability $\epsilon_0\chi_a$. The dipole force is strong in a standing wave of light because the intensity changes from a maximum to zero (at the nodes) over a distance of $\lambda/2$ to give a high gradient of intensity, where λ is the wavelength of the laser light. Physically, an atom absorbs light with wavevector k from one beam and emits light with wavevector $-k$ to the other beam due to stimulated emission [3].

The atom acquires a linear momentum of $2k$. For large detunings, the standing wave gives a dipole potential U_{dip} along the z -axis of the form

$$U_{dip} = U_0 \cos^2(kz). \quad (1.6)$$

The intensity U_0 at the maxima is four times the intensity of the individual, counter-propagating beams. For a frequency detuning to the red, a standing wave of light traps atoms at the anti-nodes and gives confinement in the radial direction as in a single beam. When the laser frequency is detuned to the blue the atoms can be trapped in the nodes. A regular array of microscopic dipole traps is called an optical lattice (see Fig. 1.2). For three pairs of counter propagating laser beams aligned along three orthogonal axes a regular cubic lattice of potential wells can be created for large enough frequency detunings and suitable polarizations. The potential wells have a spacing of $\lambda/2$, and the strength of the optical potential can be increased by turning up the laser intensity.

1.1.3 A new generation of experiments

Experimental groups have successfully transferred a quantum gas from a magnetic trap to an optical lattice [6]. It may sound almost too good to be true [7]: the unique controllability over the underlying periodic structure and the interactions between the atoms offer the possibility to simulate a whole range of fundamental phenomena that are impossible to study in real materials. Furthermore, it allows to study the concept of quantum phase transitions in condensed matter physics in an extremely clean way.

Interest in this new generation of experiments was triggered by the theoretical prediction by D. Jaksch *et al.* [8]. Ultracold bosonic atoms loaded in an optical lattice are described by the discrete Bose-Hubbard model, and can undergo a quantum phase transition from a weakly interacting superfluid phase to a strongly interacting Mott insulating phase. This transition was first observed by M. Greiner *et al.* [6]. General properties of the Bose-Hubbard model are presented in Chapter 2, while numerical strategies to obtain exact results for this model are discussed throughout this work.

In the superfluid phase, the physics is dominated by quantum mechanical tunneling through the optical potential barrier. The atoms are delocalized and their densities fluctuate, but there is phase coherence between the atoms on the sites. When the confinement is switched off, bright and narrow interference peaks are observed (see Fig. 1.2). When the optical potential strength is increased by increasing the laser intensity, the tunneling is suppressed. Minimum energy is found for an equal number of atoms on every site, and the system is said to form a Mott state. The well defined density on every site implies that phase coherence is lost. In the interference pattern, the central peak becomes broader and less bright (see Fig. 1.2).

The transition from the superfluid phase to the Mott phase is dominated by the quantum transition point. Although in a quantum phase transition [9] the transition occurs at exactly zero temperature, the long-range behavior of correlation functions at low but finite temperatures can usually be determined. The experiment which is performed at a small but finite temperature, could in principle serve as a clean test for the concept of a quantum phase transition. Quantum phase transitions have also been observed in superconductors and quantum spin chains. The experiment by M. Greiner *et al.* will be discussed in detail in Chapter 3.

Optical lattices have also been used to investigate aspects of one-dimensional quantum gases. One-dimensional quantum systems are completely different from their three-dimensional counterparts: the system becomes strongly interacting in the low-density limit. One-dimensional quantum gases can be produced using two-dimensional optical-lattice potentials [10], since the two-dimensional lattice produces one-dimensional waveguides perpendicular to the axes of the optical lasers. This can be seen in Fig. 1.3. The radial motion is frozen out and only the axial motion persists. When the repulsion between one-dimensional bosonic atoms increases, they undergo a process called fermionization. Atoms tend to separate from one another along the axial direction, mimicking the Pauli principle for fermions. In the limit of infinite repulsion, bosonic atoms behave like (free) fermions in many respects and are said to form a Tonks-Girardeau gas [11]. In the early stages of the experimental challenge of reaching this limit, the values obtained for the repulsion were not high enough [12]. Later, by adding an optical potential along the axial

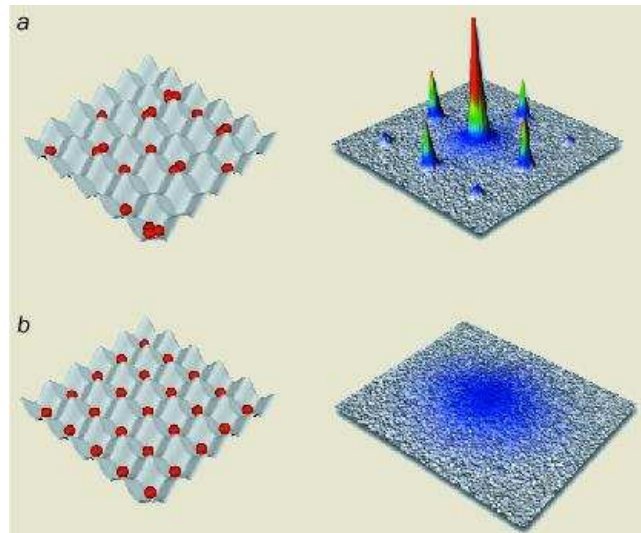


Figure 1.2 (a) In the superfluid phase the phase coherence between the matter waves on the different sites leads to a multiple matter wave interference pattern. (b) In the Mott insulating state each site is filled with a fixed number of atoms, destroying any phase coherence between the sites. The central interference peak becomes broader and less bright. Picture taken from [7].

direction, much higher values for the repulsion strength between the atoms were obtained [13]. In this experiment, as well as in a later experiment without an optical lattice along the axial direction [14], it was claimed that the atoms have entered the Tonks-Girardeau regime. In Chapter 6 we will check numerically whether these experiments are better described by bosons or by fermions.

Bose-Einstein condensates in optical lattices also offer unique opportunities for quantum information processing [7] and eventually building a quantum computer. Atoms in a Mott insulating state can be viewed as a natural quantum register, where each quantum bit is represented by a single atom. There have been ideas on how to address single atoms on different lattice sites [15]. Second, the atoms have to move closer to each other so that their quantum states become entangled. Collisions between ultracold atoms are fully coherent. By applying a time-dependent optical potential, an atom can be transferred to its neighboring site, when the atoms will collide with a definite phase shift which could be set equal to π [16]. The sys-

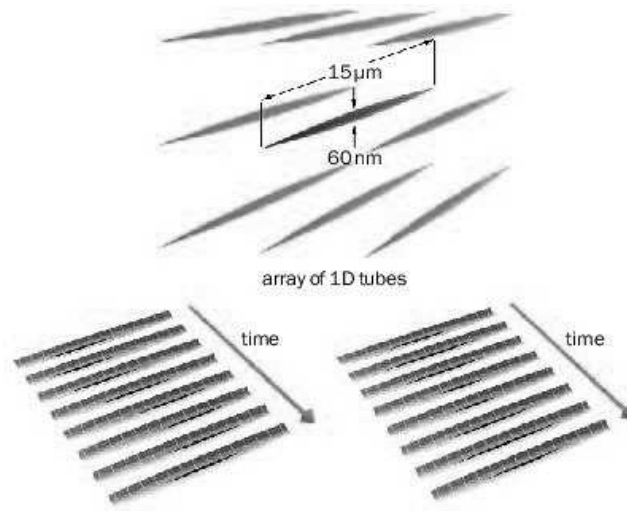


Figure 1.3 Arrays of one-dimensional quantum gases can be created by using two-dimensional lattice potentials. Picture taken from Ref. [7].

tem would constitute a quantum phase gate. Developments in this field are out of the scope of this work.

Fermionic gases have successfully been cooled to the degeneracy temperature. The exclusion principle prevents the existence of a Fermi condensate, but at zero temperature the lowest single-particle energy levels are filled with as many atoms as their spin states will allow. By sweeping the magnetic field across a Feshbach resonance, fermionic atoms can form molecules [17], and it might be possible to study the BCS-BEC crossover between molecules and Cooper pairs [18]. Related to these new and interesting challenges, we will discuss in Chapter 8 a mixture of one-dimensional ultracold bosonic and fermionic atoms. The fermions can then be cooled to lower temperatures using sympathetic cooling by the bosons. The physics of this system is much richer than that of the Bose-Hubbard model. Density waves with a period of twice the lattice spacing are predicted, and there might exist exotic phases with pairing between the bosons and the fermions.

1.2 Quantum Monte Carlo World Line Algorithms

The second important building block of this work is a numerical strategy to model the phenomena introduced in the previous section, since the exact computation of correlation functions in the Bose-Hubbard model is not possible analytically. Two numerical strategies will be introduced in the course of this thesis: first, the numerical renormalization group and second, quantum Monte Carlo methods based on a world line representation. Quantum Monte Carlo is the method of preference for simulating ultracold bosons in an optical lattice, certainly in higher dimensions. In addition, there has been a lot of progress in recent years on how quantum Monte Carlo algorithms can be made more efficient. In this work new algorithms are suggested.

The first systematic use of the Monte Carlo method dates back to World War II and the late forties. Statistical based sampling methods were invented for solving numerical problems concerning random neutron diffusion in fissile material. These simulations ran on the world's first supercomputer, MANIAC (Mathematical Analyzer, Numerical Integrator and Computer) at Los Alamos. In the early 1950s, Metropolis *et al.* introduced a Markov-chain-based dynamic Monte Carlo method for the simulation of simple fluids [19] which was afterwards applied to more complex materials such as spin glasses. Scientists have also thought of tackling quantum physical problems using variational Monte Carlo (Frost, Conroy), diffusion Monte Carlo (Metropolis, Ulam) and Green function Monte Carlo (Kalos). From the 1980s on, the path integral Monte Carlo method by Ceperley proved extremely successful on calculations of liquid ^4He [20]. For discrete quantum models, algorithms based on world lines share with path integral Monte Carlo the idea of mapping the d dimensional quantum path integral to the $d + 1$ dimensional classical path integral [21]. Nowadays, Monte Carlo methods are not only used in (quantum) physics, but in almost every branch of science. From engineering, material science and statistics over economics and finance to biology - Monte Carlo methods are extremely flexible and powerful.

One might ask what a numerical simulation is and why it is called for, as opposed to other theoretical techniques. In physics, the Hilbert space (configuration

space) is generally too large in order to allow exact diagonalization. Instead, exact results for thermodynamic observables are obtained by running a simulation and collecting a sufficient amount of statistics. The numerical technique used in this thesis is called Markov chain Monte Carlo. In a Markov chain the present state depends on its past only through the previous state. A transition rule is defined in order to go from one configuration to another with respect to the weight associated with every configuration. In Monte Carlo integration, we sample the distribution of these unnormalized weights (partition function), albeit in a correlated way. If the simulation runs for a sufficiently long period of time, the estimator for the expectation value of a particular observable is arbitrarily close to its true mean value. The technology and the efficiency of Markov chain Monte Carlo are briefly discussed in Chapter 4 of this thesis.

At the heart of quantum Monte Carlo world line methods lies Suzuki's observation that the path integral of a d -dimensional quantum spin-1/2 system can be mapped onto that of a classical Ising spin in $(d + 1)$ dimensions [21]. Quantum spins are mapped to classical world lines and local updates for quantum spins hopping around can be defined by the Metropolis algorithm [19, 22].

Let us be more specific about what a world line representation is. The Hamiltonian H is written as $H = H_1 + H_2$, where $H_j, j = 1, 2$ is the sum of a commuting two-site problem and solvable. We have here a XXZ Hamiltonian in mind, meaning that $H_j, j = 1, 2$ act on nearest neighbor sites $\langle i, i + 1 \rangle$. Usually one takes H_1 as the sum over all operators where site i is even, and H_2 as the sum over all operators where site i is odd. Using the Trotter decomposition [23], the partition function Z can then be written as

$$\begin{aligned}
 Z &= \text{Tr} [\exp(-\beta H)] = \text{Tr} \left[\exp(-\Delta\tau(H_1 + H_2))^M \right] \\
 &= \text{Tr} [\exp(-\Delta\tau H_1) \exp(-\Delta\tau H_2)]^M + \mathcal{O}(\Delta\tau^2) \\
 &= \sum_{|i_1\rangle, \dots, |i_{2M}\rangle} \langle i_1 | U_1 | i_2 \rangle \langle i_2 | U_2 | i_3 \rangle \cdots \langle i_{2M-1} | U_1 | i_{2M} \rangle \langle i_{2M} | U_2 | i_1 \rangle + \mathcal{O}(\Delta\tau^2),
 \end{aligned} \tag{1.7}$$

where the time step $\Delta\tau = \frac{\beta}{M}$ and $U_i = \exp(-\Delta\tau H_i)$. The insertion of complete basis sets in the last step allows for a graphical interpretation: the state $|i_1\rangle$ evolves in imaginary time (inverse temperature) under the operators U_1 and U_2 . Within each

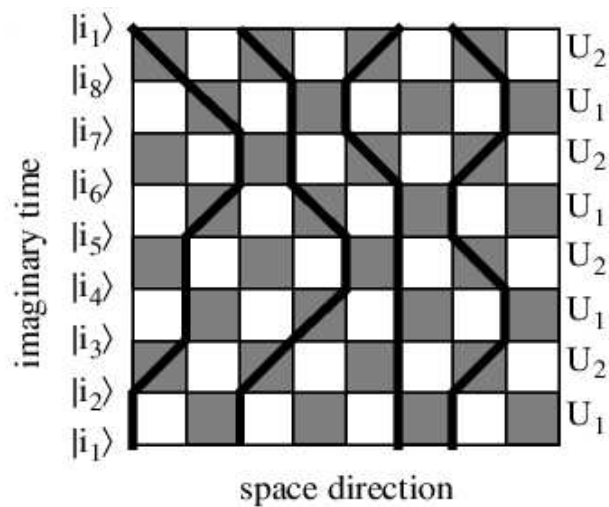


Figure 1.4 The checkerboard decomposition with world lines is a graphical interpretation of the mapping of one-dimensional quantum system to a two-dimensional classical path integral. Figure taken from Ref. [24].

time interval, the operators U_1 and U_2 are applied once, leading to the checkerboard decomposition of Fig. 1.4. Note that more accurate decompositions of the partition function in the same fashion can easily be thought of.

Local updates suffer from critical slowing down near a second order quantum phase transition. Near a first order quantum phase transition one notices the tunneling out of metastable states. In classical Monte Carlo the former was solved by cluster algorithms [25], and there is no reason why the same ideas shouldn't apply to the quantum problem [24]:

- H. Evertz' loop algorithm allows for efficient sampling of quantum spins near a second order phase transition [26]. The loop algorithm is a direct generalization of classical cluster algorithms. For certain models it is probably still the best algorithm at hand. The loop algorithm will not further be discussed in this thesis.
- Continuous time versions of the local update algorithms and the loop algorithm were formulated [27], removing the need for the extrapolation in the discrete time step $\Delta\tau$.

- An alternative was given by the local updates in the stochastic series expansion (high temperature expansion) representation [28, 29], when there is no time discretization error. The algorithm is a generalization of Handscomb's method [30]. In this thesis only continuous time algorithms will be discussed.
- The development of the worm algorithm [31], the operator loop algorithm [32] in the stochastic series expansion and the directed loop algorithm [33] allowed large scale simulations of systems without particle-hole symmetry. All these algorithms sample the distribution of the Green function, and Chapters 5 and 7 are dedicated to these algorithms.
- Flat histogram methods for quantum problems are a first step towards dealing with first order phase transitions [34]. These algorithms are not discussed in this thesis.

There exist many other quantum Monte Carlo algorithms such as variational Monte Carlo, diffusion and Green function Monte Carlo, path integral Monte Carlo, determinantal or auxiliary field quantum Monte Carlo, and many others. These algorithms are out of the scope of this thesis.

1.3 Outline of the thesis

The central aim of the thesis is a numerical approach towards two experiments, namely to the superfluid-Mott phase transition by M. Greiner *et al.* [6] and to the experiment on reaching the Tonks-Girardeau gas in a one-dimensional optical lattice, described by B. Paredes *et al.* [13]. In these experiments, measurements consist of time-of-flight absorption images after the confinement of the system has been switched off. Any theoretical/numerical comparison involves thus a calculation of the momentum distribution of the confined system. In this thesis we focus on a quantitative explanation of these experiments and on the development of efficient numerical methods for the simulation of such systems. The numerical methods are able to calculate quantities like the momentum distribution such that a direct comparison between experiment and simulation becomes feasible.

The physics of both experiments can be modeled by the Bose-Hubbard Hamiltonian, which is discussed in Chapter 2. We discuss a number of analytical approaches to the Bose-Hubbard model, which are all perturbative and do not allow the exact computation of correlation functions. This opens the way for numerical simulations. In Chapter 3, we focus on the superfluid-Mott phase transition using the numerical (real-space) renormalization group. In Chapter 4, Monte Carlo methods are introduced, with special emphasis on their efficiency. In Chapter 5, a quantum Monte Carlo method based on the local sampling of the Green function is discussed, which is used then in Chapter 6 for the study of reaching the Tonks-Girardeau limit. In Chapter 7, a canonical formulation of the quantum Monte Carlo method of Chapter 5 is given. In the mean time, quantum critical properties of the Bose-Hubbard model are studied. In Chapter 8, a mixture of bosons and fermions in a one-dimensional optical lattice is simulated by a direct extension of the canonical Monte Carlo algorithm of Chapter 7.

Chapter 2

Bose-Hubbard model

In this chapter we discuss general properties of the Bose-Hubbard model, which catches the physics of ultracold bosonic atoms in an optical lattice. In section 2.1 the Bose-Hubbard model is derived using a lowest band calculation, while the physical properties of the Hamiltonian are discussed in the following sections.

2.1 Wannier states

The Hamilton operator for ultra-cold bosonic atoms in an external trapping potential V_T reads [2, 4, 35]

$$H = \int d^3r \psi^\dagger(r) \left[-\frac{\hbar^2}{2m} \nabla^2 + V_T(r) + V_0(r) \right] \psi(r) + \frac{1}{2} g_{\text{int}} \int d^3r \psi^\dagger(r) \psi^\dagger(r) \psi(r) \psi(r), \quad (2.1)$$

where m is the mass of the atoms. The external magnetic trapping potential is usually quadratic, while V_0 is an optical lattice potential. The coupling strength $g_{\text{int}} = \frac{4\pi\hbar^2 a_s}{m}$ is related to the three-dimensional s -wave scattering length a_s of the dilute boson gas. The derivation for a one-dimensional optical lattice is given here, but the discussion readily generalizes to the two-dimensional and three-dimensional case as eq.(2.1) factorizes. In order to create a one-dimensional optical lattice, the confinement in the transverse directions must be very tight. The wavefunction in the transverse directions is then nearly Gaussian, and the integration over these directions is immediate. The effective one-dimensional coupling g_{int} reads [36]

$$g_{\text{int}} = \frac{2\hbar^2 a_s}{m a_\perp^2} \frac{1}{1 - A a_s / a_\perp}. \quad (2.2)$$

The first factor is the result one expects by taking the transverse harmonic oscillator length $a_{\perp} = \sqrt{\hbar/m\omega_{\perp}}$ into account. This is however not the whole story: Olshanii has studied the two-body scattering properties in tight waveguides and found that resonances of the form of the second factor in eq.(2.2) can occur where A is a constant of the order of unity [36]. The second factor will be neglected in the remainder of the thesis, since we will consider only applications far away from resonance. This confinement induced resonance can be used to change the interaction strength by tuning the magnetic field, similarly to the objective of using Feshbach resonances, which is based on different physics. Adding an optical lattice along the axial x axis can be done by aligning a laser with wavelength λ creating a potential

$$V_0(x) = V_0 \sin^2(kx), \quad (2.3)$$

with $k = 2\pi/\lambda$. For sufficiently deep laser potentials, we expect the atoms to be periodically localized by the laser potential. We thus expect that a description in terms of localized wavefunctions (Wannier states) around these positions catches the physics and simplifies our goal. The standard approach for this band calculation takes only the kinetic term and the optical potential into account, leading to the Mathieu equation [37]

$$H = -\frac{\hbar^2}{2m} \frac{d^2}{dx^2} + V_0 \sin^2(kx), \quad (2.4)$$

We only dispose of N sites due to the harmonic confinement, but periodic boundary conditions are imposed leading to the quantization of momenta,

$$q = \frac{2\pi l}{\lambda N}, l = 0, 1, \dots, N - 1. \quad (2.5)$$

The Mathieu equation has to be rewritten using dimensionless variables. Under the coordinate change

$$\pi z = kx \quad (2.6)$$

the wavefunction transforms as $\psi \rightarrow \sqrt{2/\lambda}\psi$ and the eigenequation reads

$$\left(-\frac{d^2}{dz^2} + V \sin^2(\pi z) \right) \psi(z) = E\psi(z), \quad (2.7)$$

with $V = \frac{\pi^2 2m}{\hbar^2 k^2} V_0 = \frac{\pi^2}{E_R} V_0$. The (photonic) recoil energy E_R is used as energy scale. For ^{87}Rb atoms subject to a laser with a wavelength of $\lambda = 854\text{nm}$, the recoil

energy amounts to $\approx 150\text{nK}$ in temperature units or $\approx 3k\text{Hz}$ in frequency units. In dimensionless units the above eigenequation has periodicity 1. The Bloch theorem then states that the eigenfunctions have the form

$$\psi_{n,q}(z) = e^{iqz}u_{n,q}(z), \quad (2.8)$$

with q the (dimensionless) momenta and $u_{n,q}(z)$ a function that has the same periodicity as the eigenequation. The subscript n denotes the band index, but we will further on show that for all our purposes it suffices to take the lowest band only. Every band consists of N energy levels. The band-index is suppressed from now on. The resulting eigenequation

$$-\left(\frac{d}{dz} + iq\right)^2 u_q(z) + V \sin^2(\pi z)u_q(z) = \tilde{E}_q u_q(z), \quad (2.9)$$

with \tilde{E}_q the rescaled eigenvalue corresponding to wavevector q , is most easily solved by going to momentum space, $u_q(z) = \sum_m A_m(q)e^{imz}$. For every q we have to diagonalize a tridiagonal matrix. This can also be seen as follows: the set of operators $\{\frac{d}{dz}, 2\pi \sin(2\pi z), 2\pi \cos(2\pi z)\}$ forms a realization of the $E(2)$ algebra with generators $e^{i(q+m)z}$ [38–40]. The tridiagonal matrix representation in the basis spanned by these generators results from writing the cosine as a sum of two exponentials, $\sin^2(\pi z) \sim -\cos(2\pi z) = -1/2(e^{i2\pi z} + e^{-i2\pi z})$. Illustrative examples for the real and imaginary part of the Bloch functions $u_q(z)$ are shown in Fig. 2.1 and in Fig.2.2.

Having obtained the N Bloch eigenstates, we are interested in the Wannier states. Wannier states are a linear combination of Bloch states, but are no eigenstates of the periodic Hamiltonian. The Wannier state localized at site R_i is real and can be obtained from the Bloch state by

$$w(x - R_i) = \frac{1}{\sqrt{N}} \sum_q e^{iq(x-R_i)} u_q(x). \quad (2.10)$$

This equation is only determined up to an arbitrary phase. We chose to perform the summation coherently [41]. In the literature, the Wannier function is often approximated by a Gaussian wavefunction,

$$w(x - R_i) = \left(\frac{1}{\pi a_{\text{ax}}}\right)^{1/4} e^{-(x-R_i)^2/2a_{\text{ax}}^2}, \quad (2.11)$$

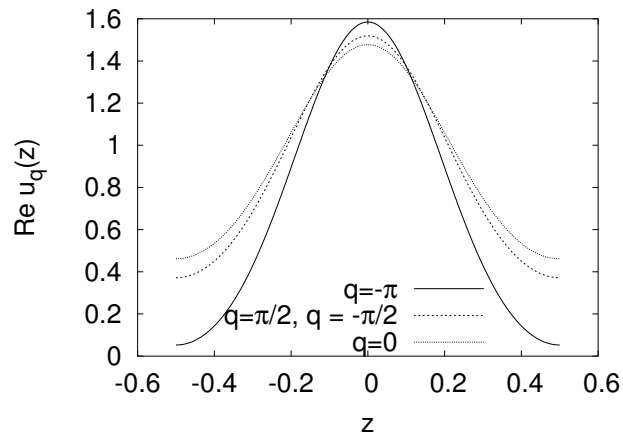


Figure 2.1 Real part of the Bloch functions for a lattice of 4 sites and optical potential $V_0 = 4.6E_R$. The momenta q are dimensionless and the functions are shown over the length of one period.

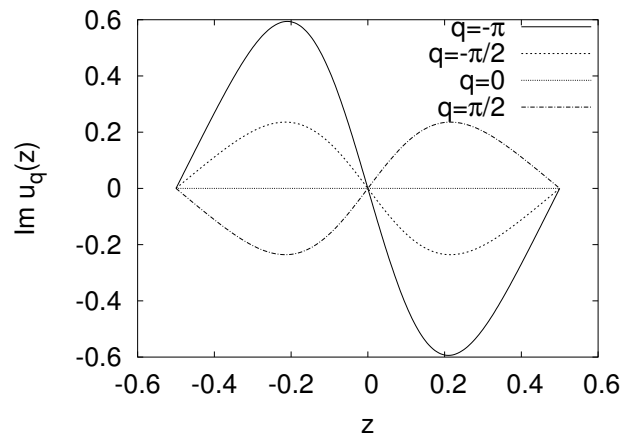


Figure 2.2 Imaginary part of the Bloch functions for a lattice of 4 sites and optical potential $V_0 = 4.6E_R$. The momenta q are dimensionless and the functions are shown over the length of one period.

where $a_{\text{ax}} = \sqrt{\hbar/m\omega_{\text{ax}}}$ is the harmonic oscillator length in the axial direction. This result becomes exact in the limit of infinitely deep lattices.

The field operators are expanded in the lowest Wannier state (with respect to the usual commutation relations) [8]

$$\psi(x) = \sum_i b_i w(x - R_i), \quad (2.12)$$

where the operator b_i annihilates a boson at site i localized at position R_i . In this basis the Hamiltonian reduces to the Bose-Hubbard model,

$$H = -t \sum_{\langle i,j \rangle} b_i^\dagger b_j + \frac{1}{2} U \sum_i n_i(n_i - 1) - \mu \sum_i n_i, \quad (2.13)$$

which is a discrete model since the relevant degrees of freedom correspond to atoms tunneling between the potential minima. An overview of the physical properties and the notational conventions is postponed to the next section, while here we relate the effective parameters of the Bose-Hubbard model to the microscopic and experimental parameters. The strength of the on-site repulsion term U is given by

$$U = g_{\text{int}} \int dx w^4(x), \quad (2.14)$$

where the coupling in dimensionless units reads $g_{\text{int}} = \frac{2a_s \lambda}{a_\perp^3}$. When the Gaussian approximation for the Wannier function is used, the values of U slightly differ from the ones obtained here. Repulsion between neighboring sites is an order of magnitude smaller than on-site repulsion and is neglected.

The matrix element that describes hopping between two sites i and j is given by

$$t_{i,j} = - \int dx w^*(x - x_i) \left(-\frac{d^2}{dx^2} + V_0 \sin^2(kx) \right) w(x - x_j), \quad (2.15)$$

which reduces to

$$t_{i,j} = -\frac{1}{N} \sum_q \tilde{E}_q e^{-iq(x_i - x_j)}, \quad (2.16)$$

i.e. the Fourier transform of the Bloch dispersion relation. It can also be obtained exactly from the known solution of the Mathieu equation. Second-nearest hopping should be two orders of magnitude smaller and can be neglected. We assume that all matrix elements between nearest-neighbor sites $\langle i, j \rangle$ are equal, $t_{\langle i, j \rangle} = t$. At this stage we also take the magnetic trapping into account,

$$\epsilon_i = \int dx V_T(x) |w(x - x_i)|^2 \approx V_T(x_i). \quad (2.17)$$

The physics of the Bose-Hubbard model is not influenced by the Wannier state. However, the finite extent of the localized wave-functions does play a role when comparison is made with the experiment. For instance, the density matrix in coordinate space (single particle Green function) is

$$\mathcal{G}(x, y) = \langle \psi^\dagger(x) \psi(y) \rangle = \sum_{m, n} w(x - x_m) w(y - x_n) \langle b_m^\dagger b_n \rangle. \quad (2.18)$$

Consequently, the momentum distribution relevant for the experiment is

$$n(p) = |w(p)|^2 \sum_{m, n} e^{ip(m-n)} \langle b_m^\dagger b_n \rangle. \quad (2.19)$$

The envelope $|w(p)|^2$ can be quite different for various optical potentials, as is shown in Fig. 2.3.

2.2 Physics of the Bose-Hubbard model

In this section the general properties of the homogeneous Bose-Hubbard model,

$$H = -t \sum_{\langle i, j \rangle} b_i^\dagger b_j + \frac{1}{2} U \sum_i n_i(n_i - 1) - \mu \sum_i n_i, \quad (2.20)$$

are discussed. The lattice is square in d dimensions and consists of L^d sites with periodic boundary conditions. The sum $\langle i, j \rangle$ in the first term is over nearest neighbor sites only. The operator b_i^\dagger creates a boson on lattice site i while b_i removes it. The first term in eq.(2.20) is a kinetic term with tunneling amplitude t . The operator n_i counts the local density on site i . The second term in eq.(2.20) describes the on-site repulsion between atoms and is therefore proportional to the pair density $n_i(n_i - 1)$. The operator N denotes the total number operator, $N = \sum_i n_i$. We take

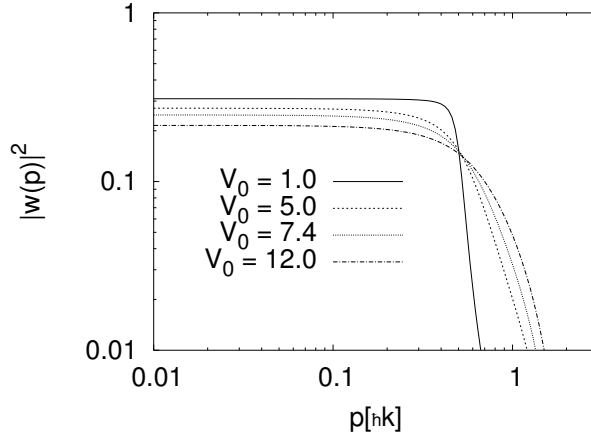


Figure 2.3 Profiles of the momentum distribution squared of the Wannier functions for various optical potential strengths ($E_R = 1$) on log-log scale.

the distance a between adjacent sites equal to $a = 1$. The total density is set by the chemical potential μ . We also define the coordination number $z = 2d$ as the number of neighbors of each site. The energy scale is determined by setting $t = 1$.

We will, to a large extent, follow the approach by Sachdev [9]. The aim is to introduce the phases of the Bose-Hubbard model, the notion of quantum phase transitions and to rederive analytical approximations that are needed for comparison with the numerical results in the next chapters. The literature on this subject is vast, and there exist many well-advanced successful analytical approaches to tackle the problem we just set. Each one has its own merits and successes for specific parameter regimes and dimensions. The main goal is to derive all analytical results we need in the future chapters at the expense of an eclectic presentation.

2.3 Mean-field theory

The Bose-Hubbard model of eq.(2.20) is invariant under a global $U(1)$ transformation,

$$b_i \rightarrow b_i e^{i\phi}. \quad (2.21)$$

Hence, we expect a quantum phase transition in t/U between a state in which the $U(1)$ symmetry is unbroken to one in which it is broken. These phases are the Mott and the superfluid phases, respectively. The nomenclature will be justified in the sequel. The conserved quantity associated with the $U(1)$ symmetry is the total number of bosons, N .

The mean-field Hamiltonian looks for the best possible sum of single site Hamiltonians,

$$H_{MF} = \sum_i \left(-\mu n_i + \frac{U}{2} n_i(n_i - 1) - \psi^* b_i - \psi b_i^\dagger \right). \quad (2.22)$$

The sites are effectively decoupled, while the variational parameter ψ represents the influence of the neighboring fields and it needs to be determined self-consistently. A nonzero ψ explicitly breaks the $U(1)$ symmetry and does not conserve the total number of bosons N . Symmetric phases appear for $\psi = 0$. The mean-field ground-state wavefunction is a direct product of Fock states over all sites. The parameter ψ is chosen to be uniform over all sites, assuming that the groundstate does not spontaneously break translational symmetry. With E_0 the expectation value of the Hamiltonian of eq.(2.20) calculated with the true wavefunction and E_{MF} the expectation value of the mean-field Hamiltonian calculated with the mean-field wavefunction, we arrive at

$$\frac{E_0}{L} = \frac{E_{MF}}{L} - zt \langle b^\dagger \rangle \langle b \rangle + \langle b \rangle \psi^* + \langle b^\dagger \rangle \psi. \quad (2.23)$$

This equation needs to be minimized over variations in ψ , leading to

$$\psi = zt \langle b \rangle. \quad (2.24)$$

This result is valid on mean-field level only. It identifies the order parameter of the phase transition.

More generally (e.g. for non-uniform systems), the above approach amounts to determining the best possible Gutzwiller ansatz wave function [42],

$$|\Psi\rangle = \prod_{i=1}^{L^d} \left(\sum_{n=0}^{\infty} f_n^{(i)} |n_i\rangle \right), \quad (2.25)$$

where the coefficients $f_n^{(i)}$ need to be determined self-consistently in a variational sense.

A different but completely equivalent approach is the decoupling approximation,

$$(b_i - \psi) (b_j^\dagger - \psi) = b_i b_j^\dagger - \psi b_i \psi b_j^\dagger + \psi^2, \quad (2.26)$$

for nearest neighbor sites $\langle i, j \rangle$ and with ψ the expectation value of the operator $\langle b \rangle$,

$$\psi = \langle b \rangle = \langle b^\dagger \rangle = \sqrt{n}. \quad (2.27)$$

In order to obtain the mean-field phase diagram, we can diagonalize the mean-field Hamiltonian exactly with a particle number cut-off that is high enough. Alternatively, since the numerical analysis shows that the superfluid-Mott quantum phase transition is second order, the energy can be approximated as

$$E^{(2)} = a_0 + a_2 \psi^2 + \mathcal{O}(\psi^4), \quad (2.28)$$

where a_0 and a_2 are perturbation coefficients. Minimum energy is found for $\psi = 0$ when $a_2 > 0$ and for $\psi \neq 0$ when $a_2 < 0$. By the Ginzburg-Landau argument, the phase boundary is found for $a_2 = 0$ [43]. The resulting phase diagram is shown in Fig. 2.4.

2.4 Mott phase

In the grand-canonical ensemble, mean-field theory is exact at $t = 0$ and the sites are effectively decoupled. The groundstate wavefunction is an exact eigenstate of N and can be written in the form $|n_i = \nu(\mu/U)\rangle$ with

$$\nu(\mu/U) = \begin{cases} 0 & \mu/U < 0 \\ 1 & 0 < \mu/U < 1 \\ \vdots & \\ n & n-1 < \mu/U < n \end{cases}.$$

Each site has exactly the same number of bosons which jumps discontinuously whenever μ/U goes through a positive integer. Excitations are gapped. Let us now

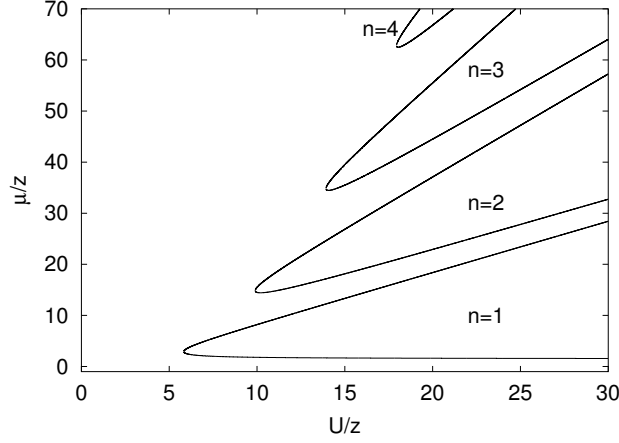


Figure 2.4 The mean-field phase diagram for $t = 1$. The Mott lobes, indicated by integer numbers, are surrounded by a superfluid.

turn on a weak value of t/U , such that $0 < t/U \ll 1$. Although the wavefunction is no longer a product wavefunction, we still have $\langle n_i \rangle = \nu(\mu/U)$ in the Mott phase [9]. This integer density is indicated in Fig. 2.4 and is the result of the energy gap Δ and the commutator $[H, N] = 0$. The Mott phase is incompressible, $\frac{\partial N}{\partial \mu} = 0$.

The elementary excitations are quasiparticles and quasiholes with a dispersion up to first order in t/U [43]

$$E_{p/h} = E_{p/h}^{(0)} - 2t \sum_j^d \cos(k_j a) \approx \Delta_{p/h} + \frac{k^2}{2m^*}, \quad (2.29)$$

with $E_p^{(0)} = Un_i - \mu$ and $E_h^{(0)} = -U(n_i - 1) + \mu$ the energies for an extra particle and hole on site i in the limit $t/U = 0$. The effective mass $m^* = 1/(2t)$ is found after Taylor expanding around the minimum $k = 0$. Suppose the lowest energy excitation is given by a particle excitation, $E_p < E_h$ (when $n_i < \frac{1}{2} + \mu/U$). The physical picture is that of a dilute gas of infinitely long-living quasiparticles with effective mass m^* , gap Δ_p and some positive scattering amplitude $a_* > 0$ (see the positive coefficient in front of the ψ^4 term in eq.(2.40)). The gas with density n_p is hence always stable with energy [44, 45]

$$E_p = (\Delta_p - \mu) n_p + \frac{2\pi a_* \hbar^2}{m_*} n_p^2. \quad (2.30)$$

When the chemical potential μ increases and becomes larger than the gap Δ_p , the particles condense (while the holes remain gapped) and we expect a density driven mean-field like quantum phase transition to a superfluid (see eq. 2.41). When the holes are the lowest energy excitations, the same considerations are still valid with the roles of the particles and the holes interchanged. However, when (to first order) the chemical potential equals $\mu = \frac{1}{2} + \mu/U$, particles and holes become gapless at the same time and behave like particles and anti-particles [46]. We can thus expect a ‘relativistic’ theory (see eq. 2.40, with the first term set to zero).

2.5 The superfluid phase

In this section we look at the other limiting phase of the Bose-Hubbard model, namely the superfluid phase. The superfluid phase is described by the Bogoliubov approximation, but first we define what is understood under the notion of ‘superfluidity’.

2.5.1 The definition of superfluidity

Long before Bose-Einstein condensation had been realized in the alkali gases, liquid ^4He had been the only system where the phenomena of ‘condensation’ and ‘superfluidity’ could be investigated. Helium is the only permanent liquid available in nature, and it becomes a solid only after increasing the pressure. Below the temperature of $T_\lambda = 2.17\text{K}$, helium becomes a superfluid. This temperature is very close to the critical value of $T_c = 3.3\text{K}$ needed for condensation (for a non-interacting system), which suggests that the phenomena of ‘superfluidity’ and ‘Bose-Einstein condensation’ are related, but not exactly the same: as temperature approaches zero, the superfluid density tends to the total density in liquid helium, while the condensate contains only 10% of all particles [47].

A precise definition of the notions ‘condensate’ and ‘superfluid’ goes as follows [2, 48]. If the one-body density matrix has a macroscopic eigenvalue N_0 , then this eigenmode with wavefunction $\phi_0(x) = e^{i\theta(x)}|\phi_0(x)|$ is the condensate. With the condensate phase $\theta(x)$ there is an irrotational velocity field associated, $v_0(x) = \frac{\hbar}{m}\nabla\theta(x)$. The velocity $v_S(x)$ of the superfluid flow is now exactly this ve-

locity $v_S(x) = v_0(x)$. The superfluid velocity can be considered as a classical quantity, since it characterizes the behavior of a macroscopic number of particles (the condensate). For systems with Galilean invariance, the superfluid fraction equals the total boson density (cf. liquid He). On a lattice this is of course not true any more.

According to the Mermin-Hohenberg-Wagner theorem [49], a continuous symmetry cannot be broken in one quantum dimension. Hence, a condensate cannot exist in one dimension. As will be discussed in section 2.7, we should speak of a Luttinger liquid instead, with a linear dispersion $\omega = uk$. The linear dispersion means that at zero temperature, we have a true superfluid in the Landau sense [4]. Even stronger, in a Luttinger Liquid correlations decay algebraically, and one often speaks of quasi long-range order. For these reasons we also denote the Luttinger Liquid phase in one dimension as a superfluid phase.

2.5.2 The Bogoliubov approximation

Let us apply the Fourier transformation

$$b_i = \frac{1}{\sqrt{L^d}} \sum_k b_k e^{ik \cdot r_i} \quad (2.31)$$

to the Bose-Hubbard Hamiltonian of eq.(2.20), yielding

$$H = \sum_k (-\epsilon_k - \mu) b_k^\dagger b_k + \frac{U}{2L^d} \sum_{k,k',k'',k'''} b_k^\dagger b_{k'}^\dagger b_{k''} b_{k'''} \delta_{k+k',k''+k'''}, \quad (2.32)$$

where the single particle energies are given by $\epsilon_k = 2t \sum_{j=1}^d \cos(k_j a)$ and where the δ implies momentum conservation up to factors of 2π .

When $U = 0$ we have a gas of non-interacting bosons, meaning that all bosons are in the condensate state $k = 0$ in the thermodynamic limit at zero temperature. The superfluid density equals the condensate density in this limit.

If we now turn on a small U/t , we can assume that the number N_0 of bosons in the condensate is still macroscopic, and we can approximate the creation operator and

the annihilation operator of bosons in the $k = 0$ state by c - numbers,

$$\begin{aligned} N_0 &= \langle b_0^\dagger b_0 \rangle \approx \langle b_0 b_0^\dagger \rangle, \\ \langle b_0^\dagger \rangle &\approx \langle b_0 \rangle \approx \sqrt{N_0}. \end{aligned} \quad (2.33)$$

This lies at the heart of the Bogoliubov approximation, where in addition to the above approximation a small fluctuation is taken into account,

$$\begin{aligned} b_0^\dagger &\rightarrow \sqrt{N_0} + b_0^\dagger \\ b_0 &\rightarrow \sqrt{N_0} + b_0. \end{aligned} \quad (2.34)$$

The new operators b_0 and b_0^\dagger are small and treated on equal footing as $b_k, k \neq 0$. Again we have explicitly broken number conservation. Minimization of the Hamiltonian with respect to the number N_0 of bosons in the condensate (or its density $n_0 = N_0/L$) imposes that the terms of the Hamiltonian linear in the operators b_0 and b_0^\dagger must vanish. This relates the chemical potential to the condensate density,

$$\mu = Un_0 - zt. \quad (2.35)$$

The Hamiltonian is restricted to (zero and) second order,

$$\begin{aligned} H^{(2)} &= -\frac{1}{2}Un_0N_0 - \frac{1}{2}\sum_k (\bar{\epsilon}_k + Un_0) \\ &\quad + \frac{1}{2}\sum_k \begin{pmatrix} b_k^\dagger & b_{-k} \end{pmatrix} \begin{bmatrix} \bar{\epsilon}_k + Un_0 & Un_0 \\ Un_0 & \bar{\epsilon}_k + Un_0 \end{bmatrix} \begin{pmatrix} b_k \\ b_{-k}^\dagger \end{pmatrix}, \end{aligned} \quad (2.36)$$

with the shifted energies $\bar{\epsilon}_k = 2z - \epsilon_k$. The Hamiltonian $H^{(2)}$ is quadratic in the operators b_k and can be diagonalized by a Bogoliubov transformation,

$$\begin{pmatrix} a_k \\ a_{-k}^\dagger \end{pmatrix} = \begin{bmatrix} u_k & v_k \\ v_k^* & u_k^* \end{bmatrix} \begin{pmatrix} b_k \\ b_{-k}^* \end{pmatrix}, \quad (2.37)$$

under the constraint $|u_k|^2 - |v_k|^2 = 1$ in order to fulfill the commutation relation $[a_k, a_l^\dagger] = \delta_{k,l}$. The computation simplifies by setting $u_k = \alpha_k \cosh \xi_k$ and $v_k = \alpha_k \sinh \xi_k$. The requirement that the final Hamiltonian is diagonal, $H = \sum_k \hbar\omega_k a_k^\dagger a_k$, leads to the solution

$$\begin{aligned} \hbar\omega_k &= \sqrt{\bar{\epsilon}_k^2 + 2Un_0\bar{\epsilon}_k} \\ |v_k^2| = |u_k^2| - 1 &= \frac{1}{2} \left(\frac{\bar{\epsilon}_k + Un_0}{\hbar\omega_k} - 1 \right). \end{aligned} \quad (2.38)$$

In agreement with the Goldstone theorem, the spectrum is gapless. The linear spectrum automatically gives rise to the critical velocity

$$v_s = \lim_{k \rightarrow 0} \frac{\partial \omega_k}{\partial k} = \frac{1}{\hbar} \sqrt{U n_0 z t} \neq 0, \quad (2.39)$$

justifying the nomenclature 'superfluid' in the Landau sense. Finally, the Bogoliubov approximation fails to see the Mott phase.

The perturbation theories we have seen in the last two sections, are in principle only valid for $t/U \ll 1$ (in the Mott phase) and for $U/t \ll 1$ (Bogoliubov approximation in the superfluid phase). In addition, the Bogoliubov theory does not predict the transition to the Mott phase. This is one of the main motivations for a numerical approach to the Bose-Hubbard model.

2.6 Continuum Quantum Field Theories

After having investigated both phases of the Bose-Hubbard model independently, we focus on the quantum phase transition, where correlation functions can diverge with certain critical exponents. Close to the transition the long-range low-energy physics is characterized by universal behavior, while the underlying lattice description is only reflected in the prefactors and the short-range behavior - a property seen in all quantum phase transitions. The critical exponents can be classified according to various universality classes (effective quantum field theories), while large-scale numerics offer the possibility to compute them. The study of critical properties is another main motivation for going to numerical calculations.

The most general mean-field Lagrangian consistent with the $U(1)$ symmetry, time reversal and spatial inversion reads [9]

$$\begin{aligned} Z &= \int \mathcal{D}\Psi^*(x, \tau) \mathcal{D}\Psi(x, \tau) \exp \left(- \int d^d x \int d\tau \mathcal{L}[\Psi^*, \Psi] \right) \\ \mathcal{L}[\Psi^*, \Psi] &= - \frac{\partial r}{\partial \mu} \Psi^* \frac{\partial \Psi}{\partial \tau} + |\partial_\tau \Psi|^2 + c^2 |\nabla \Psi|^2 + r |\Psi|^2 + \frac{u}{2} |\Psi|^4 + \dots \end{aligned} \quad (2.40)$$

The insulator phase is found for $r \gg 0$, while the superfluid is found for $r \ll 0$. The phase transition belongs to a different universality class whether the first term is zero or not.

- At the tip of the Mott lobes in Fig. 2.4, the coefficient $\frac{\partial r}{\partial \mu} = 0$. The transition is then driven by phase fluctuations and there is no density change. The transition belongs to the $O(2)$ quantum rotor class, or the $(d + 1)$ dimensional XY class. In one dimension ($d = 1$), this transition is of the Berezinskii-Kosterlitz-Thouless type [50, 51] and has a profound impact on the phase diagram. We will further discuss this case in section 2.7 and in Appendix B. F. Alet and E. Sørensen have recently studied the classical $(2+1)$ dimensional case using the Villain representation and a classical worm algorithm [52]. They obtained the critical exponent for the correlation length $\nu = 0.670(3)$, in perfect agreement with the 3D XY model. The dynamic exponent relating the quantum time direction to a z spatial (classical) directions equals $z = 1$ in this case.
- When $\frac{\partial r}{\partial \mu} \neq 0$, the second term in eq.(2.40) is irrelevant. The field Ψ is rescaled by $\sqrt{-\frac{\partial r}{\partial \mu}}$ such that the normalization is set by the Berry phase [53]. Close to the transition we have $r = -\mu$ up to a constant, and the continuum quantum field theory reads

$$\mathcal{L}[\Psi^*, \Psi] = \Psi^* \frac{\partial \Psi}{\partial \tau} + \frac{1}{2m} |\nabla \Psi|^2 - \mu |\Psi|^2 + \frac{u}{2} |\Psi|^4. \quad (2.41)$$

The particle and hole excitations have different energies. The transition is driven by density fluctuations and is called the generic transition. The dynamic exponent equals $z = 2$. The density can be regarded as an order parameter (in the grand-canonical ensemble) and one finds in one dimension [9]

$$\langle \psi^\dagger \psi \rangle = \begin{cases} \frac{1}{\pi} (2m(\mu - \mu_c))^{1/2}, & \mu > 0 \\ 0, & \mu < 0 \end{cases}. \quad (2.42)$$

with μ_c the value of the chemical potential at the phase transition (in eq.(2.41) equal to 0 by rescaling). In contrast, the density is to first order linear in the chemical potential in three dimensions, as it follows from a perturbative treatment of eq.(2.41). The case of one dimension ($d = 1$) is further discussed in the next section and in the appendix. F. Alet and E. Sørensen also studied the generic phase transition in the classical analog of $(d = 2)$ dimensions [52] and obtained for the critical exponent of the correlation length a value that strongly confirmed the mean-field one ($\nu = 1/2$). Other critical exponents

were also found close to their mean-field values. It was found that universal behavior sets in for extremely large lattices only, and their simulations were plagued by finite size effects that are reminiscent of a first order phase transition.

2.7 Physics in one dimension

Physics in one dimension is completely different from physics in three dimensions. The failure of Fermi Liquid theory is the best known example hereof. For one-dimensional bosons, the physics is also completely different and some of its properties are briefly highlighted. We succinctly mention the harmonic fluid approach and we end the section with introducing the notion of a Tonks-Girardeau gas.

2.7.1 Harmonic Fluid approach

Using Haldane's description [54, 55] (bosonization techniques), the long-range low-energy physics of the one-dimensional Bose-Hubbard Hamiltonian of eq.(2.20) is described by the sine-Gordon Hamiltonian H_{SG} (see Appendix A) [56–58]

$$H_{SG} = \frac{1}{2\pi} \int dx \left[uK(\nabla\theta(x))^2 + \frac{u}{K}(\nabla\phi(x))^2 \right] + g \int dx \cos(2\phi(x) - \delta x), \quad (2.43)$$

in terms of the phase $\phi(x)$ and density fields $\theta(x)$. The first two terms describe Gaussian fluctuations and should be regarded as the one-dimensional equivalent of Fermi liquid theory. The $\cos(2\phi(x))$ is a consequence of the periodicity of the lattice, while δ is the mismatch between the mean density n_0 and an integer times the inverse lattice spacing $1/a$. The Luttinger parameters u and K are phenomenological and relate to the second sound velocity and the compressibility. They can be related to the microscopic parameters of the underlying Hamiltonian via numerics or for exactly solvable models such as the Lieb-Liniger model only [59]. The long-range behavior of equal time correlation functions can be expressed in terms of the Luttinger parameter K (see Appendix A),

$$\begin{aligned} \langle \psi^\dagger(x)\psi(0) \rangle &\sim |x|^{-1/(2K)} \\ \langle n(x)n(0) \rangle &\sim x^{-2} + A \cos(x\pi n_0)|x|^{-2K}, \end{aligned} \quad (2.44)$$

with A a non-universal constant. Bosonization techniques do in general not allow for the computation of prefactors. In the sine-Gordon Hamiltonian, the Berezinskii-Kosterlitz-Thouless transition is found for $\delta = 0$, $K = 2$, while the generic transition to the first Mott lobe occurs when δ is varied with $K \leq 2$. It is at these values that the third term in eq.(2.43) becomes relevant (see also Appendix B). At the value $K = 1$ the system becomes a Tonks-Girardeau gas [11].

2.7.2 Tonks-Girardeau gas

In order to explain what a Tonks-Girardeau gas is, let us go back to the Bose-Hubbard Hamiltonian, eq.(2.20). When the repulsion U/t becomes infinite, minimum energy is reached for zero potential energy. This means that every site is either not occupied or singly occupied. The effective statistics consist of zero or single occupation, just like the statistics for fermions. The Bose-Hubbard model is thus reduced to a model of non-interacting hard-core bosons.

The Jordan-Wigner transformation maps hard-core bosons (or Pauli-matrices) to spinless fermions [60],

$$\begin{aligned} b_m &= K_m c_m \\ K_m &= \exp \left[i\pi \sum_{l < m} n_l \right] = \prod_{l < m} (1 - 2n_l). \end{aligned} \quad (2.45)$$

The operator K_m turns the hard-core boson operator b_m into the fermionic c_m . The value of the operator K_m is $+1(-1)$ if the total number of fermions to the left of site m is even (odd). The Jordan-Wigner transformation can be inverted,

$$c_m = K_m^{-1} b_m = K_m b_m = \left(\prod_{l < m} (1 - 2n_l) \right) b_m. \quad (2.46)$$

Here, we follow the derivation by M. Cazalilla [61]. Consider the N-particle bra

$$|\Phi\rangle = \sum_{\{m_i\}} \Phi_F(x_{m_1}, \dots, x_{m_N}) c_{m_1}^\dagger \cdots c_{m_N}^\dagger |0\rangle, \quad (2.47)$$

where $|0\rangle$ is the vacuum state. The N-particle bra can however equally well be written as

$$|\Phi\rangle = \sum_{\{m_i\}} \Phi_B(x_{m_1}, \dots, x_{m_N}) b_{m_1}^\dagger \cdots b_{m_N}^\dagger |0\rangle, \quad (2.48)$$

with

$$\begin{aligned}\Phi_B(x_{m_1}, \dots, x_{m_N}) &= A(x_{m_1}, \dots, x_{m_N}) \Phi_F(x_{m_1}, \dots, x_{m_N}) \\ &= |\Phi_F(x_{m_1}, \dots, x_{m_N})|\end{aligned}\quad (2.49)$$

the wave-function of a system of hard-core bosons, where the fully antisymmetric prefactor $A(x_{m_1}, \dots, x_{m_N}) = \prod_{i < j} \text{sgn}(x_{m_i} - x_{m_j})$ has been introduced. For an even number N of fermions with periodic boundary conditions, the corresponding bosonic theory must have antiperiodic boundary conditions. For an odd number of particles, nothing changes. We have thus arrived at the Bose-Fermi mapping by Girardeau in first quantization [11, 62].

Summarizing, Tonks bosons behave like fermions in many respects. Observables that can be expressed in terms of the magnitude of the many-body wave function have the same expectation value irrespective of whether working with spinless fermions or hard-core bosons. This is the case for the energy and the density. For other quantities like the Green function, this correspondence is no longer valid and one needs to take the phase factors back into account. When one expects that hard-core bosons are a good approximation to the solution of a bosonic Hamiltonian, one can apply the concept of ‘fermionization’: the Hamiltonian is solved using fermions, and for quantities like the Green function, the phase factors are taken back into account.

2.7.3 Can we see strongly interacting bosons as fermions?

M. Cazalilla has derived an effective Hamiltonian of interacting fermions up to order t^2/U , valid when approaching the Tonks-Girardeau limit [63]. First, he splitted the Hilbert space in two complementary subspaces, $\mathcal{H} = \mathcal{H}_P \oplus \mathcal{H}_Q$, with P a projector operator on the subspace \mathcal{H}_P of states with maximum occupation $n_i \leq 1$ for all sites i , and $Q = 1 - P$ the complementary projector operator. Using the perturbation expansion,

$$H_{\text{eff}} = PHP - PHQ \frac{1}{QHQ} QHP + \dots, \quad (2.50)$$

the effective Hamiltonian reads to order $\mathcal{O}(t^2/U)$

$$\begin{aligned}
 H_{\text{eff}} \approx & \frac{-t}{2} \sum_{i=1}^L (b_{i+1}^\dagger b_i + b_i^\dagger b_{i+1}) \\
 & - \frac{t^2}{2U} \sum_{i=1}^L (b_{i+1}^\dagger b_{i-1} + b_{i-1}^\dagger b_{i+1} + n_{i+1} + n_{i-1}) n_i,
 \end{aligned} \tag{2.51}$$

in terms of the hard-core bosonic operators b_i . By the Jordan-Wigner transformation of eq.(2.45), the effective Hamiltonian for fermions is obtained, but we only need the expression in terms of hard-core bosons in Chapter 6.

Chapter 3

Numerical Renormalization Group

The main purpose of this chapter is to quantitatively explain the Greiner experiment on the quantum phase transition from a superfluid to a Mott insulator [6], which we already briefly mentioned in section 1.1.3. The numerical renormalization group (or real-space renormalization group) is introduced and validated. The chapter ends with large-scale simulations for which the parameters are chosen close to the experimental ones. ‘Renormalization’ needs to be understood here as the systematic thinning out of degrees of freedom leading to effective Hamiltonians, but it does not involve an ultraviolet nor an infrared energy cutoff in the degrees of freedom.

3.1 Experimental parameters and results

Spin-polarized samples of laser-cooled ^{87}Rb atoms in the ($F = 2, m_F = 2$) state are cooled such that a spherically symmetric Bose-Einstein condensate with a Thomas-Fermi diameter of $26\mu\text{m}$ results consisting of 2×10^5 atoms [6]. The atoms are confined in a magnetic trap with final trapping frequencies $\nu = 24$ Hz. Three optical standing waves are aligned orthogonal to each other, leading to a three-dimensional optical potential

$$V(x, y, z) = V_0 (\sin^2(kx) + \sin^2(ky) + \sin^2(kz)) . \quad (3.1)$$

Here, $k = 2\pi/\lambda$ denotes the wavevector of the laser light with wavelength $\lambda = 852$ nm. V_0 is the maximum potential depth of a single standing wave laser field, and it is measured in units of the recoil energy $E_R = \hbar^2 k^2 / 2m$. Potential depths up to

$V_0 = 22E_R$ can be reached in the experiment, corresponding to a confining potential frequency for a single atom of $\nu = 30$ kHz. The condensate has been distributed over more than 150.000 lattice sites (potential minima) (~ 65 lattice sites in a single direction) with an average atom number of up to 2.5 atoms per lattice site in the center. The physics of the system is no longer described by the Gross-Pitaevskii equation, but the system is now strongly-interacting and correctly described by the Bose-Hubbard Hamiltonian of eq.(3.2).

By suddenly turning off the trapping potential, the atomic wavefunctions are allowed to expand freely and interfere with each other. Absorption images of this gas correspond to the momentum distribution of the original system. Deep in the superfluid regime, phase coherence between the sites leads to a high-contrast three dimensional interference pattern.

Greiner *et al.* [6] increased the optical potential depth, and studied the interference pattern (see Fig. 3.1). For low potentials, the higher-order interference maxima increase with raising potential height. At a potential depth of around $13E_R$, the interference maxima no longer increase and an incoherent background of atoms gains more and more strength. At a potential depth of $22E_R$, no interference pattern is visible at all. Greiner *et al.* associated the disappearance of the interference peaks (together with resonances in the excitation spectrum) with the cross-over from the superfluid to the Mott regime. The confining quadratic potential cuts off any diverging correlation length, making that a true quantum phase transition does not exist in a trapped system. All one can speak of, is a cross-over between different regions or domains. A potential depth of $13E_R$ corresponds to a ratio $U/t = 36$ for the effective parameters in the Bose-Hubbard model (see eq.(3.2)), which is close to the mean-field value of $U/t = z \times 5.8 = 6 \times 5.8$ (where $z = 2d$ is the coordination number) for the phase-transition in the thermodynamic limit (see Fig. 2.4).

3.2 Numerical Renormalization Group

From Chapter 2 we know that the physics of the system seen in the experiment by Greiner *et al.* [6] is correctly described by the Bose-Hubbard Hamiltonian. We know that we can directly relate the experimental parameters to the effective pa-

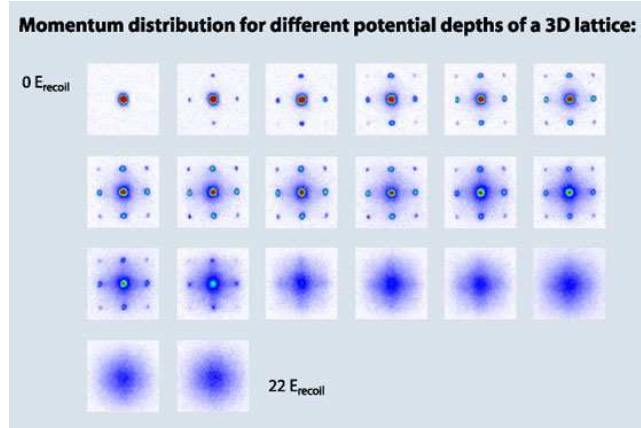


Figure 3.1 Absorption images of matter waves obtained after suddenly releasing the atoms from an optical potential with potential depths V_0 ranging from $0E_R$ to $22E_R$ after a time of flight of 15 ms. Figure taken from Ref. [6].

rameters of the Bose-Hubbard Hamiltonian. In this section, we forget about the relation between the effective parameters and the experimentally controllable ones. Instead, we work directly with the effective parameters and concentrate on the Bose-Hubbard Hamiltonian which we repeat here for convenience,

$$H = -t \sum_{\langle i,j \rangle} b_i^\dagger b_j + \frac{1}{2} U \sum_i n_i(n_i - 1) + \sum_i (\epsilon_i - \mu) n_i. \quad (3.2)$$

The notational conventions and units have been explained in Chapter 2, while the ϵ_i term represents the harmonic magnetic trapping and can be added to the chemical potential μ to form $\mu_i = \epsilon_i - \mu$. In case of a site dependent μ_i we speak of the inhomogeneous or confined model, in case of a uniform μ we speak of the unconfined or homogeneous model.

The main objective is to study the superfluid-Mott quantum phase transition in the homogeneous case, and the cross-over in the trapped or inhomogeneous case. We have seen in Chapter 2 that mean-field theory fails to adequately describe one of the phases. It is thus necessary to take more correlations into account. Second, we wish to use a numerical method that can handle the large lattice sizes. If this would be at the cost of some precision then that would be acceptable, seen the experimental uncertainty range of about $3E_R$ on the cross-over. These observa-

tions led us to a variation of the numerical renormalization group method (NRG) or real-space renormalization group method, despite its poor reputation in dealing with long-range interactions between fermions [64, 65], but we found it useful for bosonic systems (see also [66]).

The basic philosophy of the NRG method we propose, consists of extending one-site mean-field theory to larger blocks, following the idea of the renormalization group method. A fully variational method is obtained which incorporates correlations beyond mean-field at low computational cost and which is able, unlike mean-field theory, to accurately describe the different phases of the Mott-superfluid transition. A disadvantage of the method is the breaking of number conservation during the intermediate steps of the renormalization procedure. In the final step particle number should be restored in principle, but this restoration is only partial when an insufficient amount of states are kept during the model space truncation.

3.2.1 The method

The starting point of the analysis is the Gutzwiller variational ansatz [43, 67] leading to a decoupling of the individual lattice sites and to a mean-field theory. Recall from Chapter 2 that this assumption can be described by the following substitution:

$$b_i^\dagger b_j \Rightarrow \psi_j b_i^\dagger + \psi_i^* b_j - \psi_j \psi_i^*, \quad (3.3)$$

with $\psi_i \equiv \langle b_i \rangle$. This leads to a model where particle number symmetry can be broken, and that can exhibit a superfluid and a Mott-insulator behavior.

In order to obtain a higher accuracy, we extend the mean-field approximation to a renormalization group procedure by taking more correlations into account. It works as follows. Just as in mean-field, first break down the entire lattice to single sites and solve the problem for each site separately. The Hilbert space is truncated so that only a few basis states are kept on every site. In NRG this state selection is based on energy solely, meaning that we keep the N_s eigenstates corresponding to the N_s lowest energy eigenvalues. The two sites are combined now to form a

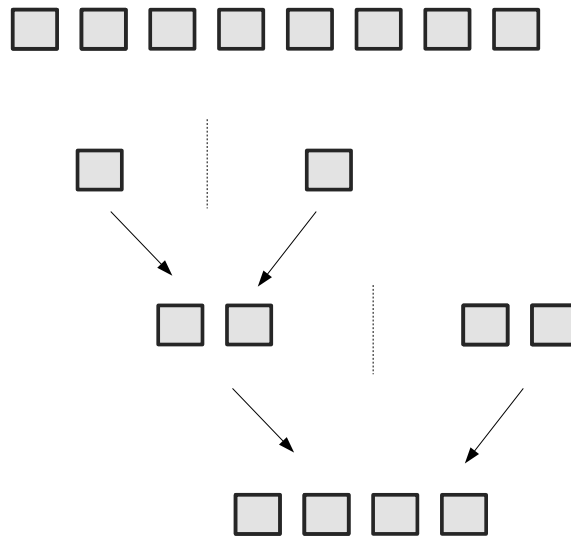


Figure 3.2 The entire lattice is first broken up into individual sites. The mean-field problem is solved for them. The sites are then combined to form small blocks, which are then combined to form larger blocks until the entire lattice is rebuilt.

small block. At this stage, the mean-field approximation (3.3) for the hopping term between the two sites can be canceled by adding a term $(\psi_i^* - b_i^\dagger)(\psi_j - b_j)$, after which the Hamiltonian for the two sites becomes

$$H_{12} = H_1 + H_2 + \sum_{i \in 1, j \in 2} (\psi_i^* - b_i^\dagger)(\psi_j - b_j) + \text{h.c.} \quad (3.4)$$

Here, H_1 and H_2 denote the Hamiltonians of the left and right site, respectively, and the sum runs over adjacent sites that each belong to a different block. In this first step, just the two sites 1 and 2 are meant. The Hamiltonian H_{12} is diagonalized in the space spanned by the product states which are constructed from the individual basis states of each site. After diagonalization, only a few states are kept again. Physical observables require a rotation, since we have performed a basis change. The procedure repeats itself: the small blocks can be joined to form larger blocks which will themselves be the building blocks of still larger blocks etc. The renormalization procedure is explained in Fig. 3.2.

The NRG procedure is very similar to the density matrix renormalization group (DMRG) [68–71]. The main differences are that in DMRG the selection of the states

is based on the eigenvalues of the density matrix instead of on the lowest energy values, and secondly that in NRG one combines blocks (exploiting symmetry), while in DMRG one extends the blocks site by site. In NRG one performs one calculation till the lattice is entirely built up, while in DMRG one sweeps again through the lattice till convergence is obtained. DMRG yields results with a higher accuracy, but its computational time and memory cost requirements are beyond current computer power for dimensions higher than one.

A new idea is that we improve on the standard NRG procedure by adding source terms to the Hamiltonian on the edges of the blocks. These terms compensate for the interaction with the other blocks in a mean-field way. In this way, the Hamiltonian of the local block feels already an average contribution of the blocks that have not yet accounted for, and that have a non-local influence on the block under consideration. After the two joining blocks are taken together, these terms need to be extracted again. If it were possible to work in an infinite Hilbert space the net effect of these source terms would be zero, but in a truncated space the calculation depends on the values of these terms. E.g. suppose we are looking for a Mott phase and these source terms are set to finite values, then we will not find the Mott phase if the source term yields contributions to states higher than the cut-off. This surely will be the case near the boundary of the Mott lobe in a homogeneous system. We have also tried to apply improved periodic boundary conditions by use of such source terms, contrary to DMRG where one usually adopts open boundary conditions. (In general, periodic boundary conditions are easier for finite-size scaling.) We will come back to the issue of source terms in the section on validation.

For the evaluation of some operators such as the total number operator squared N^2 , the contribution from the cross-terms between the two building blocks has to be taken into account. So, more than a simple rotation is needed in this case, and contributions from the total number operator N must be taken into account. Schematically, $\langle N_{12}^2 \rangle = \langle N_1^2 \rangle + \langle N_2^2 \rangle + 2\langle N_1 N_2 \rangle$, in which the indices 1, 2 indicate the two joining blocks.

One can obtain the one-body density matrix in coordinate space with the mean-

field+NRG method, but at a low accuracy because correlations $b_i^\dagger b_j$ are inaccurate when i is not the first site of the renormalization procedure, and we need the entire matrix for a confined system. However, we are able to directly calculate the diagonal of the momentum density operator $n_{k,k} \equiv n_k$ (in one dimension),

$$\begin{aligned} n_k &= \sum_{i,j} e^{-ik(i-j)} b_i^\dagger b_j \\ &= \sum_{i \in L, j \in R} \cos(k(i-j)) b_i^\dagger b_j. \end{aligned} \quad (3.5)$$

Here we sum over all sites of the blocks, easing the problem encountered with the one-body density matrix in coordinate space. This operator can be rewritten as

$$\begin{aligned} n_k &= \sum_{i \in L, j \in R} \cos(ki) \cos(kj) b_i^\dagger b_j + \sin(ki) \sin(kj) b_i^\dagger b_j \\ &= \left(\sum_{i \in L} \cos(ki) b_i^\dagger \right) \left(\sum_{j \in R} \cos(kj) b_j \right) \\ &\quad + \left(\sum_{i \in L} \sin(ki) b_i^\dagger \right) \left(\sum_{j \in R} \sin(kj) b_j \right) \\ &= C_{k_L}^\dagger C_{k_R} + S_{k_L}^\dagger S_{k_R}. \end{aligned} \quad (3.6)$$

Hence we have to keep track of linear combinations of the creation b_i^\dagger and annihilation b_i operators. The parts in which both sites i and j belong to the same block (left(L) or right(R)) have been omitted, since their updating consists only of a rotation to the newly truncated basis. When the sites belong to different blocks, there is a contribution of the cross-term just as with the operator N^2 , but it still suffices to update the C and S operators. The extension to higher dimensions of eq.(3.6) is straightforward. We normalize the Fourier transform by adding pre-factors $\frac{1}{L}$ such that the trace of the density matrix in momentum space yields the number of particles in the system.

3.2.2 Validation

In this section we consider a small lattice in one dimension in the absence of any kind of disorder.

Table 3.1 Comparison of the energies (E_{16} and E_{32}) per site obtained by the mean-field+NRG method for a modest number of states (16 and 32) kept after each diagonalization with the results E_L of a Lanczos diagonalization procedure for a small lattice of 8 sites in 1 dimension. The deviations (D_{16} and D_{32}) are indicated and can be made smaller by keeping more states after each diagonalization. The mean-field values are in the last column.

U	μ	E_L	E_{16}	$D_{16}(\%)$	E_{32}	$D_{32}(\%)$	E_{MF}
2.0	-0.5	-1.359	-1.337	1.57	-1.347	0.91	-1.24
4.0	0.7	-0.932	-0.901	3.38	-0.914	1.99	-0.78
6.0	1.8	-0.656	-0.612	6.65	-0.635	3.15	-0.44
8.0	2.5	-0.494	-0.467	5.60	-0.483	2.40	-0.27
10.0	3.5	-0.397	-0.382	3.53	-0.392	1.09	-0.10
12.0	4.0	-0.331	-0.324	2.35	-0.330	0.31	0.00
14.0	5.0	-0.284	-0.283	0.50	-0.284	0.23	0.00
16.0	6.0	-0.249	-0.247	0.38	-0.248	0.07	0.00
18.0	7.0	-0.221	-0.221	0.30	-0.222	0.04	0.00
20.0	15.2	-0.199	-0.181	8.70	-0.199	0.17	0.00

We have checked the code by comparing the resulting energies to direct Lanczos diagonalization values for a lattice containing 8 sites in one dimension. The one dimensional Bose-Hubbard model with periodic boundaries is a worst-case scenario for our mean-field+NRG procedure. The results are summarized in Table 3.1. The parameters in the table vary from a superfluid phase to a Mott phase. As expected, very deep in a Mott phase or in a superfluid phase we obtain a very good accuracy. Note that the Lanczos diagonalization was performed with a fixed boson number, while in the mean-field+NRG we adjusted the chemical potential in order to fix the density. The deviations should be interpreted accordingly.

We have checked observables like the local density n_i and local compressibility $\kappa_i = \sqrt{\langle n_i^2 \rangle - \langle n_i \rangle^2}$ against ground state results obtained with the directed loop quantum Monte Carlo algorithm in the stochastic series expansion representation for larger lattices [32]. Because the calculation of the momentum distribution seems most critical, we have explicitly shown in Fig. 3.3 the good agreement between the calculation of the momentum distribution with the renormalization group and the stochastic series expansion method for a superfluid and a Mott phase. The stochastic series expansion method is explained in full detail in the chapter 5. So we have

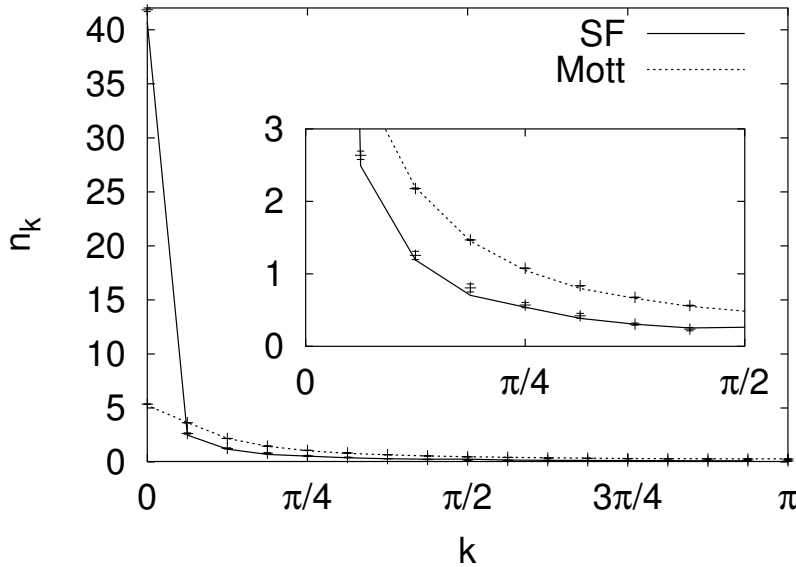


Figure 3.3 Checking the momentum distribution obtained with mean-field+NRG to a stochastic series expansion calculation for an unconfined system in one dimension of 32 sites. Calculations have been done for a system in the Mott phase ($U = 6, \mu = 2$, dashed line) and for a system in the superfluid phase ($U = 2, \mu = 1$, full line). The errors on the stochastic series expansion data points are shown but very small. In the inset, the mean-field+NRG data points are connected by a full line in the SF phase and by a dashed line in the Mott phase, while "+" signs with error bars indicate the stochastic series expansion data points.

shown that the method presented above gives correct results.

The parameter N_s that fixes how many states are kept in the truncation determines the accuracy of the results. As we have seen in Table 3.1 energies can decrease by increasing N_s , while for observables like the local density the fluctuations become smaller. We have examined how the grand-canonical potential Φ decreases when N_s is increased in the upper part of Fig. 3.4 for a system of $L = 1024$ sites (so that finite-size effects can be filtered out of this discussion) in the superfluid phase but very close to the generic Mott phase transition. This corresponds to the worst case scenario for our method. Inclusion of just a few states leads to a rapid decrease in the grand-canonical potential, but once more than 20 states are kept, the potential decreases only very gradually. The exact result $\Phi/L = -1.917(2)$ in Fig. 3.4 was

again obtained by the stochastic series expansion method, while with $N_s = 40$ we reached $\Phi/L = -1.90$. Without source terms, we found that the calculated average grand-canonical potential per site was $\Phi/L = -1.87$ with $N_s = 40$, giving further evidence of the usefulness of the source terms. It is the sweeping property of the DMRG algorithm that could improve the results here substantially, something we tried to avoid from the onset since this property is computationally too costly in higher dimensions. The discrepancy with the exact result in Fig. 3.4 reduces rather slowly at higher values of N_s , primarily because of the effects of block extension (reflected in the curves of the local densities and local energies in Fig. 3.5 for the same effect) and complications due to the periodic boundary conditions. The exact result should be recovered in the limit of N_s equal to the dimension of the Fock space for each block. In addition, for a system that is already deep in one of both phases, the mean-field+NRG method converges very rapidly to the exact result, as the energy curve shows in the lower part of Fig. 3.4 for a system in the Mott phase. Here, the energy and grand potential differ only by a constant.

On the other hand, the parameter N_s largely determines the required computer time: observables scale as N_s^2 per lattice site in memory cost, and the most time consuming operation is the rotation of variables, which scales as N_s^6 (multiplication of matrices of order N_s^2). All our calculations have been performed on a Pentium IV, 1.6GHz or a Pentium III, each with 500MB RAM. Larger lattices and higher values of N_s can straightforwardly be implemented on more performant hardware, but requiring that all occupation numbers of the truncated states are arbitrarily small on the one hand and on the other hand wishing to study large lattices in high dimensions near a quantum phase transition is still not achievable.

One of the crucial parameters of the method is the source term that is inserted at the boundary of each block. If we set it to zero, our method reduces to the standard NRG method. It can be seen in Fig. 3.5 that the fluctuations can be damped much better in a superfluid phase if we set the source term equal to the mean-field expectation value of the operator c_i , while the total energy deviates 0.9% from to the exact result instead of 1.4% without the source terms. For a homogeneous model in the thermodynamic limit, the value of $\langle c_i \rangle$ should be site-independent and the

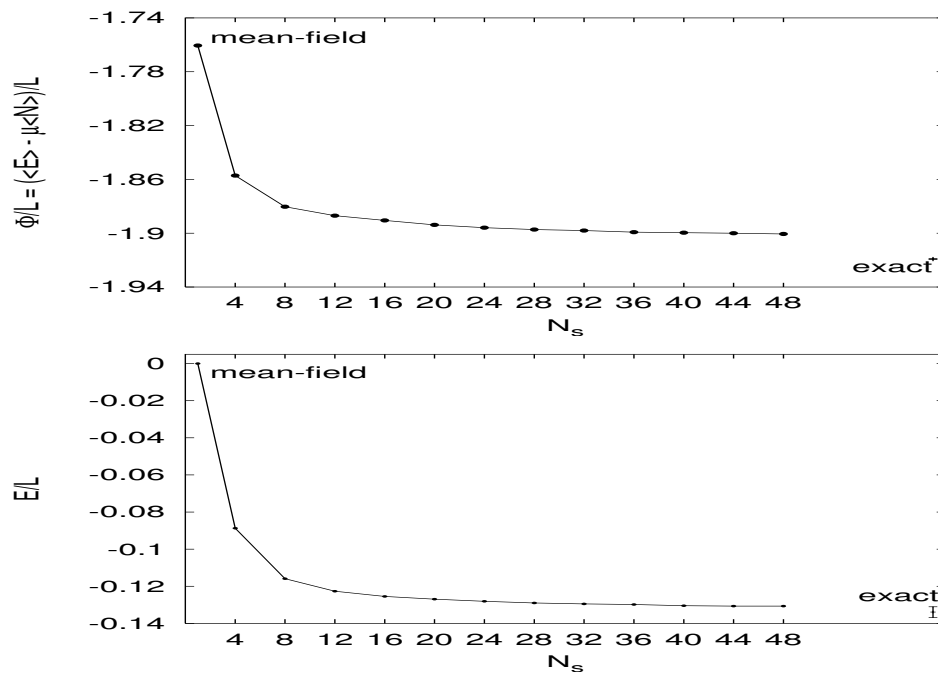


Figure 3.4 Upper: The system is variational in the average grand-canonical potential per site $\Phi/L = (\langle E \rangle - \mu \langle N \rangle)/L$. As the number of kept states N_s is increased, the grand-canonical potential decreases. The full line is a guide to the eye. The parameters are chosen such that the system is near a generic phase transition on the superfluid side ($U = 4, \mu = 1, L = 1024$). This corresponds to the worst case scenario for our method. The mean-field ($N_s = 1$) and exact (corresponding to $N_s = \infty$) results are indicated. Lower: The exponential convergence of the energy is shown. The system is deep in the Mott phase with parameters $U = 30, \mu = 16$ and $L = 1024$.

source terms should be chosen equal as well.

As argued in the previous section, the source terms are optional and need to be chosen carefully. We already know that a Mott phase can only be found if $[H, N] = 0$ (see Ref. [9]), where H denotes the Hamiltonian with renormalized parameters. Source terms might violate this condition near a Mott-superfluid transition. The addition of source terms might lead to an incorrect prediction of a superfluid phase when the compensation of the source terms in the renormalization scheme is not complete. The source terms could yield contributions to states that are thrown away after truncation of the Hilbert space and these contributions can be quite large when the parameter N_s is chosen too low. This might lead to an incorrect value of the transition point. In addition, even if the transition point of a generic Mott-superfluid phase transition was known exactly, and we would study the superfluid side of this transition, the source terms should still be chosen carefully. This can be understood as follows: any net contribution of a source term will deal with long-range correlations in the same way as mean-field does, and we know that the correlators predicted by mean-field are only valid in $d = 3$ dimensions. E.g. the density is a valid order parameter for the generic Mott-superfluid transition [9], with (see eq.(2.42))

$$n \sim \begin{cases} \mu^{1/2} & d = 1 \\ \mu & d = 3 \end{cases}.$$

Briefly said, the source terms would in one and two dimensions lead to an improved mean-field theory, in the sense that the correlators would approximately have the same exponents as in mean-field theory and the Mott lobe would extend a little bit farther into parameter space. This is explained in Fig. 3.6. When N_s is large enough, these possible dangers become less severe. In the confined case, any long-range correlations are effectively cut off and the addition of source terms is always expected to improve the calculations, as has been verified.

It was tempting to study what happens if the blocks were extended by a single site only. That leads to the same number of diagonalizations but more rotations are needed. For the unconfined case, this yielded quite good results, often smoother than in the block renormalization case. However, for the confined case this proce-

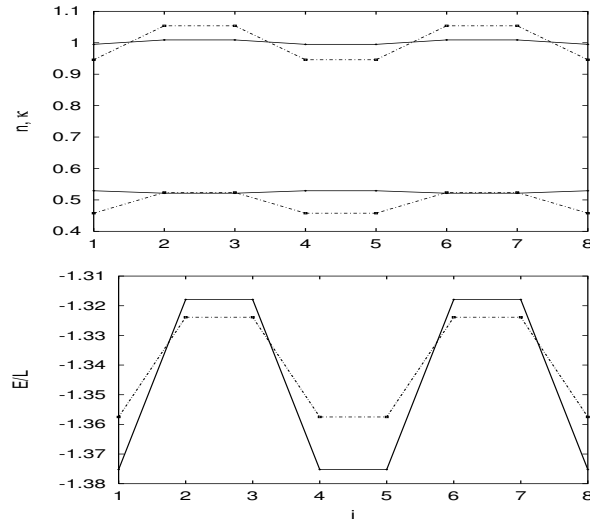


Figure 3.5 The figure shows how source terms can improve the calculations. Local energy per site E_L , local compressibility κ_i and local density n_i from bottom to top are plotted as a function of the lattice index i for a homogeneous model of 8 sites in a superfluid phase ($U = 2, \mu = -0.5$, the same values as the upper row in Table 3.1). The dashed line has source terms set to zero, while for the full line they are set to their mean-field values.

cedure did not produce regions with integer density and should hence only be used with great care.

The mean-field+NRG procedure offers a substantial improvement over mean-field results. The mean-field transition between the superfluid phase and the Mott phase is independent of the dimension of the system and is located at $U_c/z \approx 5.83$, while a DMRG [72] study locates it at $U_c/z \approx 3.36$ in one dimension and a strong-coupling expansion [73] locates it at $U_c/z \approx 4.18$ in two dimensions. We have performed a simulation at $U/z = 5.0$ in one, two and three dimensions. While mean-field theory predicts a superfluid phase (calculation yields $\langle c \rangle = 0.496$) the true phase should be a Mott phase in one and two dimensions, which is confirmed by our mean-field+NRG calculation. We even found a Mott phase in three dimensions. These results can be seen in Fig. 3.7 where the local density and local compressibility are shown. The local compressibility is nonzero in Fig. 3.7 due to finite-size effects but it scales to zero when the system size is increased to infinity.

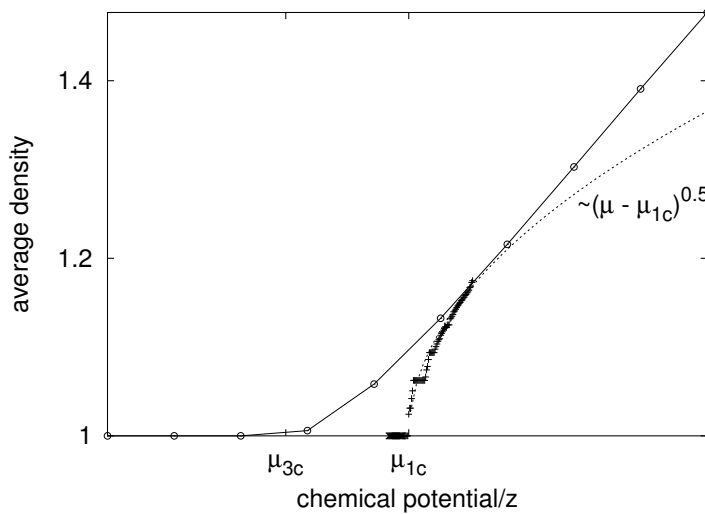


Figure 3.6 Evolution of the density in the neighborhood of the generic phase transition between the Mott and superfluid phase for one (“+” marks) and three (empty circles) dimensions. The dashed line is a fit according to eq.(3.7). In these calculations the source terms are set to zero and lattices of size $L = 1024$ sites were studied. Inclusion of the source terms in one dimension would lead to a similar plot as in the 3D case.

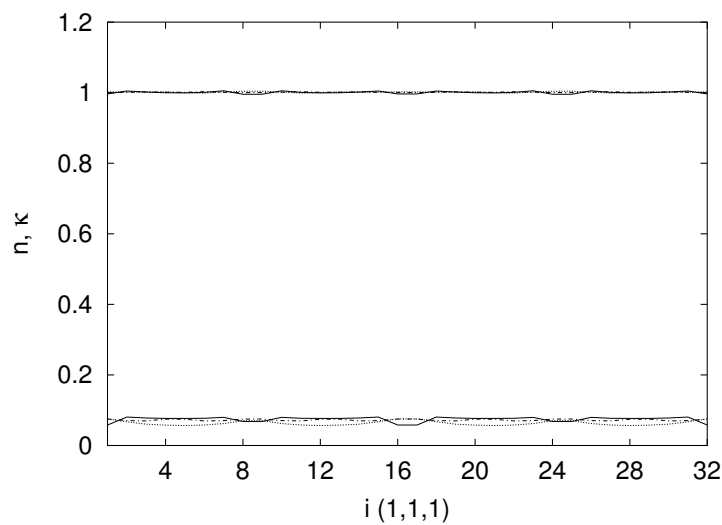


Figure 3.7 Local density (upper curves) and local compressibility (lower curves) for parameters $U/z = 5.0$ and $\mu/z = 2.0$ in one (full line), two (dotted line) and three (dashed line) dimensions. Mean-field theory predicts a superfluid phase, while the true phase in one, two and three dimensions is a Mott phase.

3.3 Results

Now that we have critically examined the approximations made with the mean-field+NRG method, we apply it to parameter regions relevant for the experiment.

3.3.1 Results in one dimension

We have, in complete analogy with Ref. [74], confined a Bose gas in a lattice of 128 sites in a trapping potential of the form

$$\epsilon_i = v_c(i - L/2)^2, \quad (3.7)$$

with $v_c = 0.008$. Choosing the parameter this way allows for filling factors of the order of unity in the center of the trap and for densities going smoothly to zero near the edges of the trap, as it should be for a confined system.

In Fig. 3.8 we see how plateaus with local fillings of an integer number of bosons can arise as more and more particles enter the system. The global compressibility is never zero, while it would be zero in the unconfined model in the thermodynamic limit. We cannot speak therefore of a true quantum phase transition, the confining potential effectively cuts off all long-range correlations. However, in local regions the local compressibility can become very low and the local density can get stuck at integer values, reflecting a local Mott region. This can be seen in Fig. 3.9. All these results are completely in line with the world line quantum Monte Carlo results of Ref. [74]. Also, for a canonical calculation with an incommensurate filling, a Mott phase with integer density can still be found, because the confining potential changes the local chemical potential.

Looking along the sites can be interpreted as different μ -slices of the phase diagram in the (U, μ) plane for the unconfined model [42]. This allows us to calculate the site at which a Mott domain is entered or left. It is clear that the Berezinskii-Kosterlitz-Thouless transition [50, 51] has no analog in the confined case. We refer to Ref. [74] for a state diagram. The authors of Ref. [74] also claim that $\kappa_i \sim (n_i - 1)$ as the Mott lobe is approached, independent of the on-site repulsion U or the chemical potential μ . In our calculations the same behavior was seen for parameters that

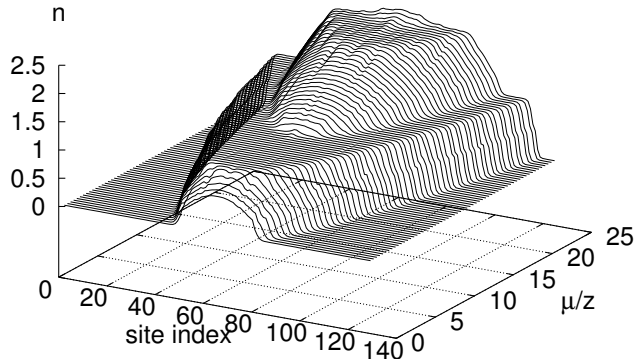


Figure 3.8 Profile of the local density n along the sites and as a function of the chemical potential μ . The on-site repulsion is $U/2 = 7.1$. Above a certain value of μ we see the emergence of a plateau ($n = 1$), and when the total number of particles is even more increased, we see the re-emergence of a compressible region. This happens first around the center and continues to exist till a plateau with $n = 2$ is reached. These results confirm the result of Ref. [74].

are of the same order of magnitude, but for small and large values of U the local compressibilities did not reach to the same values in the Mott region. The absence of universal scaling when an insulating lobe plateau is reached was also found in Ref. [75].

3.3.2 Results in two dimensions

Homogeneous case

In principle it is possible to determine the phase diagram, but a complication that makes a comparison more difficult is that in the literature [73] calculations are usually based on a fixed density while we are working in the grand-canonical ensemble. The physically most interesting case is with a disordered chemical potential [76]. A phase diagram requires a study of phase transitions and very close to a transition point it is important to include more and more states into the truncated

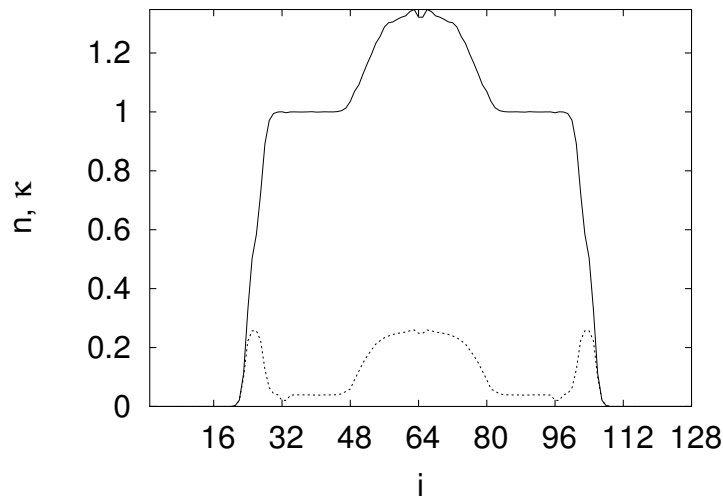


Figure 3.9 Profile of the local density n (solid line) and local compressibility κ (dashed line) along the sites for $U/2 = 7.1, \mu/2 = 6.1, L = 128, v_c = 0.008$, confirming again the result of Ref. [74].

Hilbert space and at the same time going to larger lattices. The method described here can only give a qualitative answer and is not fit to quantitatively yield the exact location of the transition point and does not allow to calculate the critical exponents in an unambiguous way.

The problem encountered here is a ‘memory effect’ when N_s is not high enough. When the source terms are set to zero and a large lattice of $L = 256 \times 256$ is taken, a calculation with a too low N_s predicts a Mott phase while an increased N_s leads to a superfluid phase. So, starting from a Mott phase (zero source terms), results in a Mott phase and starting from a superfluid phase (finite source terms) reveals a superfluid phase. The issue of the phase diagram is very similar to the difficulties encountered with the strong-coupling expansion by Freericks *et al.* [77], although their starting point is entirely different. As they point out, their method cannot describe the physics close to the tricritical point, the density fluctuations dominate even close to the tricritical point, and they can notice that the shape of the Mott lobes has changed from one to higher dimensions. Due to the limitations (source terms, block by block extensions with poor dealing of the boundary conditions on

the constituting blocks and basis truncation errors) in our method we see the same qualitative aspects, but we ran into the same quantitative difficulties, with the same order of uncertainty.

Confined case

The trapping potential takes on each site i the value

$$\epsilon_i = v_c r_i^2, \quad (3.8)$$

where r_i measures the distance from the present site i to the center of the trap. The same holds in three dimensions. In Fig. 3.10 we plot the local density for a system of $L = 64 \times 64$ sites, with $U = 23.2$, $\mu = 28.0$, $v_c = 0.05$ and the space is constantly truncated to 32 states, in line with our philosophy of a limited but fast and reliable calculation. In Fig. 3.11 we show the local compressibility for the same system, but only one quarter of the figure is shown. The other parts are symmetric. Note again that there exists a Mott insulating region with integer density. The transition from the superfluid region to this Mott region is not sharp, and the local compressibility in the Mott region is small but remains finite.

Another example can be found in Fig. 3.12 and Fig. 3.13 for a lattice of 128×128 sites, showing Mott behavior and that for a slightly weaker U a new superfluid region would emerge in the center of the trap.

3.3.3 Results in three dimensions

In the experimental setup, the absorption images of the three dimensional distribution are taken along two orthogonal axes, revealing only the integral over the third direction. It was argued that the observed fading of the Bragg peaks had nothing to do with the appearance of Mott behavior, and happened actually when the system was already very deep in the Mott insulating phase [78].

What could then be a clear signal of the transition? It was argued in Ref. [78] that satellite peaks in the momentum distribution are related to the appearance of a Mott region in the center of the trap. Satellite peaks are extra peaks that occur and that are small compared to the central peak. Once the Mott region spanned

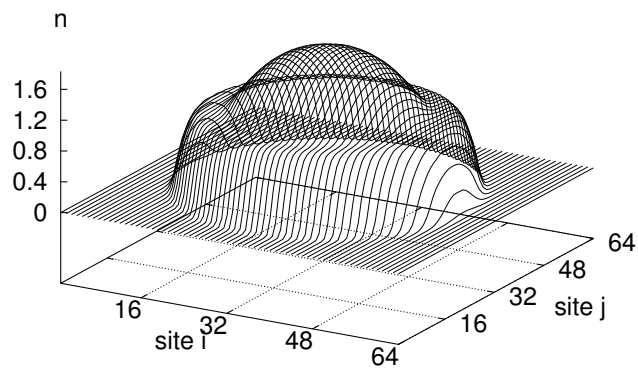


Figure 3.10 Local density for a lattice consisting of $L = 64 \times 64$ sites and with parameters $U = 23.2, \mu = 28.0, v_c = 0.05$. Note again the region with fixed integer density and the smooth transitions.

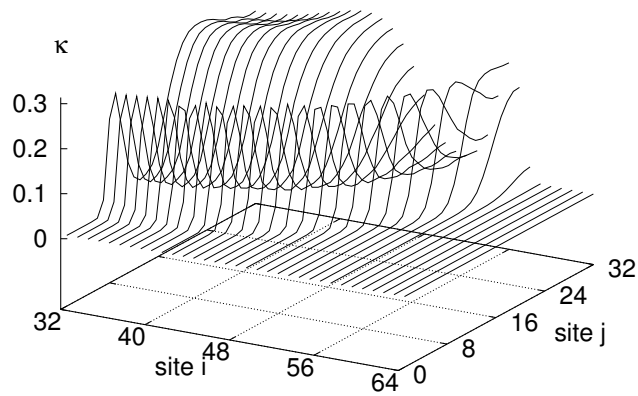


Figure 3.11 Local compressibility as a function of the site indices and with the same parameters as in Fig. 3.10.

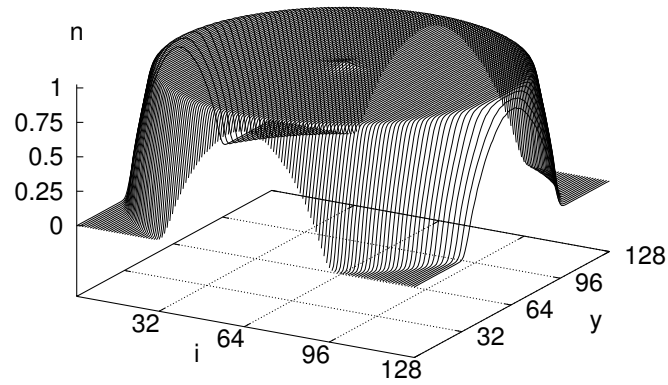


Figure 3.12 Local density as a function of the site indices for a lattice of $L = 128 \times 128$ sites and with parameters $U = 22.0, \mu = 35.6, v_c = 0.008$. The system is very close to developing a new superfluid peak in the center.

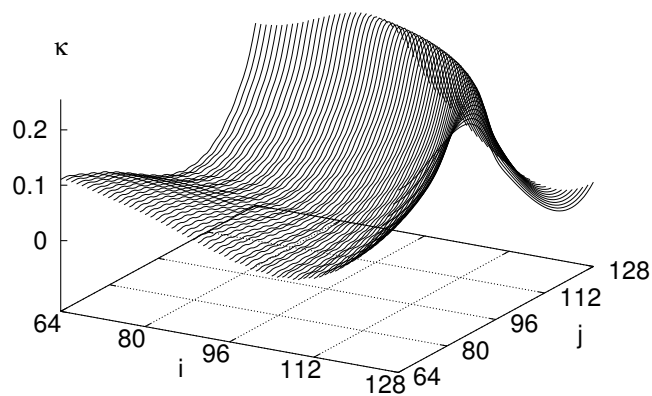


Figure 3.13 Same as in Fig. 3.12 but for the local compressibility. The parts of the plot that are not shown are symmetric.

over almost the entire lattice, the peaks disappeared into the typical broad, low-peaked Mott distribution. However, their Worm Monte-Carlo calculation was only on a lattice of $L = 16 \times 16 \times 16$ and it can be expected that for a larger lattice, the central superfluid peak might be so dominant that the satellite peaks can hardly be resolved. We present a calculation on a lattice of $L = 32 \times 32 \times 32$. We show the momentum distribution in Fig. 3.14 along the $(1, 0, 0)$ axis, for a system with an emerging Mott region of $n = 1$ in the center of the trap. As in Ref. [78] we see satellite peaks along the $(1, 0, 0)$ direction, but the central peak dominates. The satellite peaks are only 4.5% in magnitude of the central peak and will be difficult to be resolved in practice. For the experimental setup with its lattice of about $L = 65 \times 65 \times 65$ sites, the situation will even be worse. We note that the satellite peaks depend on the direction of investigation, so no satellite peaks were seen e.g. along the $(1, 1, 1)$ direction in Fig. 3.14. This directional dependence is a consequence of the breaking of rotational symmetry in a finite lattice, and its effects should diminish when larger lattices are considered.

Furthermore, the average density in the experiments was about $n \approx 2.5$ in the center of the trap [6]. There are no satellite peaks when the central density is non-integer, despite a broad Mott $n = 1$ region for an on-site repulsion U that is strong enough. This Mott region is reflected in the tail of the momentum distribution [78]. For a system with local densities varying between $n = 2$ and $n = 3.2$ (all non-integer densities), we nevertheless found satellite peaks in Fig. 3.15, and calculations showed the same behavior for densities ranging between $n = 3$ and $n = 4$. These peaks cannot possibly be related to the emergence of a Mott region in the center of the trap. Local densities of $n = 2$ at the border of the trap cannot occur experimentally, but this situation can be thought of as the central region of a larger lattice, from which the outer regions are not trapped any more.

When going to higher values of U and μ , it is in principle possible to have Mott phases at $n = 2$ and $n = 3$. In the mean-field phase diagram of the homogeneous model [43], the different Mott lobes corresponding to densities $n = 1, n = 2$, etc. get closer to each other along the direction of the chemical potential μ (see Fig. 2.4). With the confining potential ϵ_i present, the local densities along the different sites can be interpreted as a scan of the homogeneous model [42]. Hence in a small finite

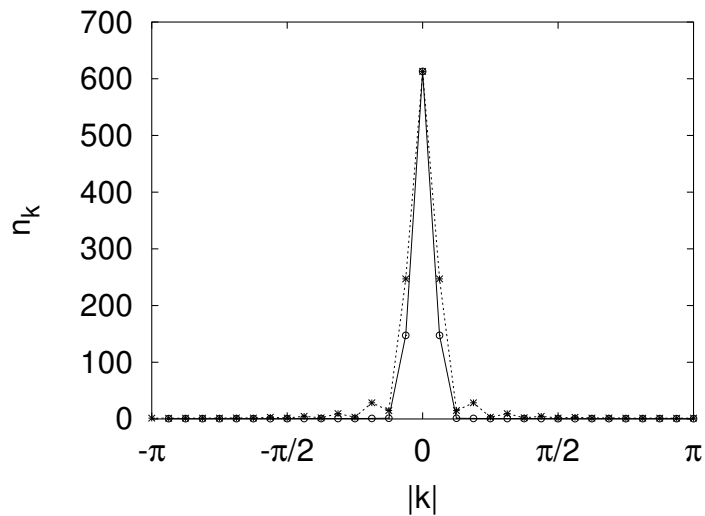


Figure 3.14 Momentum distribution for a system with a Mott plateau ($n = 1$) in the center. The parameters are $U/z = 6.5$, $\mu/z = 2.6$, $v_c = 0.04$ and $L = 32 \times 32 \times 32$. The dashed line represents the distribution along the $(1,0,0)$ direction, while the full line is taken along the $(1,1,1)$ direction. According to Ref. [78] the satellite peaks in the dashed curve point at an emerging Mott region in the center of the trap.

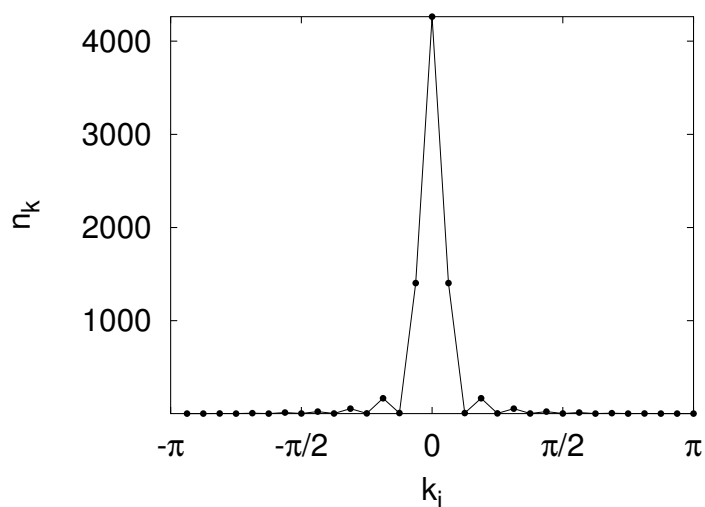


Figure 3.15 Momentum distribution along the $(0, 0, 1)$ axis for a system with particle densities varying between $n = 2$ and $n = 3.2$ ($U/z = 11$, $\mu/z = 30$, $v_c = 0.1$, $L = 32 \times 32 \times 32$). The appearance of satellite peaks cannot be related to the *emergence* of a Mott region in the center of the trap.

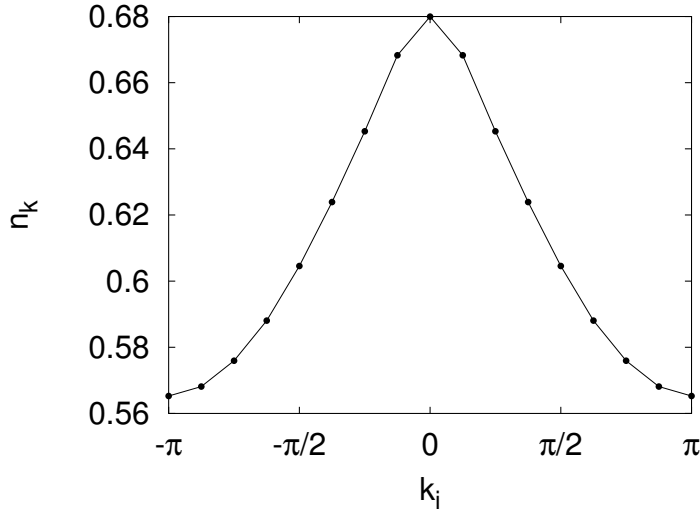


Figure 3.16 Momentum distribution along the $(0, 0, 1)$ axis for a system with particle densities varying between $n = 0$ at the edge of the trap to $n = 3$ at the center ($U/z = 30, \mu/z = 75, v_c = 9.1, L = 16 \times 16 \times 16$), leading to 2280 particles in the system. The distribution is broad and not peaked, signaling virtually overall Mott behavior.

lattice it is not a priori clear if there are non-integer densities between the different broad Mott regions. For a system with parameters $U/z = 30, \mu/z = 75, v_c = 9.1$ and $L = 16 \times 16 \times 16$, we found very few non-integer densities. The density profile consisted of four plateaus with $n = 0, 1, 2, 3$ respectively. We have almost a superposition of four Mott phases leading to the momentum distribution in Fig. 3.16, which is very low peaked and broad. When the local particle density in the center of the trap is gradually increased from $n < 3$ till the Mott region with $n = 3$, and while there already exist broad Mott regions with $n = 1$ and $n = 2$, we did not witness any satellite peaks, because the Mott behavior of the $n = 1$ and $n = 2$ plateaus already dominated the momentum distribution.

We are led to the observation that it will be difficult to indicate the transition experimentally using the satellite peaks, and that only examination of the intensity and the width of the central peak along one direction might be used to directly reveal the gradual cross-over to Mott behavior. Recently, C. Kollath *et al.* came to the same conclusion using the DMRG algorithm for the study of the cross-over in one

dimension [79]. The large-scale Monte Carlo simulations by S. Wessel *et al.* led to the same conclusion [80]. In addition, they showed that the satellite peaks occurred both in the superfluid and in the Mott phase, and are a reflection of the finite extent of the atomic cloud in the trap. This has been confirmed by S. Bergkvist *et al.* in a study of the validity of the local density approximation in one dimension by comparing the local density approximation to quantum Monte Carlo results [75]. The results by S. Wessel *et al.* [80] and S. Bergkvist *et al.* [75] are a confirmation of our observations and the statements we have made, only we could not completely rule out that the satellite peaks we observed are a numerical artefact.

Chapter 4

Exact numerical methods

Although the numerical renormalization group is a variational method and gives quite accurate results for the Bose-Hubbard model, it becomes too hard to improve on its accuracy and too restrictive in its use. In this chapter we discuss two numerical methods that are exact. First, we briefly discuss Lanczos diagonalization, which served as a benchmark tool for all our numerical methods. Second, we introduce Monte Carlo methods and discuss its convergence and efficiency properties. This will be illustrated for a classical model (Potts model). Quantum Monte Carlo methods are discussed in Chapter 5.

4.1 Lanczos diagonalization

In case one is interested in just a few of the lowest eigenvalues and eigenstates of a Hamiltonian, Lanczos diagonalization provides a fast and accurate solution [81]. We assume the Hamiltonian to be represented by a real and symmetric matrix A , which typically is large and sparse. The starting point is an arbitrarily normalized vector $|q_1\rangle$. The key idea is to iteratively generate a basis for the Krylov subspace [81],

$$\mathcal{K}(A, |q_1\rangle, n) = [|q_1\rangle, A|q_1\rangle, A^2|q_1\rangle, \dots, A^{n-1}|q_1\rangle]. \quad (4.1)$$

Direct iterative multiplication with A is called the power method, but is numerically unstable. The Lanczos iteration on the contrary, implicitly constructs this basis by tridiagonalizing the matrix A . The extremal eigenvalues of the tridiagonal matrix are progressively better estimates of A 's extremal eigenvalues. The elements

of the tridiagonal matrix $T = Q^T A Q$,

$$T = \begin{bmatrix} \alpha_1 & \beta_1 & & \cdots & 0 \\ \beta_1 & \alpha_2 & \ddots & & \vdots \\ & \ddots & \ddots & \ddots & \\ \vdots & & \ddots & \ddots & \beta_{n-1} \\ 0 & \cdots & & \beta_{n-1} & \alpha_n \end{bmatrix}, \quad (4.2)$$

are computed directly by equating columns in $AQ = QT$. We find

$$A|q_j\rangle = \beta_{j-1}|q_{j-1}\rangle + \alpha_j|q_j\rangle + \beta_j|q_{j+1}\rangle, \quad (4.3)$$

and $\beta_0|q_0\rangle \equiv |0\rangle$ for $j = 1, \dots, n-1$. The orthonormality of the q_i implies $\alpha_j = \langle q_j|A|q_j\rangle$. If $|r_j\rangle = (A - \alpha_j I)|q_j\rangle - \beta_{j-1}|q_{j-1}\rangle$ is nonzero (where I denotes the unity matrix), then $|q_{j+1}\rangle = |r_j\rangle/\beta_j$ where β_j is the norm of $|r_j\rangle$. The parameters α_j and β_j can thus be obtained recurrently (Lanczos iteration). The power of the Lanczos method is that the extremal eigenvalues converge to their true values after just a couple of iterations (basis truncation), as explained by the Kaniel-Paige convergence theory [81]. This is especially true for the groundstate, but for the excited states one has to be careful. Approximate eigenvalues can remain stuck for some time, and in general spurious eigenvalues appear. Orthogonality between the Krylov basis vectors may be lost as a consequence of limited storage accuracy [81].

There are several computer packages available that implement a partial re-orthogonalization at each step (at a high computational cost). Another approach is the Willoughby-Cullum scheme that tries to detect the spurious eigenvalues using heuristic techniques [81]. This has for instance been implemented in the IETL solver of the ALPS project [82], which offers C++ libraries for the development of code for strongly correlated quantum mechanical systems.

Lanczos methods have been extended to study dynamics and to study systems at finite temperature. They can be applied to any model and allow to calculate virtually any observable of interest. The main limitation of exact diagonalization is that it is restricted to small systems because the method scales exponentially with system size. State of the art computations involve up to a 20 sites square lattice at

Table 4.1 Lanczos Results for the $U = 4$ Bose-Hubbard model with 8 bosons on a lattice of 8 sites at a temperature $T = 0$. Ground state expectation values are shown for (i) the density $\langle n_i \rangle$, (ii) the compressibility $\langle \kappa_i \rangle = \langle n_i^2 \rangle - \langle n_i \rangle^2$, (iii) the Green function $b_1^\dagger b_i$, and (iv) the boson density-density correlation function $\langle n_1 n_i \rangle$.

site(i)	$\langle n_i \rangle$	$\langle \kappa_i \rangle$	$\langle b_1^\dagger b_i \rangle$	$\langle n_1 n_i \rangle$
1	1.00000000	0.34904109	1.00000000	1.34904109
2	1.00000000	0.34904109	0.81527800	0.40094492
3	1.00000000	0.34904109	0.71055894	0.39453292
4	1.00000000	0.34904109	0.66131466	0.37570709
5	1.00000000	0.34904109	0.64674508	0.36904939
6	1.00000000	0.34904109	0.66131466	0.37570709
7	1.00000000	0.34904109	0.71055894	0.39453292
8	1.00000000	0.34904109	0.81527800	0.40094492

half filling for the (Fermi-)Hubbard Hamiltonian.

As a numerical example, we provide numbers in units of t for the $U = 4$ Bose-Hubbard model, consisting of $N = 8$ bosons on a lattice of $L = 8$ sites. The dimension of the Hilbert space is $\frac{(N+L-1)!}{N!(L-1)!} = \frac{15!}{8!7!} = 6435$, not taking any symmetries into account. The groundstate energy was found to be $E = -7.45979062605314$ with an error of 2.2449×10^{-14} . In Table 4.1 observables like the density, compressibility, Green function and boson density-density correlation function are shown.

4.2 Monte Carlo Strategies

In this section we explain the basics of Monte Carlo and show how Monte Carlo can be used in physics by using Markov Chains. The efficiency of Markov Chain Monte Carlo is discussed and illustrated with an example from classical physics. The book on Monte Carlo by J. S. Liu [83], the book by M. E. J. Newman and G.T. Barkema [84], and the PhD-thesis by S. Rombouts [85] were guiding texts for this section. Algorithms for quantum problems are explained in full detail in Chapter 5.

4.2.1 Monte Carlo Techniques

A common problem in many scientific problems is the evaluation of the integral

$$I = \int_D g(x) dx, \quad (4.4)$$

where D is a region in a high-dimensional space and $g(x)$ is the target function of interest. If we can draw independent and identically distributed random samples $x^{(1)}, \dots, x^{(n)}$ uniformly from D then we can approximate I by the estimator

$$\hat{I}_m = \frac{1}{m} \left(g(x^{(1)}) + \dots + g(x^{(m)}) \right). \quad (4.5)$$

If each of the independent random variables has a common mean μ and finite variance σ^2 , then \hat{I}_m converges almost surely to I by the law of the large numbers,

$$\text{Prob} \left[\lim_{m \rightarrow \infty} |\hat{I}_m - I| = 0 \right] = 1. \quad (4.6)$$

The convergence rate can be assessed by the central limit theorem,

$$\lim_{m \rightarrow \infty} \text{Cdf} \sqrt{m}(\hat{I}_m - I) = \text{Cdf} N(0, \sigma^2), \quad (4.7)$$

where Cdf denotes the cumulative distribution function and $N(0, \sigma^2)$ the normally distributed probability function with mean 0 and variance σ^2 . The error term of the Monte Carlo approximation is hence $\mathcal{O}(m^{-1/2})$, regardless of the dimensionality of D . However, the variance σ^2 might be very large when the region D is large, and it is not always possible to draw random samples in an arbitrary region D . This is usually the case in statistical mechanics where we want to compute thermodynamical averages of quantities Q

$$\langle Q \rangle = \frac{1}{Z} \text{Tr} \left[Q e^{-\beta H} \right] = \frac{\text{Tr} \left[Q e^{-\beta H} \right]}{\text{Tr} \left[e^{-\beta H} \right]}, \quad (4.8)$$

with Z the partition function and H the Hamiltonian. A possible choice is to draw samples according to the target distribution $\pi(x) = Z^{-1} \exp(-\beta E(x))$, with $E(x)$ the energy of the system in configuration (state) x . The unnormalized weight of this configuration is $W(x) (= \exp(-\beta E(x)))$, while the normalization factor is the partition function. From now on, the notations $W(\cdot)$ and $\pi(\cdot)$ are used in this sense. The estimate for the expectation value for the observable Q is then $\langle Q \rangle = \frac{1}{m} \sum_{i=1}^m Q(x^{(i)})$ where the hat-superscript for the estimator is suppressed for notational convenience. Unfortunately, directly generating samples from $\pi(x)$ is in general not possible, and in practice the only reasonable alternative is to resort on Markov chains producing statistically dependent samples.

4.2.2 Markov Chains

Consider a sequence of random variables (configurations) $x^{(0)}, x^{(1)}, \dots$ defined on a finite state space \mathcal{S} , which we will assume to be a finite, countable set. The sequence is called a Markov chain if the current state depends on its past only through the previous state, or more formally

$$\text{Prob} \left[x^{(t+1)} = y | x^{(t)} = x, \dots, x^{(0)} = z \right] = \text{Prob} \left[x^{(t+1)} = y | x^{(t)} = x \right]. \quad (4.9)$$

If the form of the transition probability $\text{Prob} \left[x^{(t+1)} = y | x^{(t)} = x \right]$ is time independent then it is expressed as a transition function $T(x, y)$ with the immediate property $\sum_y T(x, y) = 1, \forall x$. Our task is to define a useful transition function $T(x, y)$ while the target distribution is known.

A Markov chain is said to be irreducible if under the transition rule any state x can be reached from any initial state $x^{(0)}$ in a finite number of Markov steps. A Markov chain is aperiodic if for any state $x \in \mathcal{S}$ the greatest common divider of $\{n : T^{(n)}(x, x) > 0\}$ is 1. For instance, the Markov chain on the state space $\{\pm 1, \pm 1, \dots, \pm 1\}$ with the transition rule that only one of the signs can be inverted at a time, has periodicity 2 and is not aperiodic. If a finite-state Markov chain is irreducible and aperiodic, then it converges to the stationary distribution exponentially. From $\sum_y T(x, y) = 1, \forall x$ we see that the transition matrix T has an eigenvalue $\lambda_1 = 1$. Irreducibility is equivalent to requiring that all other eigenvalues λ_j of T satisfy $|\lambda_j| < 1$.

A transition rule $T(x, y)$ leaves the unnormalized target distribution $W(x)$ invariant if $\sum_x W(x)T(x, y) \sim W(y)$. This will certainly be the case if detailed balance is satisfied,

$$W(x)T(x, y) = W(y)T(y, x). \quad (4.10)$$

The formulation of the problem is thus: we can compute the (unnormalized) weight $W(x)$ for all configurations (states) x , and we have to define a transition matrix $T(x, y)$ such that $W(x)T(x, y) = W(y)T(y, x)$ and $\sum_y T(x, y) = 1$. A general solution is provided by the Metropolis-Hastings algorithm [19, 22]. Instead of the

transition matrix $T(x, y)$ one works with a proposal function $P(x, y)$, which is simpler to implement. A proposal state y is drawn from this proposal function and this proposal state is accepted as the new state with probability

$$q = \min \left[1, \frac{W(y)P(y, x)}{W(x)P(x, y)} \right]. \quad (4.11)$$

This clearly satisfies all requirements on the transition matrix since we can write the Metropolis transition matrix in the form

$$\begin{cases} T^{\text{Met}}(x, y) = P(x, y)q = W(y) \min \left[\frac{P(x, y)}{W(y)}, \frac{P(y, x)}{W(x)} \right], & \text{if } x \neq y \\ T^{\text{Met}}(x, x) = 1 - \sum_{y \neq x} T^{\text{Met}}(x, y), & \text{if } x = y \end{cases}. \quad (4.12)$$

Another solution that we discuss is the heat-bath or Gibbs sampler [83],

$$T^{\text{HB}}(x, y) = \frac{W(y)}{\sum_z W(z)}. \quad (4.13)$$

This corresponds to independent sampling when applied to the whole configuration space (which we cannot do in general).

4.2.3 Efficiency

The Markov Chain trivially correlates subsequent measurements. Once we have an aperiodic and irreducible Markov chain at our disposal that converges to its unique stationary distribution $\pi(x)$, we are interested in the computation of the estimator $\langle Q \rangle$ for a certain observable $Q(\cdot)$ of interest. Suppose we have drawn samples $x^{(1)}, \dots, x^{(m)}$ from the target (stationary) distribution $\pi(x)$. Then,

$$\begin{aligned} \text{mvar} \left[\frac{Q(x^{(1)}) + \dots + Q(x^{(m)})}{m} \right] &= \sigma^2 \left[1 + 2 \sum_{j=1}^{m-1} \left(1 - \frac{j}{m} \right) \rho_j \right] \\ &\approx \sigma^2 \left[1 + 2 \sum_{j=1}^{\infty} \rho_j \right], \end{aligned} \quad (4.14)$$

where $\sigma^2 = \text{var}[Q(x)]$ and ρ_j the normalized autocorrelation function,

$$\rho_j = \frac{\langle Q(x^{(j+1)})Q(x^{(1)}) \rangle - \langle Q(x^{(1)}) \rangle^2}{\langle Q^2(x^{(1)}) \rangle - \langle Q(x^{(1)}) \rangle^2}, \quad (4.15)$$

The integrated autocorrelation time of $Q(x)$ is defined as

$$\tau_{int}(Q) = \frac{1}{2} + \sum_{j=1}^{\infty} \rho_j. \quad (4.16)$$

Then $m\text{var}(\langle Q \rangle) = 2\tau_{int}(Q)\sigma^2$, meaning that the effective sampling size is reduced to $m/[2\tau_{int}(Q)]$. The decorrelation factor is defined as $2\tau_{int}(Q)$. Often the autocorrelation function decays exponentially, which gives rise to the expression

$$\tau_{exp}(Q) = \limsup_{j \rightarrow \infty} \frac{j}{-\ln |\rho_j|}, \quad (4.17)$$

where τ_{exp} is the exponential autocorrelation time. The relaxation time of the system is the supremum over all exponential autocorrelation times of all observables. If the observable Q corresponds to an eigenfunction with eigenvalue λ of the transition matrix, then we have $\rho_j = \lambda^j$. Hence,

$$\begin{aligned} \tau_{int}(Q) &= \frac{1 + \lambda}{2(1 - \lambda)} \\ \tau_{exp}(Q) &= -\frac{1}{\ln |\lambda|}, \end{aligned} \quad (4.18)$$

and the relaxation time is

$$\tau_{exp} = -\frac{1}{\ln |\lambda_2|}, \quad (4.19)$$

where λ_2 is the second largest eigenvalue in magnitude of the transition matrix. In general, every observable (and certainly an order parameter) couples more or less strongly with the mode corresponding to the second largest eigenvalue. The convergence speed (thermalization) of the sampler is dominated by the exponential autocorrelation time, while the the statistical efficiency of the algorithm is determined by the integrated autocorrelation time.

4.2.4 Peskun ordering

The asymptotic efficiency of the sampler with transition kernel $T(x, y)$ reads (see eq.(4.15))

$$v(Q, T) = \lim_{n \rightarrow \infty} \frac{1}{n} \text{var} \left[\sum_{t=1}^n Q(x^{(t)}) \right]. \quad (4.20)$$

Peskun showed that if two transition kernels T_1 and T_2 satisfy detailed balance with the same invariant distribution and if all off-diagonal elements of T_1 are larger than or equal to those of T_2 then the chain T_1 will be asymptotically more efficient [86]. Equivalently, this means that the second largest eigenvalue of T_1 is smaller than the second largest eigenvalue of T_2 . Peskun's theorem implies an ordering of the weights. Let $\pi_1 \leq \pi_2 \leq \dots \leq \pi_n$ be the normalized weights in ascending order, $\pi_i = \frac{W_i}{\sum_j W_j}$. Peskun's theorem tells us that we can always improve a transition matrix T by 'Metropolizing' it, $T'_{ij} = \frac{T_{ij}}{\sum_{j \neq i} T_{ij}}, \forall j \neq i$. Applying this idea to heat-bath updates of eq.(4.13), the following Metropolized Gibbs sampler(MG) is obtained,

$$T_{ij}^{MG} = \begin{bmatrix} 0 & \frac{\pi_2}{1-\pi_1} & \frac{\pi_3}{1-\pi_1} & \dots & \frac{\pi_n}{1-\pi_1} \\ \frac{\pi_1}{1-\pi_1} & 1 - \dots & \frac{\pi_3}{1-\pi_2} & \dots & \frac{\pi_n}{1-\pi_2} \\ \frac{\pi_1}{1-\pi_1} & \frac{\pi_2}{1-\pi_2} & 1 - \dots & \dots & \frac{\pi_n}{1-\pi_3} \\ \vdots & \vdots & \vdots & \ddots & \vdots \\ \frac{\pi_1}{1-\pi_1} & \frac{\pi_2}{1-\pi_2} & \frac{\pi_3}{1-\pi_3} & \dots & 1 - \dots \end{bmatrix}, \quad (4.21)$$

or $T_{ij}^{MG} = \min(\frac{\pi_j}{1-\pi_i}, \frac{\pi_j}{1-\pi_j})$. Liu has applied this idea to the independence Gibbs sampler, and obtained a complete eigenanalysis for the resulting stochastic matrix [87, 88].

It is possible to repeat this Metropolizing procedure until all but one of the diagonal elements are zero. Optimal transition matrices must have $T_{ii} = 0, i \neq n$. Indeed, Frigessi *et al.* [89] have shown that the unique optimal transition matrix is of the form,

$$T_{ij}^{Opt} = \begin{bmatrix} 0 & \frac{\pi_2}{\pi_1} y_1 & \frac{\pi_3}{\pi_1} y_1 & \dots & \frac{\pi_n}{\pi_1} y_1 \\ y_1 & 0 & \frac{\pi_3}{\pi_2} y_2 & \dots & \frac{\pi_n}{\pi_2} y_2 \\ y_1 & y_2 & 0 & \dots & \frac{\pi_n}{\pi_3} y_3 \\ \vdots & \vdots & \vdots & \ddots & \vdots \\ y_1 & y_2 & y_3 & \dots & 1 - y_1 - y_2 - \dots \end{bmatrix}, \quad (4.22)$$

with $y_1 = \frac{\pi_1}{1-\pi_1}, y_2 = (1 - y_1) \frac{\pi_2}{1-\pi_1-\pi_2}, \dots$. The eigenvalues are given by $1, \lambda_2 = -y_1$ (the same as in eq(4.21)), $\lambda_3 = -y_2, \dots$. They are all negative and appear in an ordered way. This λ_2 has the lowest value that possibly can be obtained with respect to the probability distribution π , and with λ_2 determined, λ_3 is then the smallest possible third largest eigenvalue, etc. Note that a rescaling is at work here, the entries for the second row $T_{2j}, j = 2, \dots, n$ are analogous to the first row apart

from the rescaling $1 \rightarrow (1 - y_1)$. The eigenvectors can also be obtained in closed form, they are

$$\begin{aligned} e_1 &= [1, 1, \dots, 1]^T \\ e_{k+1} &= \left[\underbrace{0, \dots, 0}_{(k-1)\text{terms}}, 1 - \frac{\pi(k)}{\pi(k) + \dots + \pi(n)}, \right. \\ &\quad \left. - \frac{\pi(k)}{\pi(k) + \dots + \pi(n)}, \dots, - \frac{\pi(k)}{\pi(k) + \dots + \pi(n)} \right]^T \end{aligned} \quad (4.23)$$

Although optimal sampling is only achieved when eq.(4.22) is applied to the entire Hilbert space, in many situations of practical interest stochastic subprocesses need to be sampled. For these, efficient sampling can be achieved if all but one of the diagonal elements are zero. When eq.(4.22) is applied to a stochastic subprocess, we call it the locally optimal algorithm, where optimal is related to the local aspects only.

A different approach towards improving on efficiency has been taken in the field of broad histogram and related methods, where one has tried to optimize the ensemble (instead of the transition matrix) [90]. It is not fully understood yet how both approaches can be compatible [91].

As a first application of locally optimal Monte Carlo, we consider the $q = 4$ Potts model [84] in two dimensions, with Hamiltonian

$$H = -J \sum_{\langle i,j \rangle} \delta_{\sigma_i, \sigma_j}. \quad (4.24)$$

The sum extends over nearest neighbor sites only, and the energy is lowered when the spins σ take the same orientation on neighboring sites. The spins can take $q = 4$ different values. The energy scale is set using $J = 1$. The system exhibits a second order phase transition between a magnetic and disordered state at the critical value $\beta = \ln(1 + 2) \approx 1.1$ in the thermodynamic limit [92]. We are interested in the dynamics of the Monte Carlo process. Therefore we consider a small lattice with single-spin updates only, and we do not want to use cluster updates [25, 93] here. So we randomly select a spin, after which we have to make a choice between the four possible orientations that this spin can take. Although the random selection of

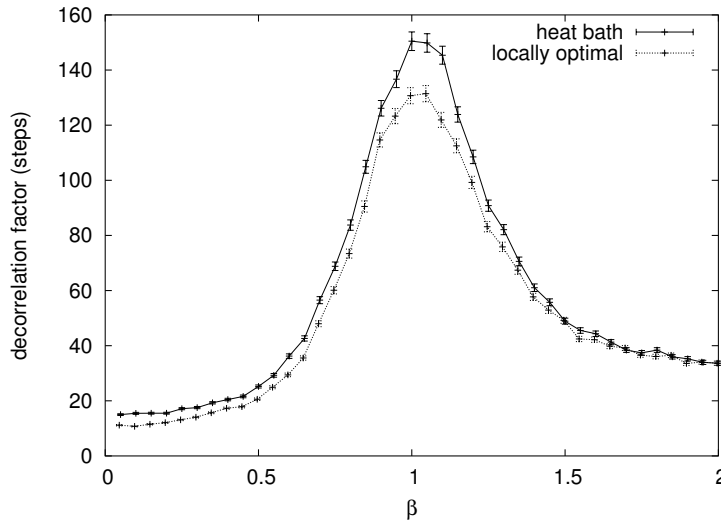


Figure 4.1 The decorrelation factor for the energy as a function of temperature β at constant interaction strength for the $q = 4$ Potts model on a $L = 4 \times 4$ matrix is shown for heat-bath updates and for the locally optimal ones. Simulations consisted of 4000 chains of one million steps each.

a site and the single spin update both seriously violate the structure of the optimal stochastic matrix of eq.(4.22), the Peskun theorem still holds, meaning that the matrix of eq.(4.22) (applied to the stochastic subprocess) still leads to a more effective sampling than heat-bath updating, $T_{ij} = \frac{W_j}{\sum_k W_k} = \pi_j, \forall i, j$. This of course cannot cure the fact that the updating of a single spin still leads to the divergence of the autocorrelation time when the temperature reaches its critical value β_c .

The decorrelation factor [85] $\sigma_Q^2/\sigma_{0,Q}^2$ has been defined above as the ratio between the error bars obtained from a Monte-Carlo simulation with correlations between successive samples (bins) and the error bars one would obtain from the same number of independent but identically distributed samples. In the limit of a large number of samples, the decorrelation factor becomes equal to twice the integrated autocorrelation time (eq.(4.16)). The decorrelation factor can accurately be estimated by running a large number of independent Markov chains. In Fig. 4.1, we see that the decorrelation factor is much smaller for the locally optimal algorithm than for the heat-bath algorithm.

A small lattice of $L = 4 \times 4$ has been chosen since the decorrelation factor scales

with system size for single-site updates such that the difference between the two algorithms will be larger in absolute terms when using a small lattice. We clearly see a significant difference between the locally optimal and the heat-bath transition probabilities. The Metropolized Gibbs sampler T^{MG} (eq.(4.21)) has the same λ_2 as the optimal one (eq.(4.22)), and the integrated autocorrelation times differ only slightly for the 4×4 Potts model.

Chapter 5

Quantum Monte Carlo algorithms

In the present chapter we discuss quantum Monte Carlo algorithms that are based on a worldline graphical interpretation. The directed loop algorithm in the stochastic series expansion representation and the worm algorithm are introduced. They have in common that they provide a local sampling of the Green function. This chapter uses the ideas about efficient Markov Chain Monte Carlo sampling that have been outlined in Chapter 4.

We are interested in the computation of thermodynamic observables $\langle Q \rangle$,

$$\langle Q \rangle = \frac{\text{Tr} [Q \exp(-\beta H)]}{Z}, \quad (5.1)$$

which requires knowledge of the partition function Z ,

$$Z = \text{Tr} [\exp(-\beta H)]. \quad (5.2)$$

The partition function is too complex to calculate, and we shall try to perform the summation statistically using Monte Carlo methods. In contrast to the classical case, we do not know the exact eigenvalues (energies) of the system. We need a representation for the partition function, and with each configuration a weight is assigned. The definition of the weight function should be done carefully as it has to be positive definite. Unfortunately this condition cannot always be met and gives rise to the infamous 'sign problem'. When the sign problem occurs there is an exponential slowdown of the algorithm, but on the other hand the sign problem depends on the representation, and the sign problem might be overcome in those

cases where a fortuitous representation exists. In order to facilitate our search for a good representation of the partition function, we will write the most general two-body Hamiltonian H as

$$H = H_0 - V, \quad (5.3)$$

where H_0 denotes a diagonal term and V an interaction. A useful decomposition for the partition function is then

$$Z = \sum_{n=0}^{\infty} \int_0^{\beta} dt_n \int_0^{t_n} dt_{n-1} \cdots \int_0^{t_2} dt_1 e^{-t_1 H_0} V e^{-(t_2-t_1)H_0} \cdots \cdots e^{-(t_n-t_{n-1})H_0} V e^{-(\beta-t_n)H_0}. \quad (5.4)$$

We arrive now at the stochastic series representation expansion (SSE) by setting

$$H_0 = 0, V = -H, \quad (5.5)$$

allowing us to integrate out all times in eq.(5.4). This yields the high temperature series expansion for the partition function,

$$Z = \text{Tr} \sum_{n=0}^{\infty} \frac{(-\beta H)^n}{n!}. \quad (5.6)$$

This little detour with imaginary times will help us explaining the analogy between the directed loop algorithm and the worm algorithm (see section 5.5). A local algorithm in the SSE representation has first been introduced by Sandvik and Kurkijärvi [28, 29] as a generalization of Handscomb's method for a spin-1/2 ferromagnetic Heisenberg model [30]. More recently, Sandvik has proposed a more refined version of his algorithm using operator loop updates [32, 33, 94]. The derivation of this algorithm will now be presented for the homogeneous Bose-Hubbard Hamiltonian in the grand-canonical ensemble on a d - dimensional square lattice,

$$H = -t \sum_{\langle i,j \rangle} b_i^\dagger b_j + \frac{1}{2} U \sum_i n_i(n_i - 1) - \sum_i \mu n_i. \quad (5.7)$$

First we will discuss the representation in detail.

5.1 Stochastic Series Expansion: representation

It is convenient to work with bond operator forms [32, 33, 95]

$$H = - \sum_{b=1}^{N_b} H_b = - \sum_{b=1}^{N_b} [H_{1,b} + H_{2,b} + H_{3,b}], \quad (5.8)$$

with N_b the total number of bonds between the L sites of the lattice. For each bond b we have introduced the bond operators that connect the interacting sites $i(b)$ and $j(b)$. The expressions for the bond operators are made symmetric in the site indices,

$$H_{1,b} = C_{\text{add}} - \frac{U}{2z} n_{i(b)}(n_{i(b)} - 1) - \frac{U}{2z} n_{j(b)}(n_{j(b)} - 1) + \frac{\mu}{z} (n_{i(b)} + n_{j(b)}), \quad (5.9)$$

$$H_{2,b} = t b_{i(b)}^\dagger b_{j(b)} \quad (5.10)$$

$$H_{3,b} = t b_{j(b)}^\dagger b_{i(b)}. \quad (5.11)$$

Here, $z = 2d$ denotes the coordination number. The constant C_{add} is a constant energy shift and ensures the (semi-)positive definiteness of all bond operators. $H_{2,b}$ and $H_{3,b}$ are called off-diagonal interactions (with respect to the sites), while $H_{1,b}$ is called a diagonal interaction. All operators are symmetric in the site indices $i(b)$ and $j(b)$ corresponding to the bond b . This name giving is related to the fact that we choose the local product basis $B = \text{Span}\{|i\rangle\} = \text{Span}\{|i_1, i_2, \dots, i_L\rangle\}$ as the basis of the Hilbert space. The bond operators $H_{i,b}$ have the crucial property that when acting on a basis state the resulting state is again a single element of the basis set, $H_{i,b}|i\rangle = |i'\rangle$. With this chosen basis, we can now replace the Trace operator in eq.(5.6),

$$Z = \sum_{|i\rangle} \sum_{n=0}^{\infty} \frac{(-\beta)^n}{n!} \langle i | H^n | i \rangle. \quad (5.12)$$

The sum over n can be truncated at $n = M$ with M of the order βN_b . M can be increased during the early stages of the simulation and will not be the source of any systematic errors. Introducing the unit operator $H_{0,0} = 1$ we can express the partition function as

$$Z = \sum_{|i\rangle} \sum_{S_M} (-1)^{n'(S_M)} \frac{\beta^{n(S_M)} (M - n(S_M))!}{M!} \langle i | \prod_{l=1}^M H_{a_l, b_l} | i \rangle, \quad (5.13)$$

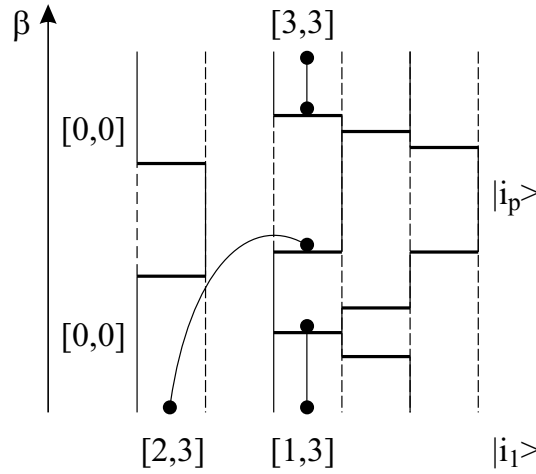


Figure 5.1 Graphical interpretation of the SSE representation (see text).

which defines the operator string S_M of length M ,

$$S_M = \{[a_1, b_1], [a_2, b_2], \dots, [a_M, b_M]\}, \quad (5.14)$$

with $a_i \in \{1, 2, 3\}$ and $b_i \in \{1, 2, \dots, N_b\}$ or $[a_i, b_i] = 0, 0$. The number of non-[0, 0] elements in S_M is denoted by $n(S_M)$, and $n'(S_M)$ denotes the number of off-diagonal operators in S_M . In order to avoid the sign problem, the latter quantity needs to be even, which is true for bipartite lattices with nearest neighbor hopping. Hence, the algorithm is restricted to models without frustration. Note that only the sequence in the operator string is of importance, the imaginary time intervals between the operators have been integrated out of the problem. Let us also introduce a notation for states obtained by acting with the first p elements of the operator string S_M on a state $|i\rangle$,

$$|i(p)\rangle = |i_1(p), i_2(p), \dots, i_L(p)\rangle = H_{a_p, b_p} \circ \dots \circ H_{a_2, b_2} \circ H_{a_1, b_1} |i\rangle, \quad (5.15)$$

with $|i(M)\rangle = |i(0)\rangle$ due to the trace. We use an analogous notation for states $|i_b(p)\rangle$ corresponding to bond b only.

There is a graphical representation associated with the SSE representation of the configuration. In Fig. 5.1 imaginary time runs from 0 to β from bottom to top. The sites of the current state $|i\rangle$ can be (singly/doubly/...) occupied which is indicated by a (single/double/...) full line. When the site is not occupied, a dashed

line is drawn. Due to the trace and the $U(1)$ symmetry, full lines are continuous and close on themselves and are called world lines. Horizontal lines represent a bond operator acting on the current state and are called vertices. The state $|i(p)\rangle$, obtained after the action of the first p elements in the operator string S_M can be obtained by sequentially scanning the operator string and changing the initial state $|i\rangle$ every time an off-diagonal operator is encountered. This means that during the simulation only one state and the operator string (two integers for every element in the string) have to be stored in computer memory. In Fig. 5.1, the bonds have been numbered from left to right, and the elements on bond nr. 3 are $[1, 3]$, $[2, 3]$ and $[3, 3]$ from bottom to top, corresponding to one diagonal interaction and two off-diagonal interactions, respectively. A typical operator string corresponding to Fig. 5.1 looks like

$$[0, 0], [3, 4], [1, 3], [0, 0], [0, 0], \dots, [1, 4], [3, 3], [0, 0], [0, 0]. \quad (5.16)$$

The matrix element in eq.(5.13) implies a chain of (bond) matrix elements,

$$\prod_{p=1}^{n(S_M)} \langle i_{b_p}(p) | H_{b_p} | i_{b_p}(p-1) \rangle. \quad (5.17)$$

All non-trivial (bond) matrix elements for the Bose-Hubbard model are,

$$\begin{aligned} \langle i_{i(b)}, i_{j(b)} | H_b | i_{i(b)}, i_{j(b)} \rangle &= C_{\text{add}} - \frac{U}{2z} n_{i(b)} (n_{i(b)} - 1) \\ &\quad - \frac{U}{2z} n_{j(b)} (n_{j(b)} - 1) + \frac{\mu}{z} (n_{i(b)} + n_{j(b)}), \\ \langle i_{i(b)} + 1, i_{j(b)} - 1 | H_b | i_{i(b)}, i_{j(b)} \rangle &= t \sqrt{(n_{i(b)} + 1) n_{j(b)}}, \\ \langle i_{i(b)} - 1, i_{j(b)} + 1 | H_b | i_{i(b)}, i_{j(b)} \rangle &= t \sqrt{(n_{j(b)} + 1) n_{i(b)}}, \end{aligned} \quad (5.18)$$

where the matrix element is zero otherwise or it is zero when a particle number drops below zero or exceeds the (arbitrarily high) particle number cut-off on a particular site.

5.2 Directed loop algorithm

Now that we have discussed a useful representation of the partition function and the graphical interpretation of any configuration, we are in a position to define the

updates that are performed in every step of the Monte Carlo process. There are two kind of updates involved.

5.2.1 Diagonal update

In the first update step, we scan the operator string S_M sequentially, and the update will try to make changes of the form $[0, 0]_p \leftrightarrow [1, b_p]_p$ at every position $p = 1, \dots, M$. This update changes the expansion order n by ± 1 . As an example, we derive the acceptance factor q for the update $[0, 0]_p \rightarrow [1, b_p]$ using the Metropolis-Hastings recipe [22], $q = \frac{W(y)P(y \rightarrow x)}{W(x)P(x \rightarrow y)}$, where $W(x)$ is the weight of the current configuration x and $P(x \rightarrow y)$ describes the transition to the new configuration y . The factors in the nominator describe the process that is exactly the reverse of the one described above. The update does not change the number of off-diagonal operators, nor do the operators before or after the current position p change. Hence, the relevant factors to the weight $W(x)$ of the current configuration are,

$$W(x) = \beta^{n(S_M)} \frac{(M - n(S_M))!}{M!}. \quad (5.19)$$

We propose that in the update $[0, 0]_p \rightarrow [1, b_p]$ each of the N_b bonds can be chosen with equal probability, $P(x \rightarrow y) = \frac{1}{N_b}$. For the reverse move, there is only one $[0, 0]_p$ state, so $P(y \rightarrow x) = 1$. Leaves us only with the computation of the weight $W(y)$ of the new configuration, where we also have to take the matrix element of the new bond operator into account,

$$W(y) = \beta^{n(S_M)+1} \frac{(M - (n(S_M) + 1))!}{M!} \langle i_b(p) | H_{1,b_p} | i_b(p) \rangle. \quad (5.20)$$

The new configuration is finally accepted with probability

$$P([0, 0]_p \rightarrow [1, b_p]) = \min[1, q] = \min \left[1, \frac{\beta N_b \langle i_b(p) | H_{1,b} | i_b(p) \rangle}{M - n} \right]. \quad (5.21)$$

Analogously, one finds

$$P([1, b_p] \rightarrow [0, 0]_p) = \min \left[1, \frac{M - n + 1}{\beta N_b \langle i_b(p) | H_{1,b} | i_b(p) \rangle} \right]. \quad (5.22)$$

5.2.2 Off-diagonal update

In the second step of the update, we will try to change diagonal interactions in off-diagonal ones, and vice versa. From the operator sequence S_M we construct

the reduced sequence of non- $[0, 0]$ elements, while storing the position of the $[0, 0]$ elements for future reference. As it can be seen in Fig. 5.1 the (bond) matrix elements can be represented by a four-leg vertex, where the legs carry the occupation (quantum numbers) of the current site. The legs connect all vertices. Since the occupations of the legs completely specify the overall configuration, we can construct a linked list of vertices plus the occupations on the four legs starting from the current state $i(0)$ and the reduced sequence. The list should be doubly linked, because we want to travel both upwards and downwards in imaginary time. From every leg of a given vertex we can now travel to the leg of the vertex to which this vertex is connected. The doubly linked list forms a graph, and during the second kind of update the topology of the graph will not change, but the occupations (quantum numbers) of the legs and the operators at the vertices will change.

Off-diagonal update : description

Let us first describe in words what a typical operator loop update looks like. First we select a random leg in space-time, where a discontinuity pair is inserted, that is a segment of infinitesimal length where the occupation is increased or decreased by one. The end points of this segment are called an increasing and a decreasing worm. We then have to choose a direction, upwards or downwards in imaginary time. One of the two worms remains immobile, while the other worm starts to move, and reaches a first vertex, hereby changing the occupation on the entrance leg. At the vertex the worm has to choose one of the legs of this vertex to continue its journey. It is possible that the worm changes its direction in imaginary time. The worm increases or decreases the occupation on the exit leg as well. The chosen leg is connected by the double linked list to another vertex, where the worm travels to. The motion continues until the worm reaches the immobile worm again and bites in its own tail. At this point both discontinuities are annihilated and the update is completed. Note that the worm does not have the ability to insert new interactions (vertices).

Extended configuration space

More formally, the update described above is a local update in the extended configuration space of the Green function,

$$Z_e[U(i, j, \tau)] = \text{Tr} \left[\mathcal{T} \left((b_i(0)b_j^\dagger(\tau) + b_i^\dagger(0)b_j(\tau)) \exp(-\beta H) \right) \right], \quad (5.23)$$

where the worm $U(i, j, \tau)$ has site-indices i and j where the occupation number increases/decreases at imaginary times 0 and τ . The summation over the dependencies i, j and τ is implicit. The notation $b_j^\dagger(\tau, \uparrow)$ for the mobile worm will also be used, indicating the direction in imaginary time. However, this information is already known, since $b_j^\dagger(\tau, \uparrow) = b_j(\tau, \downarrow)$. (i.e. when a worm changes its direction in imaginary time at a vertex, it will also change its action from increasing to decreasing because of the $U(1)$ symmetry). Our original configuration space is naturally embedded in the extended configuration space and we can go back to the original one whenever $i = j$ and $\tau = 0, \beta, 2\beta, \dots$. Although the imaginary time τ appears again (recall that we have integrated out all time dependences in the setup of the algorithm), we do not have to change the SSE representation,

$$\mathcal{T} \left(b_i(0)b_j^\dagger(\tau)e^{-\beta H} \right) = \sum_{n=0}^{\infty} \sum_{l=0}^n b_i H^l b_j^\dagger H^{n-l} \frac{(-\beta)^n}{n!}. \quad (5.24)$$

Insertion Probabilities

Inserting complete sets of states gives us the matrix elements which we will treat as weights, as usual. This means however, that we have to specify the weight we wish to give to the matrix element of the worm tail and the worm head. The conventional choice is to set these equal to unity, irrespective of the occupation before and after the worm operators. Another choice has been discussed in Ref. [96]. Whatever choice we make, it does not substantially alter the description of the algorithm. Note that the action of the worm operator on a basis state yields again a state proportional to one basis state.

We now have to set up a detailed balance for the transition from and to the extended configuration space, that is a detailed balance for inserting and annihilating a worm. From the description in words above, we know that the worm

motion finishes when the worm bites in its own tail. Suppose the initial worm pair is $b_i(0)b_i^\dagger(\epsilon, \uparrow)$, with the second operator the mobile worm which moves initially upwards in time. There are two possibilities to end the worm motion. First, the worm can go back to the time $t = 0$ on site i with an operator $b_i(\epsilon, \downarrow)$. Then the insertion probability for the reverse worm is always the same. Second, the worm can approach $t = 0$ on site i with an operator $b_i^\dagger(-\epsilon, \uparrow)$. The insertion probabilities must hence satisfy

$$P_{ins} [b_i^\dagger, n_i] = P_{ins} [b_i, n_i + 1], \quad (5.25)$$

on all sites i with occupation n_i . For a soft-core Bose-Hubbard model with particle number cut-off N_{max} a possible solution is [96]

$$\begin{aligned} P_{ins} [b_i^\dagger, n_i] &= \frac{1 - \delta_{n, N_{max}}}{2} \\ P_{ins} [b_i, n_i + 1] &= \frac{1 - \delta_{n, 0}}{2}. \end{aligned} \quad (5.26)$$

For hard-core bosons, one can use $P_{ins} [b_i^\dagger, 0] = 1$ and $P_{ins} [b_i, 1] = 1$, thus always inserting a worm.

Worm motion and efficiency

Let us now have a closer look at the process when we wish to swap $b_j(\tau \pm \epsilon)$ with an interaction H_b (occurring at time τ) in a way that satisfies detailed balance. If each of these steps satisfies detailed balance locally, then detailed balance will be satisfied globally as well. From experience we know that it is this swap update that has the largest impact on the efficiency of the method. The worm motion is completely determined by how the worm passes through and modifies the vertices. Suppose the worm head reaches a vertex at the leg left under (entrance leg), as in Fig. 5.2. The local configuration can then change according to the four processes bounce, straight, jump and turn, each with their proper weight $W_i, i = 1, \dots, n$. For models with number conservation ($U(1)$ symmetry), it is possible that one or more of the four processes cannot occur, so n can in principle be two, three or four. The bounce process, which means that the worm returns on its footsteps, is always possible but since it does not change the current vertex, it can be regarded as a waste of computer time. The worm head has to choose between one of the n processes, modifies

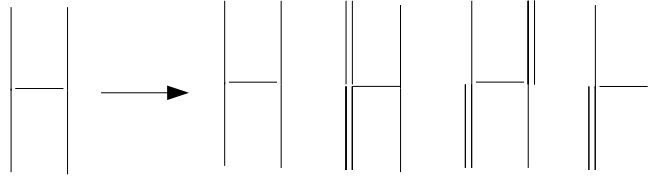


Figure 5.2 The four possible states that can arise when the worm enters the leftmost vertex at the leg left under in a number occupation basis and for a system with particle number conservation. A single line means that the leg is singly occupied, a double line means double occupancy and a dashed line denotes that the leg is not occupied. The four processes on the right correspond to bounce, straight, jump and turn, from left to right.

hereby the current vertex and goes consequently to the next vertex along the segment that connects the current exit leg and the next entrance leg. The probability matrix T_{ij} defines the transition from the entrance leg to the exit legs and hence completely determines the worm motion. We will now discuss several choices for this probability matrix T_{ij} .

Originally, the heat-bath updates [32], $T_{ij} = \frac{W_i}{\sum_j W_j}$, (solution A) were proposed. Secondly, in Ref. [33] it was realized that other choices were also perfectly possible. One has adopted the notion of directed loops for directing the worm head at the vertices in order to be more efficient than solution A. The rule of thumb is that the bounce processes should be as low as possible. This inspired the authors of Ref. [96] to numerically minimize the trace of the probability matrix T_{ij} with respect to detailed balance, $W_i T_{ij} = W_j T_{ji}$ (hereafter called solution B or the minimal bounce solution). They used a linear programming technique [97] for this purpose. Equivalently, one can say that this amounts to minimizing the sum of the eigenvalues of the transition matrix T_{ij} , $\min(\lambda_2 + \lambda_3 + \lambda_4)$. Thirdly, we propose to use the locally optimal probability matrix eq.(4.22) as transition matrix (solution C) for the scattering of the worm at a vertex.

Spin 3/2XY model. In Ref. [96] the directed loop algorithm was studied for the one dimensional spin 3/2XY model in an external magnetic field h ,

$$H = J \sum_{\langle i,j \rangle} \frac{1}{2} (S_i^+ S_j^- + S_i^- S_j^+) - h \sum_i S_i^z, \quad (5.27)$$

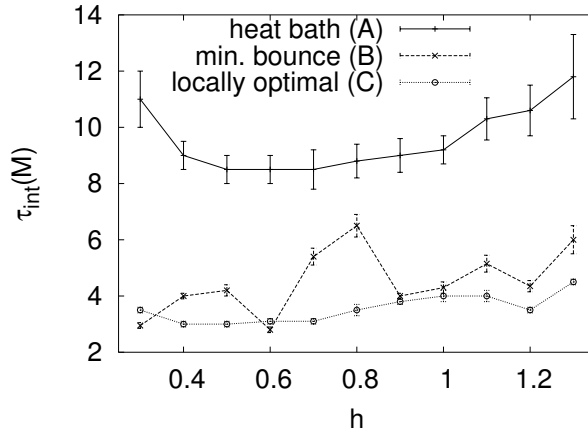


Figure 5.3 Integrated autocorrelation times for the magnetization, $\tau_{int}(M)$, as a function of magnetic field h for a spin $3/2 - XY$ model as in Ref. [96], lattice size $L = 64$, inverse temperature $\beta = 64$. The integrated autocorrelation times are made loop size independent (normalized to two worms per update) so that the heat bath (solution A), minimal bounce (solution B) and locally optimal (solution C) algorithms can directly be compared. The precise definition of these algorithms is explained in the text.

where the first sum extends over nearest neighbors and J is an exchange interaction term. It appeared that solution B always gave shorter autocorrelation times than solution A, as can also be seen in Fig. 5.3 and in Fig. 5.4, where the integrated autocorrelation times for the uniform magnetization and the energy are plotted.

We also addressed the spin $3/2 - XY$ model with solution C and the results for the integrated autocorrelation times for the magnetization and the energy are also presented in Fig. 5.3 and in Fig. 5.4. We find a substantial improvement over solution A. Solution C is also much better than solution B for magnetic fields around $h \approx 0.8$, while for other magnetic fields the difference is smaller. This indeed shows that minimizing bounces is not optimal for the spin $3/2XY$ model. Note that increasing the system size does not significantly change the ratio of the correlation times of solutions B and C.

Bose-Hubbard model. In the Bose-Hubbard model, the diagonal weights are relatively much larger compared to the non-diagonal weights than in spin systems. Again, as can be seen in Fig. 5.5, the heat-bath updates (solution A) are outper-

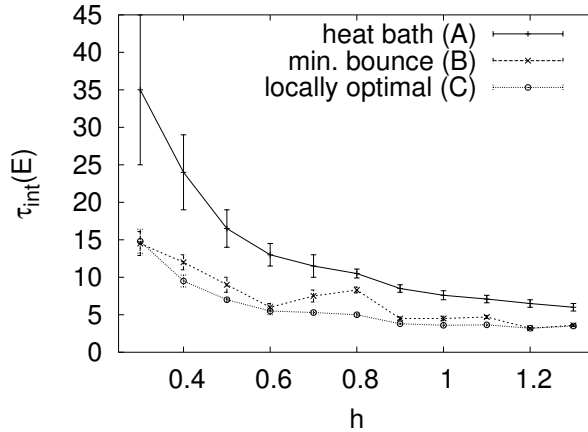


Figure 5.4 Analogous to Fig. 5.3 but now for the integrated autocorrelation time of the energy, $\tau_{int}(E)$, as a function of the magnetic field h .

formed, but for large on-site repulsion U the minimal bounce solution (solution B) is superior to the locally optimal solution (solution C).

As in the Potts model eq.(4.24), we are guaranteed that solution C is more efficient than solution A, but the Peskun theorem does not claim that solution C is superior to solution B, because choosing the lowest (local) λ_2 will not necessarily correspond to the lowest integrated autocorrelation time, τ_{int} (eq.(4.16)). Specifically, in case $n = 2$ both solutions reduce to Metropolis updating eq.(4.11). In case $n = 3$ solution B is of the form

$$T_{ij}^B = \begin{bmatrix} 0 & a & 1 - a \\ \frac{\pi_1}{\pi_2} a & 0 & 1 - \frac{\pi_1}{\pi_2} a \\ \frac{\pi_1}{\pi_3} (1 - a) & \frac{\pi_2}{\pi_3} - \frac{\pi_1}{\pi_3} a & \frac{2\pi_3 - 1 + 2\pi_1 a}{\pi_3} \end{bmatrix}. \quad (5.28)$$

The linear programming technique [97] applied in solution B will try to make $a = \frac{1-2\pi_3}{2\pi_1}$ if $\pi_3 < \frac{1}{2}$, otherwise it will take $a = 0$. It will be the system parameters that determine whether T^B or T^C (eq.(4.22) for $n = 3$) performs better. Due to its structure it is also not possible to improve T_B by Metropolizing it.

Also in case $n = 4$ both solutions B and C put all diagonal elements in the (local) stochastic matrix zero, except for the diagonal element corresponding to the largest weight. We know from the Peskun theorem (see section 4.2.4) that this leads to an

efficient sampling. As a counterexample, the Metropolized Gibbs sampler eq.(4.21) has only one zero on the diagonal of the transition matrix and is systematically outperformed by both solution B and C.

The class of locally optimal stochastic matrices can be parameterized as

$$T_{ij} = \begin{bmatrix} 0 & a & b & x \\ \frac{\pi_1}{\pi_2}a & 0 & c & y \\ \frac{\pi_1}{\pi_3}b & \frac{\pi_2}{\pi_3}c & 0 & z \\ \frac{\pi_1}{\pi_4}x & \frac{\pi_2}{\pi_4}y & \frac{\pi_2}{\pi_4}z & 1 - \frac{\pi_1x + \pi_2y + \pi_3z}{\pi_4} \end{bmatrix}, \quad (5.29)$$

with $x = 1 - a - b$, $y = 1 - \frac{\pi_1}{\pi_2}a - c$, $z = 1 - \frac{\pi_1}{\pi_3}b - \frac{\pi_2}{\pi_2}c$ and the three free parameters a, b and c . Solution B will now try to minimize T_{44} , or minimize a, b and c , under a number of constraints such as $a + b \leq 1$. This can be suboptimal however, since the minimum will be found when one or more of the constraints are exactly met [97]. Suppose the minimum is found for $a + b = 1$, as it happens in the spin $3/2XY$ model for magnetic fields $h \approx 0.8$. Then the scattering from the least probable state to the most probable state is zero, and this clearly cannot be optimal and explains why solution C is better in Fig. 5.3.

The overall conclusion is that the integrated autocorrelation times for both solutions B and C will be of the same order and roughly optimal. The important principle is that the diagonal elements corresponding to the lowest $n - 1$ weights should be zero. Some arbitrariness is still retained, but it does not seem possible to define how the remaining freedom should be chosen independently of the weights that occur in the updating process. When the diagonal and non-diagonal weights are of the same order, solution C is better, while for large diagonal weights solution B gives the lowest integrated autocorrelation times. Furthermore, we have a good argument why these solutions lead to a locally optimal sampling, based on the Peskun theorem (see section 4.2.4). We expect the same roughly optimal behavior for other observables than for the ones discussed here when solutions B and C are applied.

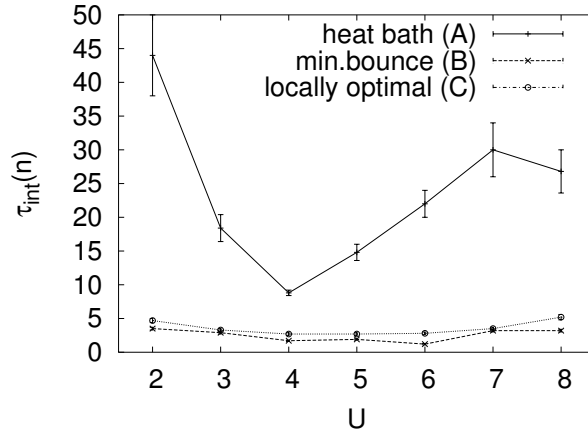


Figure 5.5 Integrated autocorrelation time for the density, $\tau_{int}(n)$, as a function of on-site repulsion U for a one-dimensional Bose-Hubbard model with $\mu = 5, t = 1$, lattice size $L = 64$ and inverse temperature $\beta = L$. Four loops were constructed in every update for the ‘min. bounce (B)’ and ‘locally optimal (C)’ algorithms, while for ‘heat bath (A)’ we constructed 16 loops and multiplied the results by four afterwards. Particle number cut-off is lowered at $U = 3$ and $U = 8$. The Mott phase sets in for $U > 9$.

Worm motion: remarks

The worm motion is such that particle number is increased (decreased) when the mobile worm of type $b^\dagger(b)$ goes around in imaginary time. We are thus working in the grand-canonical ensemble. There is also a finite probability that the worm can go around all sites in one coordinate direction and thereby changing the winding number. From these observations and the analysis given in the previous paragraph, we can conclude that the worm update is ergodic.

Let us think for a moment on how the worm can cross a vertex, and what more can be said about ‘bounces’ and ‘turns’. Suppose there is a worm $b_i^\dagger(\tau - \epsilon, \uparrow)$ approaching a vertex $H_b(\tau)$. Depending on the type of the interaction $H_b(\tau)$ three different cases can occur, that separate in two distinct classes.

First, for an interaction $H_b = b_i^\dagger b_j$ we have (written as operators)

$$\begin{aligned} b_i^\dagger (b_i^\dagger b_j) &\rightarrow (b_i^\dagger b_j) b_i^\dagger \\ &\rightarrow b_i^\dagger (b_i^\dagger b_j), \end{aligned} \quad (5.30)$$

corresponding to the 'straight' and 'bounce' processes, respectively. If we choose the worm weight as $f_i = \langle n_i | b_i^\dagger | n_i - 1 \rangle = \sqrt{n_i}$ (cf. Ref. [96]), then we can forget about the bounces, and the motion at this vertex is deterministic (we do not need to draw a random number). This is of course a consequence of the commutator $[b_i^\dagger, b_i^\dagger b_j] = 0$. This still holds for worm weights $f_i = \sqrt{n_i}/E_{d,i}$ with $E_{d,i}$ a parameter that can be chosen to optimize the efficiency of the algorithm and where d denotes the dependency on moving upwards \uparrow or downwards \downarrow in imaginary time.

The second class consists of the equations arising for vertices of the form $(n_i + n_j)$ and $b_i b_j^\dagger$. Specifically in the latter case we have

$$\begin{aligned} b_i^\dagger (b_i b_j^\dagger) &\rightarrow (b_i b_j^\dagger) b_i^\dagger \\ &\rightarrow (n_i + n_j) b_j^\dagger \\ &\rightarrow b_j^\dagger (n_i + n_j) \\ &\rightarrow b_i^\dagger (b_i b_j^\dagger), \end{aligned} \quad (5.31)$$

corresponding to the 'straight', 'jump', 'turn' and 'bounce' processes, respectively. These equations do not form a closed set, and couple to the equations originated by the vertex $H_b = (n_i + n_j)$. The specification of the algorithm requires a choice for the worm weights (for instance the f_i , or taking them all to be unity), and determining the transition probabilities for the 'straight', 'jump', 'turn' and 'bounce' processes in a way that satisfies the reversibility condition. The transition probabilities need to be determined for all two-particle states that can occur, and in general the transition probability for the turn and bounce processes will be nonzero. This is ultimately a consequence of $[b_i^\dagger, (b_i b_j^\dagger)] \neq 0$ and $[b_i^\dagger, (n_i + n_j)] \neq 0$. The ideas of 'locally optimal Monte Carlo' give a clue of how the transition probabilities are best chosen, assuming the worm weight is already fixed.

5.3 Observables

In this section we will discuss what kind of observables are in reach and how they are measured. Measurements are performed in a given configuration $\mathcal{C} = (|i\rangle, S_M)$.

- For a diagonal, local operator Q_i at site i ,

$$Q_i(\mathcal{C}) = \frac{1}{n} \sum_{p=0}^{n-1} \langle i_i(p) | Q_i | i_i(p) \rangle. \quad (5.32)$$

Densities and compressibilities belong to this class.

- A static density-density correlation function $C_{ij} = \langle n_i n_j \rangle$ has the estimator,

$$C_{ij}(\mathcal{C}) = \frac{1}{n} \sum_{p=0}^{n-1} \langle i_i(p) | n_i | i_i(p) \rangle \langle i_j(p) | n_j | i_j(p) \rangle. \quad (5.33)$$

Time-dependent local correlation functions have been discussed in the literature [28, 29].

- Estimators for the energy $E = \langle H \rangle$ and the specific heat $C = dE/dT$,

$$E = -\frac{1}{\beta} \langle n \rangle + N_b C_{\text{add}} \quad (5.34)$$

$$C = \langle (n - \langle n \rangle)^2 \rangle - \langle n \rangle, \quad (5.35)$$

follow directly from counting the number of non- $[0, 0]$ vertices in the operator string, corrected by the additive constant C_{add} . Similarly, estimators for the kinetic and the potential energy are obtained by counting the number of off-diagonal and diagonal vertices, respectively.

- The superfluid density (stiffness) ρ_s can be calculated using the winding number [98],

$$\rho_s(\mathcal{C}) = \frac{W^2(\mathcal{C}) L^{2-d}}{d\beta}, \quad (5.36)$$

where the winding number W denotes how many times the worldlines go around the lattice before closing on themselves again. The argument leading to eq.(5.36) only holds for configurations with positive definite weight, i.e. in the absence of any sign problem.

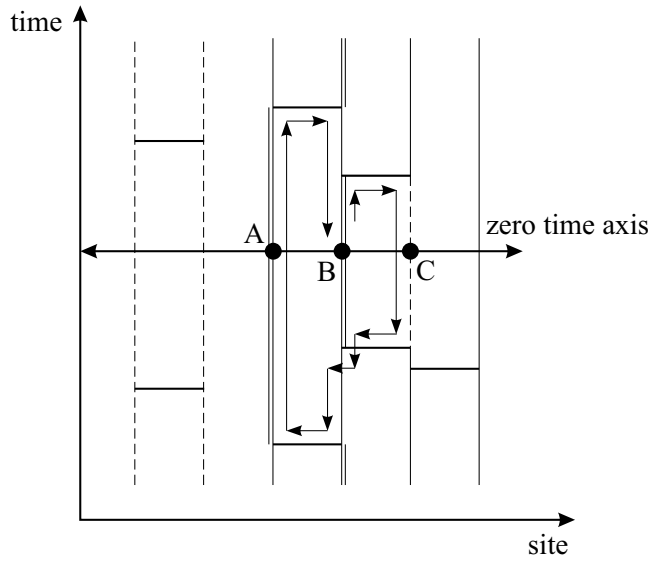


Figure 5.6 Measuring the equal time Green function in the stochastic series expansion. The configuration before the worm update is shown, together with the complete motion. The initial mobile worm annihilates a particle and moves upwards in time. Every time the mobile worm crosses the zero time axis, a measurement of the equal time Green function can be performed 'on the flight'. This is indicated by the thick dots and the letters A , B and C .

- We are also interested in the equal time Green function $\mathcal{G}(i, j) = \langle b_i^\dagger(\tau) b_j(\tau) \rangle$. From eq.(5.24) we see that the worm follows the distribution of the Green function. Let us draw a zero-time axis through the immobile worm, as in Fig. 5.6. We can make a measurement of the equal time Green function on the flight every time the mobile worm travels through the time axis [99, 100], as indicated by the letters A , B and C in Fig. 5.6. As an example, measurement B will contribute to the estimator of the local density on that site. With our choice of taking unity for the weight of the worm matrix elements, measurement C contributes a value of $\sqrt{2}$ to $\mathcal{G}(i, i + 1)$, while measurement A contributes a value of 2 to $\mathcal{G}(i, i - 1)$.

5.4 Application

The operator loop algorithm in the SSE representation has been successfully applied to spin systems, leading to unprecedented accuracy. In Chapter 6 the method

is applied to the one-dimensional Bose-Hubbard model approaching the Tonks regime, but here we want to show illustrative results for spin systems. Consider the one-dimensional spin 1/2-antiferromagnetic Heisenberg defined on a chain,

$$H = J \sum_{i=1}^L S_i \cdot S_{i+1}. \quad (5.37)$$

The Hamiltonian can be mapped to a system of hard-core bosons, and can after a Jordan-Wigner transformation be considered as an interacting one-dimensional fermion theory. Just as for one-dimensional bosons (as explained in Appendix A), the spin-1/2 system can be bosonized and the basic properties are those of a Luttinger liquid, meaning the absence of long-range order. Alternatively, the system can be studied exactly by the Bethe-ansatz [56]. The long range behavior of the equal time correlation function in the Luttinger Liquid region are [56]

$$\langle S^z(x) S^z(0) \rangle = C_1 \frac{1}{x^2} + C_2 (-1)^x \left(\frac{1}{x} \right) \ln^{1/2}(x), \quad (5.38)$$

where the C_i are non-universal amplitudes. In 1983 Haldane conjectured that only the half-integer spin chains are critical and that integer spin chains have an energy gap Δ [101, 102], leading to an exponential decay of the correlation function

$$\langle S^+(x) \cdot S^-(0) \rangle = e^{-x/\xi}, \quad (5.39)$$

with a finite correlation length $\xi \sim 1/\Delta$. Haldane's predictions have been confirmed in numerical and experimental realizations and constitute our basic understanding of (quasi) one-dimensional spin chains.

In Fig. 5.8. we show the correlation function $\langle S^+(x) S^-(0) \rangle$ for a spin-1/2 and spin-1 chain consisting of $L = 128$ sites at an inverse temperature of $\beta = 256$. In Fig. 5.7 the susceptibilities $\chi = \frac{\beta(\sum_i S_z(i))^2}{N}$ for the same spin-1/2 and spin-1 chain are shown for various chain lengths L and inverse temperatures $\beta = L$. For the spin-1/2 chain, the correlation function decays as a power law, and the susceptibility converges to a finite value for $1/L \rightarrow 0$. For the spin-1 chain, the correlation function decays exponentially and the susceptibility tends to zero for $1/L \rightarrow 0$. All our observations are in line with Haldane's predictions.

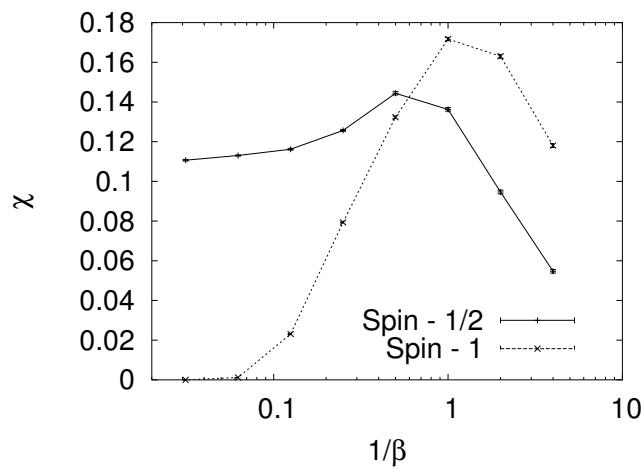


Figure 5.7 Spin susceptibility $\chi = \frac{\beta(\sum_i S_z(i))^2}{N}$ for a spin-1/2 and spin 1 chain consisting of $L = 128$ sites as a function of inverse temperature. The spin-1 chain is gapped while the spin 1/2 chain is critical (apart from the finite size gap).

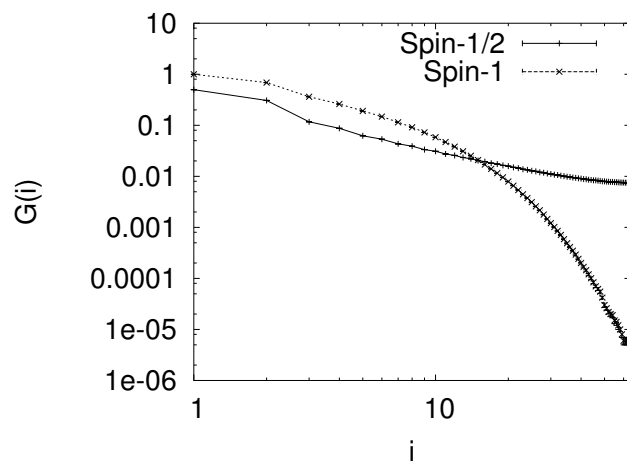


Figure 5.8 Spin correlation function $G(i) = S^+(0)S^-(i) + \text{h.c.}$ for a spin-1/2 chain and spin-1 chain consisting of $L = 128$ sites and at inverse temperature $\beta = 256$.

5.5 Worm algorithm : a locally optimal formulation

Quite generally, a worm algorithm is a quantum Monte Carlo algorithm based on a worldline representation where the decomposition eq.(5.4),

$$Z = \sum_{n=0}^{\infty} \int_0^{\beta} dt_n \int_0^{t_n} dt_{n-1} \cdots \int_0^{t_2} dt_1 e^{-t_1 H_0} V e^{-(t_2-t_1)H_0} \cdots e^{-(t_n-t_{n-1})H_0} V e^{-(\beta-t_n)H_0}, \quad (5.40)$$

is embedded in the extended configuration space

$$Z_e[U(i, j, \tau)] = \text{Tr} \left[\mathcal{T} \left(\left(b_i(0) b_j^\dagger(\tau) + b_i^\dagger(0) b_j(\tau) \right) \exp(-\beta H) \right) \right]. \quad (5.41)$$

While the choice $H_0 = 0, V = -H$ leads to the stochastic series expansion representation, the worm algorithm is obtained by collecting all diagonal one-body and two-body terms into H_0 (with respect to a chosen basis). Updates sample the Green function and are local in the extended configuration space. The directed loop algorithm is thus a special case of the worm algorithm (see also Chapter 7). In this section we think about a new formulation for the worm algorithm that incorporates the ideas of locally optimal Monte Carlo.

Compared to the original formulation of the worm algorithm by Prokofev *et al.* [31], the efficiency of the directed loop algorithm in the stochastic series expansion representation was found superior for spin systems and even for a homogeneous Bose-Hubbard model in both phases (except for the extreme soft-core case) [103]. This is an expected result for spin systems where the diagonal energies are of the same order as the spin exchange amplitudes, but for the Bose-Hubbard model this result feels unsatisfactory. For a trapped Bose-Hubbard model however, the worm algorithm was found superior [103].

The origins of the power of the directed loop algorithm are believed to be

- directed: the direction of the worm propagation does not randomly alter after an interaction is passed. This ensures large changes in configuration space along the imaginary time axis. The worm can also easily change from site.
- the concept of 'locally optimal Monte Carlo' is very powerful in the determination of how a worm has to pass (and modify) an interaction.

- Integrating out the imaginary times from the onset allows for a very efficient implementation with only integer number operations. The doubly linked list can be implemented by compiler optimized data structures.

On the down side, the need for a separate diagonal update and the construction of the doubly linked list in every step (a copy operation) are not present in the worm algorithm.

Inspired by these observations, we are looking for a worm algorithm that combines the best of both approaches and has the properties:

- the worm has the ability of inserting, passing and annihilating interactions. Detailed balance should be imposed between these processes using locally optimal Monte Carlo.
- due to the exponential factors representing the diagonal weights in eq.(5.40), imaginary time jumps by the worm are sampled using the exponential distribution. Compared to previous formulations of the worm algorithm [31, 100], we do not consider time intervals of constant energy, nor will we insert and annihilate interactions by jump/anti-jump processes.
- The worm is tagged by an extra label 'direction'. This label is dummy, as it does not appear in eq.(5.40). In addition, worms can be raising or lowering which is in a one-to-one correspondence with the direction of propagation for every Monte Carlo step. The direction of propagation can only change when the worm encounters an interaction.

We call the resulting algorithm the hybrid-worm algorithm. Note that this is not a 'new' algorithm, just another formulation of the worm algorithm, based on the ideas of locally optimal Monte Carlo. We describe it now in words (for the Bose-Hubbard model). Note that imaginary time now goes from 'left' to 'right' instead of from 'down' to 'up' (as in the directed loop algorithm), due to historical reasons.

1. Pick an arbitrary site and an arbitrary time and call it (i, τ) . Find the occupation on all sites at that particular time τ . A direction (left or right) is chosen with equal probability. Assume propagation to the right was chosen.

2. At (i, τ) a worm-pair (tail-head) is inserted. If the occupation is higher than zero, the worm-pair can be raising or lowering with equal probability. The occupation between worm tail and worm head is one higher for a lowering worm-pair. If the occupation at (i, τ) is zero, then with probability 50% a lowering worm is inserted, with probability 50% no worm is inserted. These insertion probabilities are thus the same as in eq.(5.26) for the directed loop algorithm.
3. When moving to the right (left), we call E the energy to the left (right) of the worm head. Draw an exponential deviate, $p = -\ln(u)$ with u an uniform random number, $0 < u \leq 1$. Evaluate the imaginary time shift window $\Delta\tau = p/E$ and the new worm time $\tau' = \tau + \Delta\tau$.
4. If the worm head encounters the worm tail during this propagation, the update ends with probability one and we arrive at a new diagonal configuration.
5. If the new worm time is larger than the time to the next interaction, the new worm time only equals the time of the next interaction. The worm can either bounce back or pass, annihilate or modify the interaction along the detailed balance rules defined below.
6. If no interaction is encountered in the imaginary time shift window, the worm can insert an interaction or bounce back.
7. Go back to step 3.

Observables, including the Green function, can be measured in the same way as discussed in section 5.3 for the directed loop algorithm.

We will now define the equations of detailed balance between inserting and annihilating an interaction. First, there are two simple cases. When the worm encounters an interaction that has no sites in common with the worm head, the worm can pass the interaction with probability one. This is a consequence of the commutator of the worm operator and the interaction being zero. Second, when a worm operator b_i^\dagger encounters an interaction $b_i^\dagger b_j$, it can pass the interaction with probability one. This is also the result of the commutator being zero. After passing an interaction, the diagonal energies change and a new exponential deviate must be

drawn.

The only interesting case happens when inserting an interaction, as depicted in Fig. 5.9. For the Bose-Hubbard model, an interaction can be inserted to both neighboring sites, meaning that we have to set up detailed balance between three different configurations. The configurations with an interaction inserted both have a total weight consisting of the weight of the interaction and the worm weight. The weight of the current configuration consists of the worm weight and a contribution E , resulting from the normalization of the exponential distribution. (Strictly speaking, the normalization factor is always present, but when the worm reaches an interaction, we have to integrate over all imaginary time jumps that would go beyond the interaction, hereby canceling the normalization factor. See also Chapter 7.) The transition matrix is a 3×3 matrix, and the ideas of locally optimal Monte Carlo can readily be applied. Other choices such as heat-bath updates are also possible, but they are expected to be less performant. If no interaction is inserted, the worm bounces back. If an interaction is inserted, the direction of propagation can be maintained.

Similarly, when a worm b_i^\dagger reaches an interaction $b_j^\dagger b_i$ diagram (b) in Fig. 5.9 from the left, the worm can either bounce back (b), annihilate the interaction (a) while keeping the the same direction of propagation or 'relink' the interaction as in (c), when the worm jumps to another site and changes its direction of propagation.

When the worm head reaches the worm tail, the Monte Carlo step is finished. Global detailed balance is satisfied, since the 'reverse' worm can be constructed using the same numerical recipe as described above. The algorithm described above is valid not only when the diagonal energies involve one site only, but also when the diagonal energies contain nearest neighbor repulsion repulsion terms.

5.6 Is the hybrid-worm algorithm efficient?

Although we have argued why we believe the proposed hybrid-worm algorithm should be efficient, there is only one way to actually find out whether it is efficient

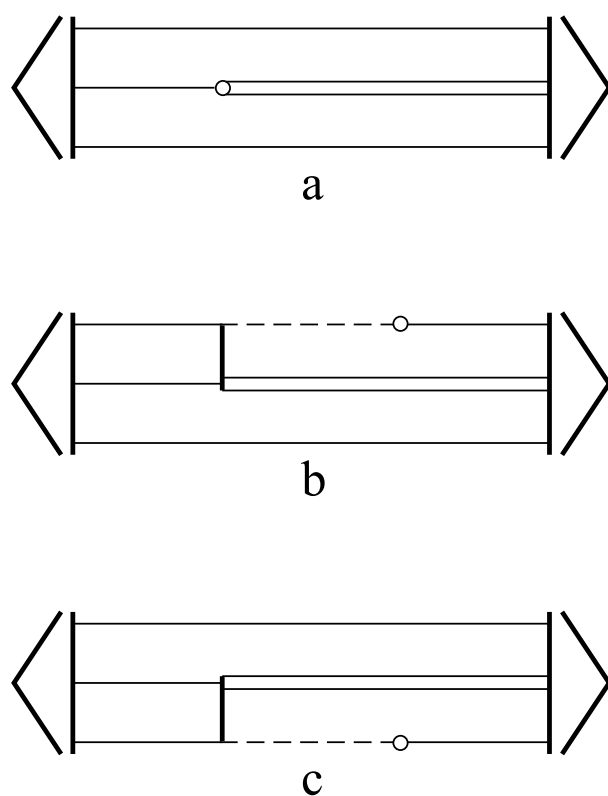


Figure 5.9 When the worm moves to the right and tries to insert an interaction in configuration (a), the two possible new configurations are configurations (b) and (c). The third possibility is bouncing back and changing direction in configuration (a). The transition matrix is thus a 3×3 matrix. Interactions are denoted by a full vertical line, the worm by a circle.

or not: that is to do the calculations and compare the efficiency with the directed loop algorithm.

We have calculated the standard deviations on the kinetic energy and on the squared density for a Bose-Hubbard model of 32 sites at an inverse temperature of $\beta = 32$ and with a fixed chemical potential $\mu = 2$. Simulations consisted of 40 bins that each ran 300 seconds on a Pentium III processor. The directed loop algorithm had a particle number cutoff of ten particles per site for $U = 1, 2$ and $U = 3$, while a cutoff of five particles per site was taken for the other values of U . The number of loops per update was optimized such that on average twice the number of vertices are visited. The Mott phase is reached for $U = 6$, from which value of U on only two loops per update are performed.

We have calculated the standard deviation on the kinetic energy and on the density squared (i) for the directed loop algorithm in the stochastic series expansion framework. (ii) for the hybrid worm algorithm where the diagonal energies are shifted by a constant in order to make them non-negative (iii-iv) for the hybrid worm where the energy-difference between the diagonal configurations to the left and to the right of the worm has been taken as the diagonal energy E , and where detailed balance between inserting and annihilating interactions has been imposed by (iii) heat-bath updates eq.(4.13) or (iv) by locally optimal updates, eq.(4.22). In Figs. 5.10 and 5.11 the results for algorithms (i) and (iv) are shown.

Among the different hybrid worm optimization parameters, approach (iv) is almost always the most efficient one. It is ten percent better than approach (iii) over the entire parameter regime. The directed loop algorithm seems to be the preferred model for very low values of U when looking at the kinetic energy but not at the squared density. The kinetic energy has an anomalously high integrated autocorrelation time for the hybrid worms (iii) and (iv); the reason for which is not yet fully understood. Algorithm (ii) gives the lowest error bars on the kinetic energy deep in the Mott phase, but it is outperformed for other observables. Finally, we agree that it is not unambiguous how the directed loop simulations should be performed in the Mott phase.

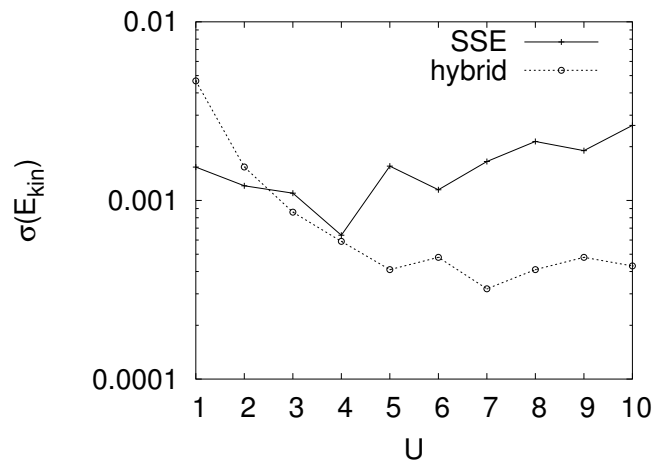


Figure 5.10 Standard deviation on the kinetic energy for the directed loop algorithm in the stochastic series expansion framework (SSE), and the hybrid worm using the energy difference and locally optimal updates (hybrid). The accuracy of the data points is about ten percent. (see also text).

In conclusion, the hybrid worm looks like an interesting algorithm to do simulations. At first, it seems better than the directed loop algorithm for the homogeneous Bose-Hubbard model, but this conclusion could be observable dependent. At this point, larger simulations are needed, and it would also be interesting to test it for spin systems, where the diagonal energies are more of the same order as the spin exchange energy terms. An important difference in the implementation of both algorithms is the use of the different data structures.

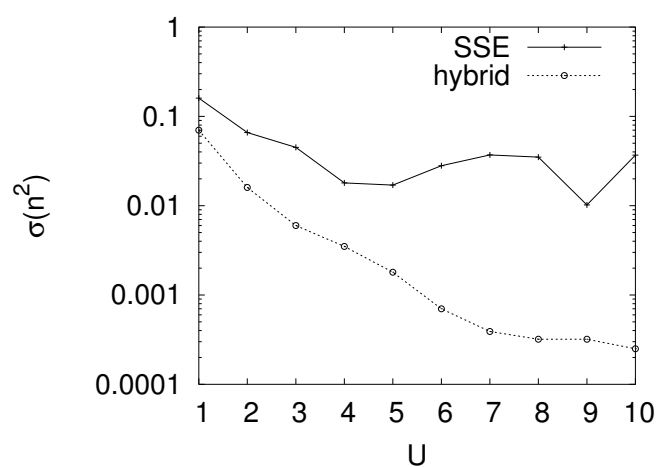


Figure 5.11 Standard deviation on the squared density for the directed loop algorithm in the stochastic series expansion framework (SSE), and the hybrid worm using the energy difference and locally optimal updates (hybrid). The accuracy of the data points is about ten percent. (see also text).

Chapter 6

Tonks gas

We have already opened the discussion on a Tonks-Girardeau(TG) gas in Chapter 2. When the repulsion between the bosons is so strong, they behave like effective hard-core bosons (in the Bose-Hubbard model this occurs for a very large U) and, in one dimension, they share many properties with fermions. For instance, TG bosons have the same energy and density as fermions do but have a different correlation function.

Initially, the regime of strong repulsions between bosons has been studied experimentally [12] and theoretically [104, 105] for an atomic gas not subject to an optical potential, but the acquired values for the ratio of the repulsive interaction strength to the kinetic energy were rather low and the TG regime was not seen. By using an optical lattice, much higher values for this ratio could be reached, resulting in the first successful experimental realization of a TG gas [13]. Recently however, another experiment without the use of an optical lattice claimed to have seen the Tonks limit [14].

Similar to the experiment on the superfluid-Mott transition [6], the interpretation of the experiment in Ref. [13] is complicated by the finite-size effects due to the harmonic trap. Even in the homogeneous case, an accurate theoretical description of the transition from a weakly interacting Bose gas to a strongly interacting Tonks gas has to rely on numerical simulations. In this chapter, our aim is to model the experimental results of Ref. [13] using one single numerical framework which accommodates both the weakly and the strongly interacting regime. The TG regime is

characterized by the absence of double occupancies in the many-boson wave function. To identify the TG regime unambiguously, one has to evaluate whether the experimental results are better described by soft-core bosons with a considerable overlap or by hard-core bosons for which double occupations are explicitly suppressed.

First, we discuss the experiments on the TG gas, subsequently we present our simulations for the experiment on the lattice. We also briefly comment on the experiment by Kinoshita *et al.* without a lattice that has reached the Tonks limit [14].

6.1 Experiments

For the experiment performed with the optical lattice [13], a rather small Bose-Einstein condensate of $3 - 4 \times 10^4$ Rb atoms with atomic mass $m = 87$ is put in a magnetic trap. Two orthogonal standing laser waves with a wavelength of 823 nm are imposed on the condensate, creating a two-dimensional optical lattice along the y and z directions. An array of one dimensional quantum gases in the x direction confined to narrow potential tubes results. The tunnel coupling between the tubes decreases exponentially by gradually increasing the transversal optical potentials to $27E_R$. In the axial direction the gases are trapped with a frequency of $\omega_{ax} = 2\pi \times 60\text{Hz}$. After a hold time of 10ms, the intensity of the laser along the axial direction is ramped up to a final depth of $18.5E_R$ with a wavelength of $\lambda_{ax} = 854$ nm. The axial momentum distribution of the quantum gases is probed by the standard imaging of the atomic cloud during ballistic expansion after a time-of-flight period of 16 ms. Before all optical and magnetic trapping potentials are switched off however, the confinement in the axial direction is reduced by lowering the lattice potential along the z direction to $6E_R$ within a time period of $100\mu\text{s}$. A ramp down is also used along the x -axis, enhancing the number of atoms in the central momentum peak. This is not fully non-adiabatic and it is believed to lead to a narrowing of the Gaussian envelope in the observed momentum distribution by $\sim 20\%$. An example of an experimental momentum profile is shown in Fig. 6.1 for an axial optical lattice potential strength of $V_0/E_R = 5.6$ (corresponding to a ratio of $U/t = 7.8$ in the Bose-Hubbard model) together with the momentum profile obtained using fermionization theory (see section 2.7.2). For comparison, the

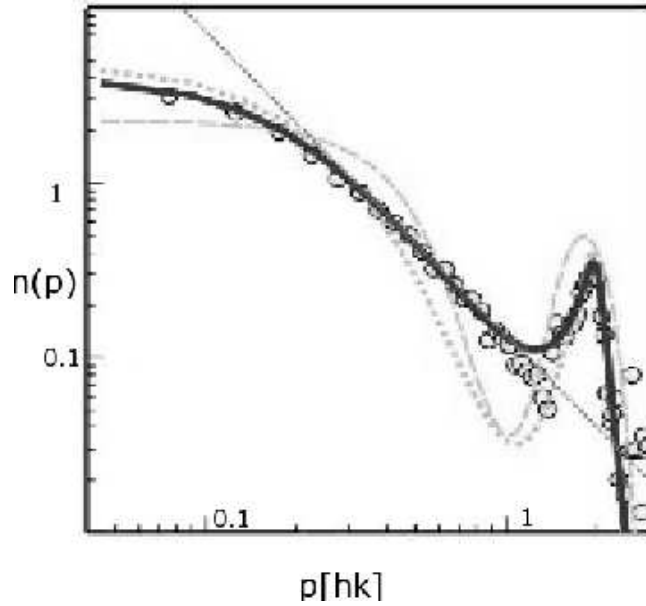


Figure 6.1 Momentum profile of a one-dimensional quantum gas subject to an axial lattice potential depth of $V_0/E_R = 5.5$ ($U/t = 7.8$). On the x -axis the momentum p is shown in units of $\hbar k$. The momentum profile reaches a minimum at $p = \hbar k$ and a maximum at $p = 2\hbar k$. For repulsion strengths U/t stronger than $U/t > 5$, fermionization theory gives accurate results. The experimental data (circles) are shown, together with the predictions from fermionization theory (thick full line), obtained at finite temperature and with averaging over the tubes. The momentum profiles for the ideal Bose (short dashed line) and ideal Fermi gas (long dashed line) are also displayed for comparison. It was assumed that there are 18 particles in the central tube. The figure has been taken from Ref. [13].

results for a non-interacting Bose gas and for a non-interacting Fermi gas are also shown. All these momentum profiles have been obtained assuming a Thomas-Fermi density profile (see eq.(1.5)) in every tube [4], and the averaging over the tubes in the fermionization theory is carried out by a fitting procedure where only the number of atoms in the central tube is a fitting parameter. Temperature has been calculated by assuming conservation of entropy during the ramping up of the axial lattice [13]. Fermionization gives good agreement with the observed profiles from values of $U/t \approx 5$ on. Note that the momenta p have been expressed in units of photon momenta $\hbar k$, and that the peak at $p = 2\hbar k$ corresponds to the first order diffraction peak due to the lattice.

The second successful experiment will only briefly be described here [14]. A

condensate of ^{87}Rb atoms is confined in an array of one-dimensional parallel tubes by a blue-detuned two-dimensional optical lattice. Along the tubes the condensates are confined by a red-detuned crossed dipole trap. In contrast with the experiment described above, there is no lattice here along the axial direction. The transverse confinement can be made tighter leading to an increase in the ratio between mean potential and kinetic energy, $\gamma = E_{int}/E_{kin}$. Strengthening the axial confinement would decrease γ . The temperature T_{1d} , related to the measured energy via $E = k_B T_{1d}/2$, is shown in Fig. 6.2 as a function of the lattice depth U_0 which is expressed in terms of the recoil energy. At low trap power, $P = 12$ mW in Fig. 6.2(A), the atoms approach the TG regime, while at high trap power, $P = 320$ mW in Fig. 6.2(B), the atoms act more like a BEC. The measured data are compared to non-interacting fermions (fermionization theory, see section 2.7.2), to mean-field theory (Bogoliubov approximation, see section 2.5.2) and to the exact solution of the one-dimensional Bose Gas with delta interaction in the thermodynamic limit (Lieb-Liniger model [59]). These curves contain no free parameters. Error bars in the theory curves reflect the uncertainty in the crossed dipole trap size and the atom number (54 ± 6 atoms in the central tube). The system is purely one-dimensional only above $U_0 > 20E_R$ when the interaction between the tubes is negligible.

6.2 Simulations

We can apply the lowest-band calculation of section 2.1 in order to obtain the one-dimensional Bose-Hubbard model and relate its effective parameters to the experimental input parameters. The Bose-Hubbard model is able to describe the transition to the Tonks-Girardeau limit, and is our preferred model to study the Tonks-Girardeau limit for ultracold atoms in an optical lattice. We thus start from the Bose-Hubbard Hamiltonian,

$$H = -t \sum_{\langle i,j \rangle} b_i^\dagger b_j + \sum_i (\epsilon_i - \mu) n_i + \frac{U}{2} \sum_i n_i (n_i - 1), \quad (6.1)$$

with the same conventions and notations as in Chapter 2, and where the ϵ_i term represents the harmonic magnetic trapping. The main uncertainties in the model originate from the experimental uncertainty on the scattering length a_s [106] which is involved in the renormalization of the effective parameters of the Bose-Hubbard

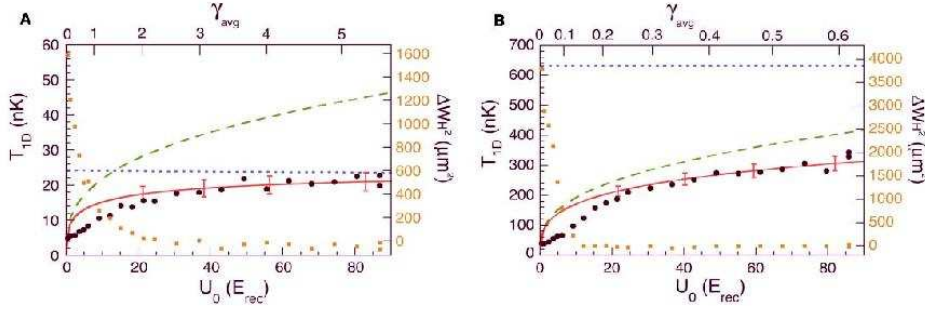


Figure 6.2 Temperature (denoted by circles) of the gas as a function of the lattice depth U_0 and the corresponding values of γ . At low trap power, $P = 12$ mW in (A), the atoms approach the TG regime, while at high trap power, $P = 320$ mW in (B), the atoms more act like a BEC. Non-interacting fermions are represented by short dashed lines and are valid at $\gamma \gg 1$, mean-field theory (Bogoliubov approximation) is represented by long dashed lines and is valid at $\gamma \ll 1$, while the exact one-dimensional Bose-gas (Lieb-Liniger model) is valid at all values of γ and is represented by a solid line. The solid squares represent the change in square of the horizontal width, ΔW_h^2 , after the crossed dipole trap has been shut off. Figure taken from Ref. [14].

model. As we work in the grand-canonical ensemble, the chemical potential μ must be fine-tuned such that the expected number of particles corresponds to the experimental number of particles. The Bose-Hubbard model is simulated using the directed loop algorithm in the stochastic series expansion representation [32] (SSE) with locally optimized loop updates [33, 107] (see Chapter 5). From this Monte Carlo simulation, thermodynamic observables such as the energy, the (local) density, the (local) compressibility and the one-body correlation function can be computed exactly in a statistical sense [99, 100], as has been explained in detail in Chapter 5.

6.2.1 Homogeneous system

First, we consider a homogeneous ($\epsilon_i = 0$) atomic gas in a lattice of $L = 128$ sites with periodic boundary conditions at a very low but finite temperature, $T/t = 0.2$. In Fig. 6.3 we show the internal energy per site of this system for increasing values of U/t , keeping the average density fixed at $\langle n \rangle \approx 0.5$. An ideal Bose gas occurs in the limit of vanishing U , which is indicated by the lower horizontal line in Fig. 6.3, while the ideal Fermi gas is found for $U \rightarrow \infty$ and is indicated by the

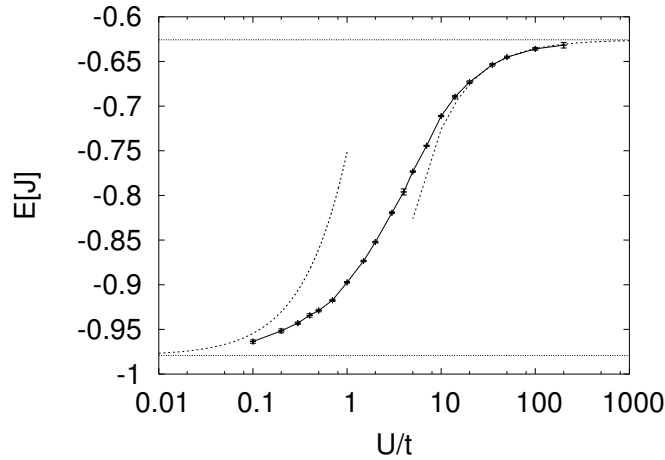


Figure 6.3 Internal energy per site as a function of U/t for a homogeneous model with 128 sites at a temperature $T/t = 0.2$. The data points with error bars connected by the full line are the energies obtained by the SSE method. The energies for non-interacting fermions (upper dotted horizontal line) and non-interacting bosons (lower dotted horizontal line) are shown, together with the Bogoliubov approximation for bosons (dashed line on the left) and a first order perturbation theory for fermions (dashed line on the right).

upper horizontal line. For very large values of U/t , no site of the lattice will be doubly occupied and one can apply the Jordan-Wigner transformation to map the bosons onto fermions [9]. For small but finite U ($U/t \ll 0.1$ in Fig. 6.3), the system is adequately described by the standard Bogoliubov approximation [43]. For large U a perturbation of interacting fermions was derived in Ref. [63] to order $1/U$. From the log scale in Fig. 6.3, it appears that the limit of non-interacting fermions is reached slowly for values of $U/t > 10$. For $U/t \sim 1$ one has to resort to numerical methods, and we see that the SSE method remains efficient over the entire U/t range. Higher temperatures lead qualitatively to the same results, but the description in terms of fermions is only valid for higher values of U/t . Temperature can be seen as a source for exciting double occupancy on a particular site, whose likelihood must be suppressed by a stronger on-site repulsion term. Because the density $\langle n \rangle \approx 0.5 < 1$, we expect the physical picture here to be the same as for the Bose gas in the continuum in the experiment by Kinoshita *et al.* [14]. The experimentalists claim to reach the Tonks limit for $U/t \approx 5$, although it is not unambiguous to define what 'reach' means, seen the fact that Tonks behavior can strictly speaking

only occur at $U/t = \infty$. From our simulations, there is still a rather large difference in energy between soft-core bosons and non-interacting fermions at this value of U/t . All one can safely say, is that the interaction energy scale for going over from the weak to the strong interacting regime occurs at $U/t \approx 2$. This holds for both the experiment by Kinoshita *et al.* [14] and our simulations.

6.2.2 Inhomogeneous system.

The harmonic trapping potential breaks the homogeneity of the system. For the parameters we follow Ref. [13]: the scattering length a_s of Rb atoms is taken to be $a_s = 102(6)a_0$ [106], with a_0 the Bohr length; the characteristic length a_\perp of the tight confinement in the y and z direction is $a_\perp = 57.6\text{nm}$; the parameter ϵ_i in eq.(6.1), characterizing the trapping in the axial direction, is given by $\epsilon_i = \int dx V_T(x) |w(x - x_i)|^2 \simeq 8 \times 10^{-4} E_R (i - \frac{L}{2})^2$, with $w(x - x_i)$ the Wannier function centered around site i and $L = 50$ the total number of sites. The ratio U/t can be varied by changing the optical potential strength V_0 . The temperature T and the number of particles in one tube are not directly accessible experimentally. The averaging over an array of one-dimensional tubes in Ref. [13] can be understood as an averaging over condensates with different temperatures and particle numbers. However, one can understand the onset of the TG limit from simulations for a single tube with a fixed temperature. We used $T/t = 1$ at all interaction strengths, which is of the same order as the temperatures estimated in Ref. [13].

In Fig. 6.4 the local densities and the momentum profiles are shown for several values of the optical potential strength V_0 , in line with the actual values used in the experiment of Ref. [13]. All Monte Carlo simulations consist of at least 20 chains of 2^{16} samples with each 50 – 200 off-diagonal updates such that error bars are not visible. Momentum profiles are experimentally measurable and can be calculated from a numerical simulation as (eq.(2.19))

$$n(p) = |w(p)|^2 \sum_{j,l} e^{-ip(j-l)} \langle b_j^\dagger b_l \rangle, \quad (6.2)$$

where the envelope $w(p)$ is the Fourier transform of the Wannier function $w(x)$, p denotes momentum in units of $\hbar k$ and $\langle b_j^\dagger b_l \rangle$ is the one-body density matrix of the Bose-Hubbard model. In Fig. 6.4, the peak observed at $p = 2\hbar k$ is the first-order

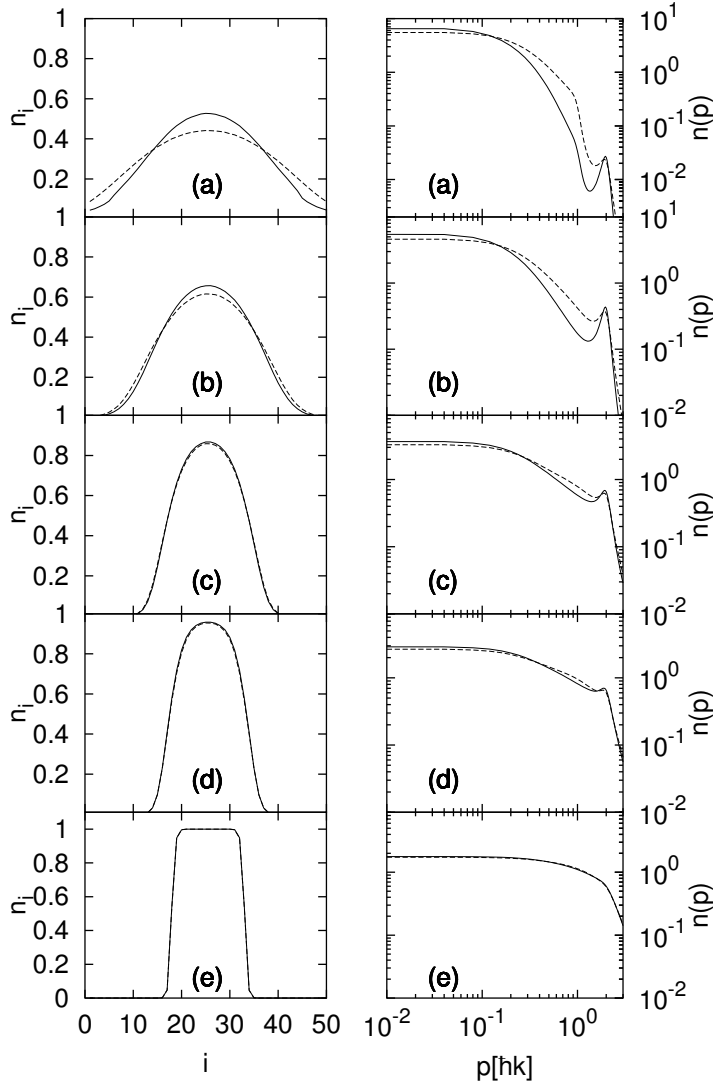


Figure 6.4 Local densities n_i in coordinate space as a function of the site index i (left) and the corresponding momentum profiles $n(p)$ as a function of the momentum p (in units $\hbar k$) on the right. The axial optical lattice depths, the ratios U/t and the values of the slope parameter α for soft-core (full line) and α' for hard-core bosons (dashed line) are (a) $V_0/E_R = 1, U/t = 1.75, \alpha = 2.71, \alpha' = 1.69$, (b) $V_0/E_R = 5, U/t = 7.85, \alpha = 1.92, \alpha' = 1.38$, (c) $V_0/E_R = 9.5, U/t = 28.6, \alpha = 1.00, \alpha' = 0.78$, (d) $V_0/E_R = 12, U/t = 52.28, \alpha = 0.72, \alpha' = 0.56$, (e) $V_0/E_R = 20, U/t = 258.54, \alpha = 0.33, \alpha' = 0.32$. In each plot the average number of particles is $\langle N \rangle \approx 15$, the temperature is $T/t = 1$, and the lattice consists of 50 sites.

diffraction peak reflecting the presence of the optical lattice. The ratio between the height of the central peak and the first-order peak is solely related to the width of the Wannier orbitals and is not affected by averaging over the array of tubes nor by the dynamics of the Bose-Hubbard model. The procedure to calculate the Wannier orbitals outlined in section 2.1, yields ratios in good agreement with the experimental data shown in Fig.2 of Ref. [13]. This suggests that the ramping down along the axial direction in the experiment proceeded adiabatically, and it demonstrates that the discrete Bose-Hubbard model is a valid approach to describe the physics of ultracold atomic alkali gases in optical lattices.

In every subplot (a-e) of Fig. 6.4 there is a region where the slope of the momentum distribution is almost linear (on log-log scale), similar to what occurs in an infinite homogeneous Tonks gas at $T = 0$, which has an infrared divergence $n(p) \propto p^{-1/2}$ at low momenta and an asymptotic tail $n(p) \propto p^{-4}$ at high momenta [108, 109]. In our case, the periodicity of the optical lattice sets an upper momentum scale $p_L = \hbar k$. The width of the Wannier orbitals sets another upper scale, $p_W \simeq (V_0/E_R)^{1/4} p_L$, which turns out to be larger than p_L for the parameter regimes considered here. The harmonic trap sets a lower momentum scale $p_T = (m\hbar\omega)^{1/2} \simeq 0.1\hbar k$, below which the momentum distribution is flattened because of the suppression of long-range correlations. Due to the trapping potential, the influence of temperature on the momentum distribution will be different from the homogeneous case: thermal fluctuations occur at the edges of the cloud and therefore they mainly affect the momentum distribution below p_T . Only the momentum distribution in the region between p_T and p_L relates directly to the short-range dynamics of the Bose-Hubbard model and might show a power-law behavior similar to the homogeneous system. We have fitted the linear parts of the log-log curves in this region with a power law $n(p) \propto p^{-\alpha}$. The slope α is sensitive to temperature, density and interaction strength, but to first order independent of the Wannier orbitals. By comparing the results for soft-core and hard-core bosons in Fig. 6.4, one sees that the TG regime is approached for optical potentials $V_0/E_R = 9.5$ and $V_0/E_R = 12$, while the agreement between hard-core and soft-core bosons is even better at $V_0/E_R = 20$, which in our model corresponds to a ratio $U/t = 259$. These values are in line with Fig. 6.3, where the energy for

$U/t = 200$ is only 4% lower than the energy of an ideal Fermi gas. For lower optical potentials, finite boson-boson interactions certainly need to be taken into account and double occupancies in the center of the trap do play an important role.

We see in subplot (e) of Fig. 6.4 that a Mott-like region is formed in the center of the trap. For a homogeneous system in the Mott phase, the dispersion relation of the excitations has a gap of order U [42], meaning that the role of double occupancies is strongly suppressed [110]. The Mott phase is entered at a ratio U/t as low as 1.67 at $T = 0$ for a density of one particle per site [72]. For the inhomogeneous system, the insulating behavior translates into a local compressibility (in fact the variance) that tends to vanish in the center of the trap [74]. Hence, for $T \ll U$ hard-core bosonic behavior can be reached for local densities varying from $\langle n_i \rangle = 0$ to $\langle n_i \rangle = 1$. However, the reduced local compressibility does not mean that for higher densities the TG regime would be reached at weaker optical potential strengths. Fig. 6.5 shows that a significant difference between the soft-core and hard-core momentum profiles persists even if the density-profile develops a Mott-like region, at an intermediate optical lattice strength $V_0/E_R = 7$ ($U/t = 14.3$). This indicates that the short-range correlations in the Mott-like region differ significantly from the short-range correlations in the TG regime.

The systems we have discussed so far are certainly not in the ground state. It might be possible to decrease temperature further by a factor of the order of ten [111]. We have simulated the system for decreasing temperature at a fixed optical potential strength of $V_0/E_R = 4.6$ ($U/t = 6.75$), with 18 particles confined in the trap. The results are shown in Fig. 6.6, where we see that the momentum profiles remain similar, only the difference in the heights between $p = \hbar k$ and $p = 2\hbar k$ gets a boost. For low enough temperatures, the momentum profiles are flattened for momenta smaller than the characteristic momentum scale set by the magnetic trapping, p_T .

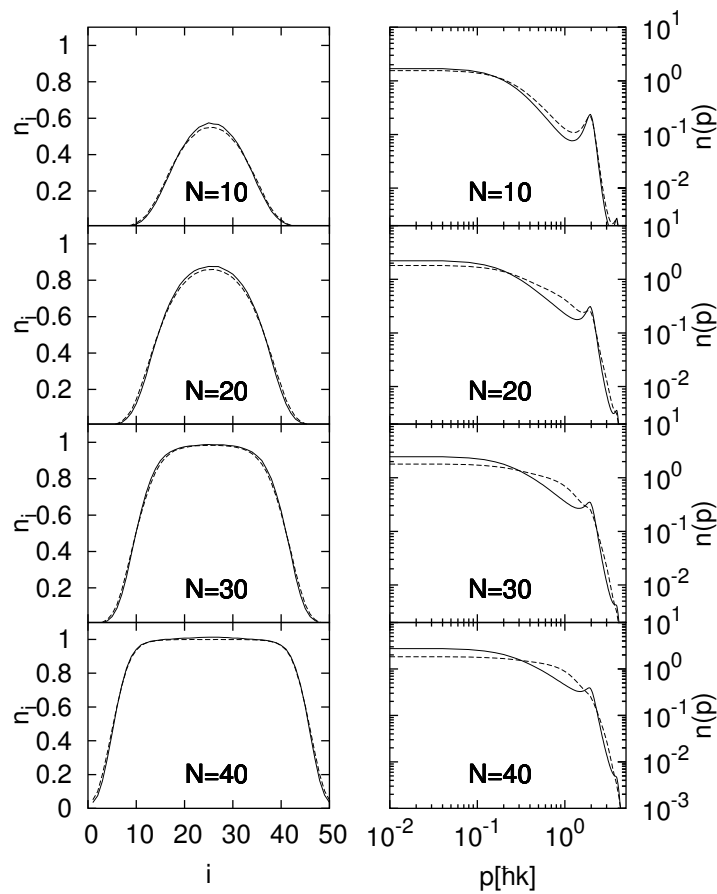


Figure 6.5 Density profiles n_i and momentum density profiles $n(p)$ (p in units $\hbar k$) for different fillings N at an optical lattice potential $V_0/E_R = 7$ and temperature $T/t = 1$, for soft-core (full line) and hard-core bosons (dashed line).

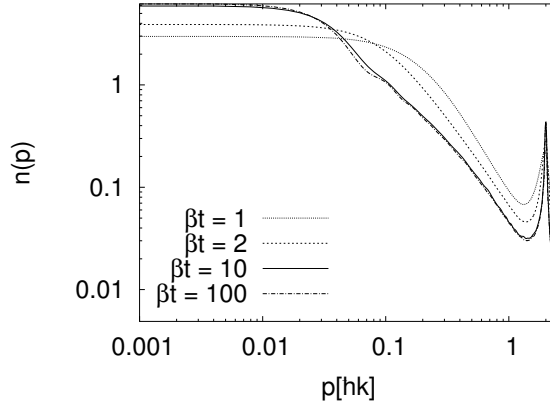


Figure 6.6 Momentum density profiles $n(p)$ (p in units $\hbar k$) at different inverse temperatures β for an optical lattice potential $V_0/E_R = 4.6$ ($U/t = 6.75$) for 18 particles confined in the trap.

6.3 Conclusions and Outlook

Our simulations lead to the conclusion that the discrepancy between soft-core and hard-core bosons remains non-negligible (even in the strongly interacting regime) up to the strongest optical potentials studied. The TG limit is reached gradually, and perfect agreement between soft-core and hard-core bosons occurs only at infinite repulsion. This means that the original interpretation, namely the fermionization theory (see section 2.7.2) by B. Paredes *et al.* [13], needs to be readjusted. Furthermore, we found that the short-range correlations in the Mott phase do not enhance the onset of TG behavior.

An interesting question is why the fermionization theory by B. Paredes *et al.* [13] did give good quantitative results for repulsion strengths $U/t \approx 5$. There are two possible explanations: On the one hand, one can say that the difference between the slopes in the momentum profiles between the hard-core and the soft-core bosons is too small. Any fitting procedure that performs an average over the tubes whitewashes the difference in momentum profile between soft-core and hard-core bosons and automatically leads to the experimentally observed profiles. Such an interpretation is in favor of the use of the fermionization theory. On the other hand, one can argue that, on basis of our simulations, the difference in momentum pro-

files between soft-core and hard-core bosons should remain after an averaging procedure has been applied. The momentum profiles have only two characteristic features, a height and a slope, while there are two unknowns (which are then the fitting parameters): the temperature and the number of particles. Then the averaging procedure itself should be held responsible for the 'unexpected' good results of the fermionization theory. Clearly, this discussion could be resolved if the experiment were performed on a single one-dimensional tube, but then the noise would prevent the detection of any signal.

Recently, S. Wessel *et al.* looked into the TG problem by using the same Monte Carlo method as we did [103]. Their simulations were performed for the ground state only and did not take the momentum profile of the Wannier state into account. They stressed the fact that no finite U/t exists when the Tonks gas sets in, since good agreement between hard-core and soft-core bosons is also dependent on the observable under investigation. In the low density region, the momentum profile was found rather insensitive to the value of U/t , allowing a description in terms of a TG gas already at very small values of U/t . Near the boundary of the system, the local density was close to the hard-core limit for all values of $U/t > 5$. For higher densities, larger values of U/t are needed in order to observe the behavior of a Tonks gas.

Let us come back to the disappearing of the first-order diffraction peak in the experiment on the superfluid to Mott transition by Greiner *et al.* [6]. As explained in Chapter 3, this was first attributed to entering the Mott region in the center of the trap. Later this viewpoint was contested [78]. From Fig. 6.4 we can conclude that the disappearing of the diffraction peak happens when the bosons behave as hard-core bosons (also in three dimensions) [112] and has indeed nothing to do with entering the Mott region in the center of the trap.

Chapter 7

Canonical algorithms

In this chapter a worm algorithm in the canonical ensemble is introduced. Just as with the quantum Monte Carlo algorithms presented so far, the updates consist of a local sampling of the Green function. The algorithm is applied to the Berezinskii-Kosterlitz-Thouless phase transition [50, 51], which is dominated by phase fluctuations and occurs at the tip of the Mott lobes in the Bose-Hubbard model.

7.1 Canonical Worm algorithm

Recall the decomposition of eq.(5.40) for the partition function,

$$Z = \sum_{m=0}^{\infty} \int_0^{\beta} dt_m \int_0^{t_m} dt_{m-1} \cdots \int_0^{t_2} dt_1 e^{-t_1 H_0} V e^{-(t_2-t_1)H_0} \cdots e^{-(t_m-t_{m-1})H_0} V e^{-(\beta-t_m)H_0}. \quad (7.1)$$

In the canonical worm algorithm local updates for the operator

$$U(\beta, \tau) = e^{-\tau H} A_{\alpha} e^{-(\beta-\tau)H} \quad (7.2)$$

are defined hereby generating a random walk in the extended configuration space. The parameter τ can be considered as the imaginary time at which the worm operator is inserted in the propagator $\exp(-\beta H)$. The worm operator is of the form

$$A = \sum_{\alpha} A_{\alpha} = \sum_{ij} A_{ij} a_i^{\dagger} a_j, \quad (7.3)$$

where α is a shorthand notation for i and j , which can be any two sites. The coefficients A_{ij} can be chosen at will: they can be constants, but it could also be interesting to use a function that contains a priori information about the behavior of the Green function. The idea of the algorithm is that the operators $a_i^\dagger a_j$ propagate simultaneously at all times such that total particle number cannot change. The worm has the ability to insert and annihilates interactions, justifying the name canonical worm algorithm.

When the worm operator is added to the propagator $\exp(-\beta H)$ and complete sets $\sum_i |i\rangle\langle i|$ are inserted, the following decomposition arises:

$$\begin{aligned} \text{Tr} [U(\beta, \tau, \alpha)] = & \\ & \sum_{m=0}^{\infty} \sum_{i_0, \dots, i_m} \int_0^\beta dt_m \int_0^{t_m} dt_{m-1} \cdots \int_0^{t_2} dt_1 \langle i_0 | V | i_1 \rangle e^{-(t_2-t_1)E_{i_1}} \langle i_1 | V | i_2 \rangle e^{-(t_3-t_2)E_{i_2}} \\ & \cdots \langle i_{L-1} | V | i_L \rangle e^{-(\tau-t_L)E_{i_L}} \langle i_L | A | i_R \rangle e^{-(t_R-\tau)E_{i_R}} \langle i_R | V | i_{R+1} \rangle e^{-(t_{R+1}-t_R)E_{i_{R+1}}} \cdots \\ & \cdots \langle i_{m-1} | V | i_m \rangle e^{(t_m-t_{m-1})E_{i_m}} \langle i_m | V | i_0 \rangle e^{(\beta+t_1-t_m)E_{i_0}}, \end{aligned} \quad (7.4)$$

where E_i is the eigenvalue of H_0 corresponding to eigenstate $|i\rangle$ and where index L points to the imaginary-time variable t_L just before τ , and the index $R = L+1$ to the imaginary-time variable t_R just after τ . Configurations are specified by an order m , a set of inserted eigenstates $|i_0\rangle, \dots, |i_m\rangle$, interaction times t_1, \dots, t_m and the worm insertion time τ . Markov processes to sample these configurations according to their weights W ,

$$\begin{aligned} W(m, i, t, \tau) = & \\ & \langle i_0 | V | i_1 \rangle e^{-(t_2-t_1)E_{i_1}} \langle i_1 | V | i_2 \rangle e^{-(t_3-t_2)E_{i_2}} \cdots \\ & \cdots \langle i_{L-1} | V | i_L \rangle e^{-(\tau-t_L)E_{i_L}} \langle i_L | A | i_R \rangle e^{-(t_R-\tau)E_{i_R}} \langle i_R | V | i_{R+1} \rangle e^{-(t_{R+1}-t_R)E_{i_{R+1}}} \cdots \\ & \cdots \langle i_{m-1} | V | i_m \rangle e^{(t_m-t_{m-1})E_{i_m}} \langle i_m | V | i_0 \rangle e^{(\beta+t_1-t_m)E_{i_0}}, \end{aligned} \quad (7.5)$$

are discussed in the following sections.

In contrast to the directed loop algorithm in the stochastic series expansion representation and the hybrid worm (Chapter 5), the worm operator remains in the description at all times. Diagonal configurations arise when A_{ij} is of the form A_{ii} .

All different kind of updates are local in the extended configuration space such that at the end of every Monte Carlo step we arrive at a configuration which contributes to the equal time Green function. Because the worm-annihilator and the worm-creator propagate simultaneously we have tremendous statistics for the equal-time Green function. However, information about dynamics is not accessible using this algorithm. The algorithm as it is outlined below can be further generalized by introducing more optimization parameters, but in practice it is already quite efficient.

In the following sections, the algorithm is introduced step by step, gradually increasing the complexity. First, we discuss a sampling when the worm operator cannot create nor annihilate interactions. Second, probabilities for inserting and annihilating interactions are introduced. Subsequently, the global acceptance factor is calculated and we end with a recipe for the Bose-Hubbard model.

7.1.1 Sampling with a constant number of interactions

Let us first consider the situation where a number of interactions are present in the configuration, with a worm that moves through and changes the interactions but that does not create or annihilate any one of them. This corresponds to the vertical moves that were discussed above, i.e. shifts of τ proportional to an exponential distribution are taken. The construction of a trial move consists of:

1. Decide with 50%/50% probability whether to move the worm to the left (lower values of τ) or to the right (higher values of τ). So the direction of the worm can change in every Monte Carlo step. Assume a jump to the right was chosen.
2. Draw the shift in imaginary time proportional to

$$P(\Delta\tau)d(\Delta\tau) = E_L e^{-E_L \Delta\tau} d(\Delta\tau), \quad (7.6)$$

where E_L is the diagonal energy to the left of the worm, including a possible energy shift $E_L - E_0$. $E_0 < \{\min_i E_i\}$ ensures non-negativity of the diagonal energies and is an optimization parameter. In practice, $\Delta\tau = -\ln(u)/E_L$ is taken, with u a uniform random deviate, $0 < u \leq 1$.

3. Evaluate $\tau' = \Delta\tau + \tau$

4. If $\tau' < t_R$ shift the worm to time τ' and proceed to step 7.
5. Otherwise, one has to move the worm through the interaction at t_R ,

$$\langle i_L | A_\alpha | i_R \rangle \langle i_R | V | i_{R+1} \rangle \rightarrow \langle i_L | V | i'_R \rangle \langle i'_R | A_{\alpha'} | i_{R+1} \rangle. \quad (7.7)$$

The state $|i_R\rangle$ is changed into a state $|i'_R\rangle$ in a way that satisfies detailed balance. This can be assured by choosing the new configuration $|i'_R\rangle$ proportional to

$$P(|i'_R\rangle) = \frac{\langle i_L | V | i'_R \rangle \langle i'_R | A_{\alpha'} | i_R \rangle}{\mathcal{N}_{L,R+1}}, \quad (7.8)$$

where \mathcal{N} is a normalization factor given by

$$\begin{aligned} \mathcal{N}_{L,R+1} &= \sum_i \langle i_L | V | i \rangle \langle i | A | A_{R+1} \rangle \\ &= \langle i_L | V A | i_{R+1} \rangle. \end{aligned} \quad (7.9)$$

According to the Metropolis-Hastings algorithm (see section 4.2.2), the acceptance factor requires a factor

$$q_R = \frac{\mathcal{N}_{L,R+1}}{\mathcal{N}_{R+1,L}}. \quad (7.10)$$

However, when $[A, V] = 0$ the acceptance factor $q_R = 1$ in all cases. This is for instance the case when the worm operator of the form (7.3) is applied to the Bose-Hubbard model.

6. After passing the interaction at t_R we can either go back to step 2 or we can avoid generating a new random number by taking the new shift as

$$\Delta\tau = \frac{E_L}{E'_L} [\Delta\tau - (t_R - \tau)], \quad (7.11)$$

where E'_L is the new diagonal energy to the left of the worm after the worm has passed the interaction at t_R . So the worm is shifted to $\tau = t_R$ and we go back to step 3.

7. When the complete time shift has been exhausted, we have to evaluate the acceptance factor q by comparing the probability to generate the (actual) step

with the probability to generate the reverse step. Because the time shifts have been generated proportional to the exponential factors in eq.(7.5), the exponential factors cancel and only the normalization coefficients of the exponential distribution remain,

$$q = \frac{E_{R,i}}{E_{L,f}}, \quad (7.12)$$

with $E_{R,i}$ the diagonal energy to the right of the worm before the update, and $E_{L,f}$ the diagonal energy to the left of the worm after the update (= before the reverse update). When the worm operator does not commute with the interaction, the above acceptance factor has to be multiplied with every q_r from the interactions at t_r the worm has passed.

8. The constructed move is accepted with probability $\min(1, q)$.

7.1.2 Sampling with a varying number of interactions

Assume the worm is at time $t = \tau$. A complete update (one step) consists of the following steps,

- at $t = \tau$ there is a chance of inserting an interaction with probability c_τ .
- Calculate the imaginary time shift.
- When the worm reaches an interaction at $t = t_l$, there is a chance of annihilating it with probability a_l and halting the worm there.

Inserting and annihilating an interaction are each other's opposite, and detailed balance should be fulfilled between them. For the annihilation procedure, there is a further complication: we have to integrate over the probabilities for all moves that would go beyond t_l .

Let us calculate the acceptance factor for inserting an (initial) interaction at $t = \tau$,

$$W(x) = \langle i_L | A_\alpha | i_R \rangle, \quad (7.13)$$

$$P[x \rightarrow y]d(\Delta\tau) = c_\tau P_{\text{ins},\tau}d(\Delta\tau), \quad (7.14)$$

$$W(y) = \langle i_L | V | i'_\tau \rangle \langle i'_\tau | A_{\alpha'} | i_R \rangle, \quad (7.15)$$

$$P[y \rightarrow x]d(\Delta\tau) = a_\tau d(\Delta\tau). \quad (7.16)$$

The new state is chosen proportional to

$$P_{\text{ins},\tau} = \frac{\langle i_L | V | i'_\tau \rangle \langle i'_\tau | A_{\alpha'} | i_R \rangle}{\mathcal{N}_\tau}, \quad (7.17)$$

where \mathcal{N}_τ is the sum of all possible numerators that can arise in the expression above. Hence, the acceptance factor is

$$q = \frac{\langle i_L | V | i'_\tau \rangle \langle i'_\tau | A_{\alpha'} | i_R \rangle}{\langle i_L | A_\alpha | i_R \rangle} \frac{a_\tau}{c_\tau P_{\text{ins},\tau}} = \frac{a_\tau \mathcal{N}_\tau}{c_\tau A_\tau} \equiv 1/q_\tau^+, \quad (7.18)$$

where A_τ denotes the matrix element of the worm operator at time $t = \tau$. This case also incorporates the case when deleting an interaction at $t = t_l$ with acceptance factor $q = q_l^+$. The other possibility is when no interaction is inserted at time $t = \tau$,

$$W(x) = \langle i_L | A_\alpha | i_R \rangle \quad (7.19)$$

$$P[x \rightarrow y]d(\Delta\tau) = (1 - c_\tau)d(\Delta\tau) \quad (7.20)$$

$$W(y) = \langle i_L | A_\alpha | i_R \rangle \quad (7.21)$$

$$P[y \rightarrow x]d(\Delta\tau) = E_R d(\Delta\tau) \quad (7.22)$$

where the last equation can be understood as the normalization factor of an imaginary time shift of infinitesimal length $d(\Delta\tau)$. The acceptance factor can be written as

$$q = \frac{E_R}{1 - c_\tau} \equiv 1/q_\tau^-. \quad (7.23)$$

All processes dealing with insertion and annihilation of interactions can be written in terms of the factors $1/q_\tau^+$ and $1/q_\tau^-$ at the beginning ($t = \tau$) of the update and in terms of the factors $q_{\tau'}^+$ and $q_{\tau'}^-$ at the end ($t = \tau'$) of the update. In more detail we have

- No interaction is inserted, no interaction is deleted: $q_{00} = q_{\tau'}^-/q_\tau^-$.
- An interaction is inserted at the beginning of the step, no interaction is deleted at the end: $q_{c0} = q_{\tau'}^-/q_\tau^+$.
- No interaction is inserted at the beginning but an interaction is deleted at the end: $q_{0a} = q_{\tau'}^+/q_\tau^-$.
- An interaction is inserted at the beginning and an interaction is deleted at the end: $q_{ca} = q_{\tau'}^+/q_\tau^+$.

7.1.3 Optimizing the sampling parameters

It is expected that the most efficient sampling method will be obtained when $q_l^+ = q_l^-$ for all l . This condition leads to

$$c_l = \frac{\mathcal{N}_l a_l}{\mathcal{N}_l a_l + E_l A_l}, \quad (7.24)$$

when the acceptance factors become

$$q_l \equiv q_l^+ = q_l^- = \frac{1}{\frac{\mathcal{N}_l}{A_l} a_l + E_l}. \quad (7.25)$$

A simple choice (but not necessarily the optimal one) is to take $a_l = 1$: an interaction is always deleted if possible. The acceptance factors q are different when moving to the left instead of moving to the right.

When $[V, A] = 0$, the final acceptance factor q depends only on a factor for the initial and final state ($t = \tau'$),

$$q = \frac{R_\tau}{R_{\tau'}}, \quad (7.26)$$

with ($R_\tau = 1/q_\tau$),

$$\begin{aligned} R_\tau &= \frac{\langle i_L | V A | i_R \rangle}{\langle i_L | A | i_R \rangle} + E_R \\ &= \frac{\langle i_L | V A | i_R \rangle}{\langle i_L | A | i_R \rangle} + \frac{i_L | A H_0 | i_R \rangle}{\langle i_L | A | i_R \rangle} \\ &= \frac{\langle i_L | A (V + H_0) | i_R \rangle}{\langle i_L | A | i_R \rangle}, \end{aligned} \quad (7.27)$$

where this expression is valid for moving to the right and where $a_l = 1$ is set. When moving to the left the indices L and R need to be interchanged. We adopt the notation R_L and R_R for moving to the left and to the right, respectively, while any information about the time is implicit in the states $|i_L\rangle$ and $|i_R\rangle$. The operator $H_0 + V$ is not the full Hamiltonian, since $H = H_0 - V$. It is tacitly assumed that the operator H_0 incorporates the energy shift E_0 . The expectation value of the factors R results in

$$\langle R \rangle = \langle H_0 + V \rangle_\beta. \quad (7.28)$$

If we choose the direction of worm propagation proportional to R_R (for moving to the right), then the global acceptance factor changes to

$$q = \frac{\bar{R}_\tau}{\bar{R}_{\tau'}}, \quad (7.29)$$

with $\bar{R} = R_L + R_R$. Accepting all moves, irrespective of the factor q , is a sampling along the distribution $\bar{R}W(\cdot)$. Finite temperature observables are then evaluated as

$$\begin{aligned} \langle Q \rangle_\beta &= \frac{\text{Tr} [e^{-\beta(H_0 - V)} Q]}{\text{Tr} [e^{-\beta(H_0 - V)}]} \\ &= \frac{\sum_{s \in \mathcal{S}} (Q_s / \bar{R}_s)}{\sum_{s \in \mathcal{S}} (1 / \bar{R}_s)}, \end{aligned} \quad (7.30)$$

and the variance is computed as [22]

$$\sigma^2(f/g) = \frac{E_{\mathcal{S}} [(f - E_{\mathcal{S}}(f/g)g)^2]}{ME_{\mathcal{S}}^2(g)}, \quad (7.31)$$

where M is the number of independent samples, $f_s = Q_s / \bar{R}_s$, $g_s = 1 / \bar{R}_s$ and $E_{\mathcal{S}}(f)$ is the Monte Carlo average for the observable f in the configuration space \mathcal{S} . Accepting all moves can thus be considered as a variance reduction attempt. In practice we found variances of the same magnitude for a fixed number of steps, but the code is much faster when all moves are accepted. The factors \bar{R}_s are well behaved because they correspond to the expectation values of a bounded Hermitian operator $H_0 + V$.

7.1.4 Application: the bosonic Hubbard model

We now provide a numerical recipe of the above algorithm for the Bose-Hubbard model. A practical choice for the worm operator is

$$\begin{aligned} A_d &= \frac{1}{\bar{N}} \sum_i n_i, \\ A_{ij} &= b_i^\dagger b_j. \end{aligned} \quad (7.32)$$

The diagonal worm is completely delocalized (not defined on a particular site), and we have introduced one optimization parameter \bar{N} , for which a very good choice

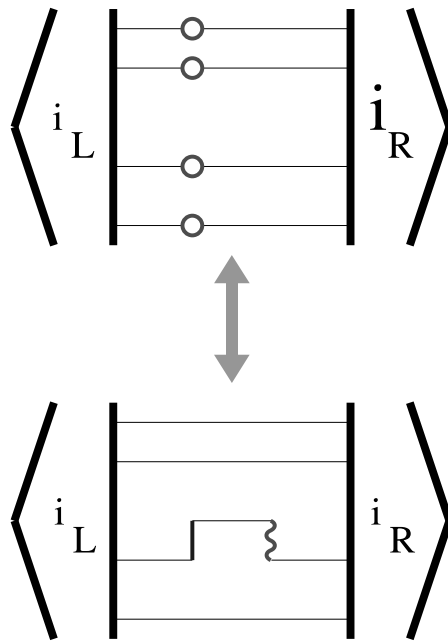


Figure 7.1 When the worm is diagonal (circles) it can insert an interaction (full line) and the new worm (curly line) is between neighboring sites. The reverse step is also possible.

is $\bar{N} = N$, the total number of bosons. The total operator A commutes with the interaction, $[V, A] = 0$. The worm weights are defined as

$$\begin{aligned} \langle i_L | A_d | i_R \rangle &= N / \bar{N}, \\ \langle i_L | A_{ij} | i_R \rangle &= \sqrt{n_i^L (n_j^L + 1)}, \end{aligned} \quad (7.33)$$

with the occupation numbers $n_i^L = \langle i_L | n_i | i_L \rangle$.

Next, the evaluation of the norms \mathcal{N}_τ requires the evaluation of all possible matrix elements of the form $\langle i_L | AV | i_R \rangle$ and $\langle i_L | VA | i_R \rangle$ and the transition probabilities between these states. All possible transitions for both diagonal and non-diagonal worms are shown in Figs. 7.1, 7.2 and 7.3, which denote intervals of infinitesimal time.

Trying out the ideas of optimally local Monte Carlo, we minimized the transition to the left upper configuration in Fig. 7.4. Only for very high values of U/t in

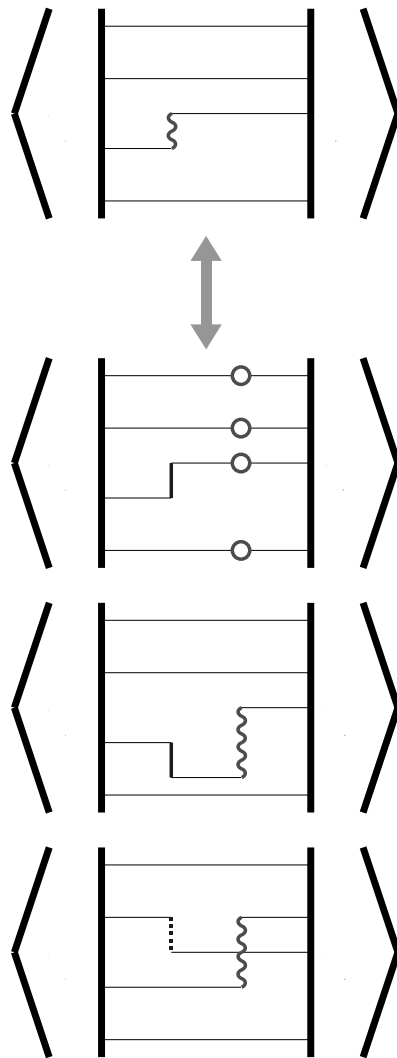


Figure 7.2 Diagrams when the current worm resides on neighboring sites and tries to insert an interaction. A full line denotes an interaction that is always possible, a dashed line is an interaction that can sometimes be inserted.

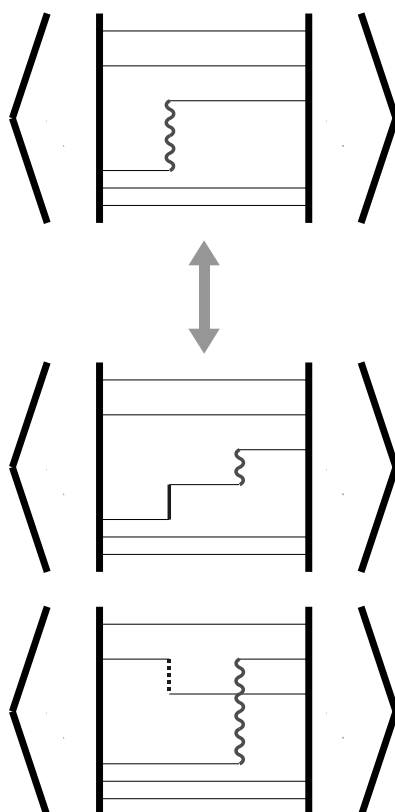


Figure 7.3 Diagrams when the current worm resides on non-neighboring sites and tries to insert an interaction.

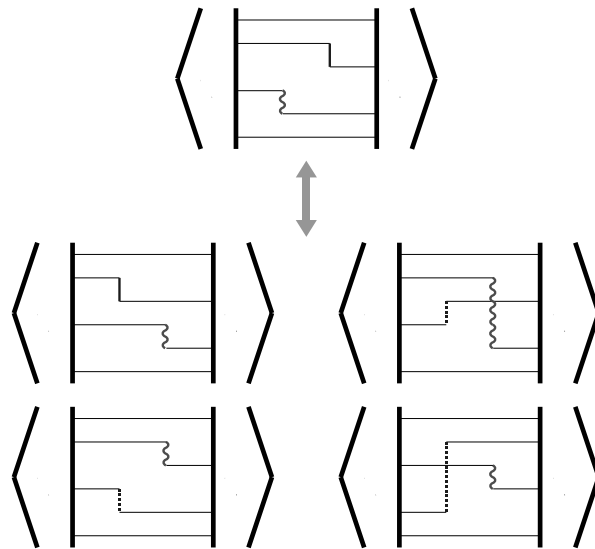


Figure 7.4 Diagrams when the worm passes an interaction that cannot be annihilated. The cases when an interaction can be annihilated are covered by Figs. 7.1, 7.2 and 7.3

the Bose-Hubbard model this was found to be an improvement in computational efficiency, but the conclusion was that it is not worth implementing it. After all, the left upper configuration in Fig. 7.4. means a change from the current configuration, and there is no reason to believe why this should be worse than the other configurations in Fig. 7.4.

Putting everything together, we arrive at the numerical recipe for every Monte Carlo step in the Bose-Hubbard Hamiltonian:

1. Assume the worm is at imaginary time position $t = \tau$, with $|i_L\rangle$ and $|i_R\rangle$ the one-particle basis states to the left and to the right of the worm. Evaluate the matrix element $A = \langle i_L | A_\alpha | i_R \rangle$.
2. Evaluate (if not yet known) for both propagation directions all possible interaction insertion matrix elements, e.g. $\langle i_L | V A_\alpha | i_R \rangle$ for jumps to the right, and for all possible sites and worm operators. The sum gives \mathcal{N}_L and \mathcal{N}_R for worm propagations to the left and to the right, respectively. Evaluate $R_L = \mathcal{N}_L / A + E_L$ and $R_R = \mathcal{N}_R / A + E_R$. Their sum gives $\bar{R} = R_L + R_R$

3. Choose the worm propagation direction proportional to R_R/\bar{R} for propagation to the right and R_L/\bar{R} for propagation to the left. Assume propagation to the right was chosen.
4. An interaction is inserted with probability $c_R = (\mathcal{N}_R/A)/R_R$. If so, an interaction proportional to the matrix elements $\langle i_L|VA_\alpha|i_R\rangle$ is chosen.
5. Draw an exponential deviate $p = -\ln(u)$ with u an uniform random number, $0 < u \leq 1$. Evaluate the imaginary time shift $\Delta\tau = p/E_R$ and the new worm time $\tau' = \tau + \Delta\tau$.
6. If this time window exceeds the time to the next interaction at $t = t_l$, we have to see if the interaction can be annihilated by the worm. If yes, annihilate the interaction with probability one and proceed to the evaluation of the acceptance factor q in step 7. Otherwise, the worm passes the interaction with probability one (since $[A, V] = 0$) but the configuration can change according to the states depicted in Fig. 7.4. Pick a new configuration according to their respective weights, and adjust the time step as

$$\tau' = t_l + (\tau' - t_l) \frac{E'_L}{E_L}, \quad (7.34)$$

where E'_L is the diagonal energy to the left of the worm after the worm has passed the interaction. Repeat this step until an interaction is annihilated, or until the time window is completely exhausted and the worm halts between two interactions.

7. The acceptance factor is $q = \bar{R}_i/\bar{R}_f$, where \bar{R}_i is the factor \bar{R} before the update and \bar{R}_f is the factor \bar{R} evaluated after the update.
8. All moves are accepted, meaning that we sample the distribution $\bar{R}W(\cdot)$ instead of the distribution $W(\cdot)$. Expectation values for diagonal observables are given by eq.(7.30) and their variances by eq.(7.30). The entry (i, j) in the histogram of the equal-time Green function can be updated after every Monte Carlo step by a factor $q_1 \cdot q_2 \cdot \dots \cdot q_{n-1} \cdot q_n$ where q_1, q_2, \dots, q_{n-1} are the acceptance factors from the previous $(n - 1)$ Monte Carlo steps, and (i, j) are the current coordinates of the worm operator.

7.2 Application: study of the Berezinskii-Kosterlitz-Thouless transition

The single feature of the standard Bose-Hubbard model we haven't scrutinized numerically so far, is the study of the quantum critical behavior near the tip of the Mott lobes. This transition is phase driven (constant density) and belongs to the Berezinskii-Kosterlitz-Thouless (BKT) [50, 51] universality class in one dimension. The canonical worm algorithm has the big advantage of keeping the density constant, in contrast to the grand-canonical approaches of Chapter 5. Studying the BKT transition is notoriously difficult because of the logarithmic finite-size corrections. Secondly, we study the quantal formulation of the problem which is known to be computationally slower than studying the equivalent $(1 + 1)$ classical rotor formulation, but may allow for the determination of the exact $U_c = (U/t)_c$ (with units $t = 1$) where the transition occurs.

Determination of the BKT transition was attempted in several previous studies. For a truncated model with a maximum of two particles per site the critical point was found at $U_c = 3.46$ with the Bethe-Ansatz [113]. In a combination of exact-diagonalization with up to $L = 12$ sites and the renormalization group, Kashurnikov *et al.* found $U_c = 3.29 \pm 0.02$ [114], and $U_c = 3.33 \pm 0.05$ in a quantum Monte Carlo study [115]. An exact diagonalization approach reported the critical point at $U_c = 3.64 \pm 0.07$ [116], and a study using 12th order strong coupling expansions located it at $U_c = 3.85 \pm 0.15$ [73]. The density matrix renormalization group (DMRG) should be the method of preference for this problem, and the most elaborate study consisted of computing the Luttinger K exponent (see Appendix A) via the long-range behavior of the one-body bosonic Green function [72]. Exactly at the BKT point, the value of K is known, $K = 2$ (see Appendix B), and this fact is used for the determination of the critical point. Unfortunately, the values of K obtained by fitting a power law to the Green function depended strongly on the fitting interval, and values for the critical point ranged from $U_c = 3.48$ to $U_c = 3.22$, with non-overlapping error bars. The BKT transition occurs also at finite temperature in the two-dimensional XY model, and has also extensively been studied in this context [117, 118].

The approach we took here is justified as follows. In Appendix B the renormalization group flow equations for the BKT transition are derived (eqs.(B.15) and (B.19)),

$$\begin{aligned}\frac{dK}{dl} &= -\delta g^2 \\ \frac{dg}{dl} &= (2 - K(l))g,\end{aligned}\tag{7.35}$$

where δ is a positive, regularization dependent constant that also depends on K . However, we can safely set $K = 2$ to this order of accuracy. The exact value of δ is not important for our purposes. The quantity $l = \ln(L - L_0)$ denotes the system size, with L_0 a characteristic length of the order of the lattice spacing. The system is coupled to the lattice via the coupling strength g . The flow equations have an integral $\Delta = (2 - K)^2 - \delta^2 g^2$ which does not depend on l . Exactly at the BKT point $(2 - K(l)) = 1/l$, or

$$f(K) \equiv \frac{1}{(2 - K)} - \ln(L) = -\ln(L_0).\tag{7.36}$$

For $K = K_{KT}$, the values of $f(K)$ will converge to a constant as a function of L , while for $K < K_{KT}$ they diverge to $-\infty$ and for $K > K_{KT}$ they diverge to $+\infty$. This approach has been used for the finite temperature BKT transition in the two-dimensional XY model in Ref. [118]. Unfortunately, the more elaborate fitting techniques of Ref. [117] cannot be applied since we do not dispose of enough statistics.

Knowing the behavior of the Luttinger K exponent in the Luttinger phase and being armed with a numerical robust procedure, we address the question of the evaluation of the K parameter. In view of the excellent statistics of the equal time Green function in the canonical worm algorithm, it seems logical to extract it from its long-range behavior. The underlying assumption is that the long range behavior of the Green function $\mathcal{G}(x)$ sets in already for very low x , which is most probably justified. In Appendix A the long range behavior at zero temperature is derived as (see eq.(A.25))

$$\mathcal{G}(x) \sim x^{-\frac{1}{2K}}.\tag{7.37}$$

Exactly at the BKT point, $\mathcal{G}(x) \sim x^{-1/4}$. However, our simulations are carried out with periodic boundary conditions meaning that the position x is better replaced by the cord function $d(x|L) = L|\sin(\pi x/L)|/\pi$ [58],

$$\mathcal{G}(x) \sim \left(\sin \frac{\pi x}{L} \right)^{-\frac{1}{2K}}. \quad (7.38)$$

Working in one dimension, we need the parameter K at zero temperature, and extracting it from a calculation at finite but small temperature can be dangerous. We take here a pragmatic viewpoint and perform all simulations at inverse temperature $\beta = L$, knowing that very close to the BKT point this is probably not good enough. The alternative is to extract zero temperature properties from e.g. a histogram of the winding number and using the fact that the speed is unrenormalizable in the Lorentz covariant Luttinger theory [31]. We found it hard to obtain sufficient statistics this way.

In Table 7.1 we show values of the Luttinger K parameter extracted from the Green function for various system sizes L at inverse temperatures $\beta = L$ and at values of U/t ranging from $U/t = 3.2$ to $U/t = 3.4$. In the second part of the table the rescaled variables $f(K)$ (see eq.(7.36)) are shown. From these numbers we conclude that in the thermodynamic limit the system is certainly in the superfluid phase at $U/t = 3.20$ and certainly in the Mott phase at $U/t = 3.33$. The transition point is located at $(U/t)_c = 3.28 \pm 0.04$. The quality of the fits can be assessed in Fig. 7.5 for a system consisting of $\beta = L = 128$.

In conclusion, we have shown that our approach is one of the most accurate numerical approaches to determine the BKT transition point. It is straightforward to obtain lower error bars on the transition point if one has slightly more computer power at hand than we do.

7.3 Canonical or grand-canonical Monte Carlo simulations?

In this section the efficiency of the directed loop algorithm in the stochastic series expansion of section 5.2 is compared to the efficiency of the worm algorithm described above. The former is in the grand-canonical ensemble, while the latter is in

Table 7.1 Extracted Luttinger K parameter (upper part) and their values $f(K)$ (lower part) according to eq.(7.36) for various system sizes L at inverse temperatures $\beta = L$ and at values ranging from $U/t = 3.2$ to $U/t = 3.4$.

	3.20	3.24	3.27	3.28	3.29	3.31	3.33	3.40
16	-0.2208	-0.2235	-0.2266	-0.2271	-0.2272	-0.2297	-0.2313	-0.2376
32	-0.2241	-0.2275	-0.2304	-0.2308	-0.2321	-0.2338	-0.2358	-0.2422
64	-0.2270	-0.2292	-0.2319	-0.2324	-0.2339	-0.2355	-0.2386	-0.2462
128	-0.2273	-0.2308	-0.2330	-0.2343	-0.2353	-0.2374	-0.2407	-0.2474
16	1.00	1.44	2.06	2.19	2.20	2.89	3.40	6.79
32	0.86	1.59	2.42	2.55	3.02	3.74	4.83	12.07
64	0.76	1.35	2.25	2.44	3.10	3.97	6.27	28.18
128	0.15	1.16	1.99	2.62	3.13	4.53	8.09	41.82

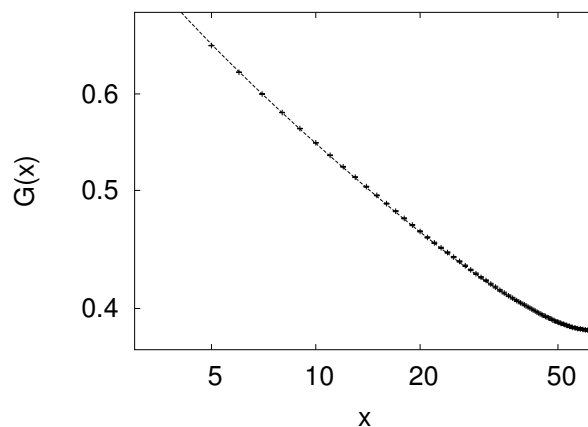


Figure 7.5 The expectation value of the Green function and its error bars are shown on log-log scale as a function of the position x from sites $x = 3$ to $x = 64$ for a system of $L = \beta = 128$ with periodic boundary conditions. The repulsion is $U/t = 3.27$. The full line is a fit with a power-law over the interval ranging from sites $x = 5$ to $x = 124$. The fitting interval has been chosen in such a way that the error on the exponent is lowest. Note that $G(1)$ corresponds to the density (exactly one) in the figure (not shown). The fitting function is of the form $f(x) = a \sin(\pi(x-1)/L)^b$, where the fitting parameters are $a = 0.38369 \pm 0.00005$ and $b = -0.232976 \pm 0.000014$. The calculation took more than eight days on a Pentium-III.

the canonical ensemble.

Simulations were done for a one-dimensional Bose-Hubbard model of $L = 32$ sites at inverse temperature $\beta = 32$ with values of the repulsion varying from $U = 1$ to $U = 10$. For the canonical worm algorithm, we took $N = 32$ particles, while for the directed loop algorithm we worked at a fixed chemical potential, $\mu = 2.0$. For sufficiently large repulsion, the system is in a Mott phase with one particle per site. The Mott phase can hence directly be used to compare the efficiency of both algorithms. The directed loop algorithm had a particle cutoff of 5 particles per site for all simulations, which is too low for the lowest values of the repulsion. The number of loops in every Monte Carlo update in the directed loop algorithm was optimized such that the integrated autocorrelation times (see eq.(4.16)) are not higher than 5. For the directed loop algorithm, a constant is added to the Hamiltonian, which increases with increasing repulsion and makes the simulation slower. The validation of the approach with fixed chemical potential in the directed loop algorithm and fixed density in the canonical worm algorithm, is that both algorithms are used in their natural way.

It is not easy to determine which observable leads to the best criterium to compare both algorithms. Since the superfluid fraction can be considered as an order parameter, it is certainly a valid candidate. Only, its value and its error bars are zero in the Mott phase in the thermodynamic limit, making a comparison impossible. Another good candidate is the kinetic energy, which can be measured in the same way for both algorithms. It suffices counting the interaction vertices that correspond to the hopping of particles. In Fig. 7.6 we see the error bars on the kinetic energy obtained for both algorithms. Both algorithms ran for 40 times 300 seconds for every data point on the same Pentium III processor. The accuracy on the error bars is about 10 percent. The directed loop algorithm is clearly more efficient in the superfluid phase (although particle number cut-off is too low) compared with the Mott phase. The canonical worm algorithm remains as efficient throughout all values of the repulsion. In the Mott phase the canonical worm algorithm is found to be more efficient than the directed loop algorithm, while in the superfluid the opposite seems true. This is in line with the intuitive feeling that the worm algorithm

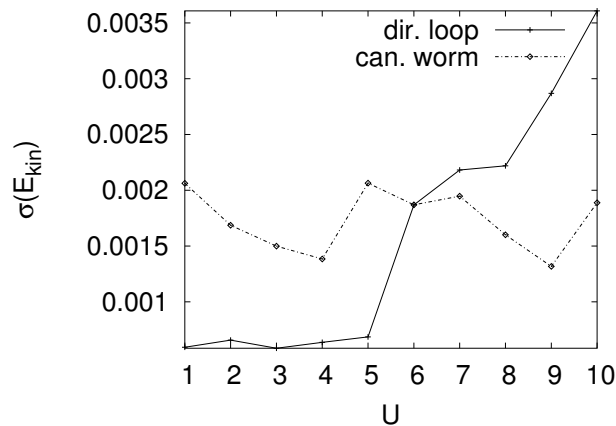


Figure 7.6 Error bars on the kinetic energy for a Bose-Hubbard chain of $L = 32$ sites at inverse temperature of $\beta = 32$ for various repulsion strengths. Results are shown for the directed loop algorithm in the grand-canonical ensemble and canonical worm algorithm (see text). The simulations took 40 times 300 seconds on a Pentium III for every data point.

should be the method of preference when there are large diagonal matrix elements. However, care has to be taken with such a statement: other observables like the compressibility always have error bars that are of the order of magnitude lower in the canonical worm algorithm than in the directed loop algorithm. Second, the integrated autocorrelation times (see eq.(4.16)) for the kinetic energy in the canonical worm algorithm were found to be surprisingly high (factor of 2) compared to the ones of the superfluid fraction. This is probably a consequence of the fact that during one Monte Carlo step the number of interactions can change only by 0 or ± 1 , and it makes sense to extend the canonical worm algorithm such that the worm does not always stop after annihilating an interaction. Thirdly, the data structures used in both algorithms are different.

Recall that the canonical worm algorithm had an optimization parameter: a constant shift E_0 needed to make the diagonal energies positive. In the derivation of the algorithm a global constant was used for this. Another choice is to vary the constant in every Monte Carlo step and using $E_0 = \min[E_L, E_R]$ where E_L and E_R are the energies to the left and to the right of the current worm, respectively. This choice can result in infinite time jumps, meaning that the next interaction is reached

with probability one. We found the second approach superior to the first one for most observables (except for the kinetic energy) if the lattice is sufficiently large. This approach was used in the simulations.

In conclusion, it is hard to compare the efficiency of the directed loop algorithm in the stochastic series expansion and the canonical worm algorithm since the comparison is observable dependent and also depends on the different implementation (data structure). When working in the canonical ensemble, the use of the canonical worm algorithm is preferred.

Chapter 8

Mixtures of bosons and fermions in a one-dimensional optical lattice

In this chapter we consider a mixture of bosons and fully spin-polarized (spinless) fermions in a one-dimensional optical lattice. Theoretically, this system has been studied using Lanczos diagonalization for small lattice sizes [119], using the Gutzwiller ansatz [120] and using bosonization techniques [121, 122]. Compared to the pure bosonic case, novel phenomena are predicted, such as the Peierls instability towards a charge density wave [123] and the pairing between bosons and fermions [121, 122]. In a charge density wave the density of the particles is modulated. In this work a first step is made to derive a quantum Monte Carlo method able to describe the several phases. Experimentally it is not fully clear how these phases can be realized and how they can be observed. Defining clear experimental signals will be the challenge for future research, which falls outside the scope of this thesis.

We start with the derivation of the Bose-Fermi Hubbard Hamiltonian in one dimension. Then we discuss some general properties and limiting cases of this model and introduce the canonical boson-fermion worm. We end with numerical simulations. It will become clear from the results that this part of the thesis (Chapter 8) should be regarded as an outlook and as a direction indicator for future research. However, as this is a problem where a two-particle worm is essential, we thought it sufficiently interesting to discuss it here. Possible extensions to boson-boson mixtures in higher dimensions and to one-dimensional systems with bosons

and fermions with spin show the importance of the first steps presented in this chapter.

8.1 The Bose-Fermi Hubbard Hamiltonian

The Hamiltonian for a Bose-Fermi mixture loaded into a one-dimensional optical lattice and confined by an additional, slowly varying external harmonic trapping potential is [120]

$$H = T_B + T_F + V_{T,B} + V_{0,B} + V_{T,F} + V_{0,F} + W_{BB} + W_{BF}, \quad (8.1)$$

where

$$T_B = - \int dx \Psi_B^\dagger(x) \frac{\hbar^2}{2m_B} \frac{d^2}{dx^2} \Psi_B(x), \quad (8.2)$$

$$T_F = - \int dx \Psi_F^\dagger(x) \frac{\hbar^2}{2m_F} \frac{d^2}{dx^2} \Psi_F(x), \quad (8.3)$$

are the boson and fermion kinetic energies while the boson-boson and the fermion-boson contact interaction energies are

$$W_{BB} = \frac{1}{2} \frac{2\hbar^2 a_{BB}}{m_B a_{\perp,B}^2} \int \Psi_B^\dagger(x) \Psi_B^\dagger(x) \Psi_B(x) \Psi_B(x), \quad (8.4)$$

$$W_{BF} = \frac{1}{2} \frac{2\hbar^2 a_{BF}}{m_R a_{\perp,B} a_{\perp,F}} \int \Psi_B^\dagger(x) \Psi_F^\dagger(x) \Psi_F(x) \Psi_B(x). \quad (8.5)$$

The boson-boson and the fermion-boson s -wave scattering lengths a_{BB} and a_{BF} , the boson mass m_B , the fermion mass m_F and the reduced mass m_R parameterize the interaction strength. The transverse harmonic oscillator length $a_{\perp,B/F}$ results from the Gaussian integration over the tight transverse directions, where we have assumed that the magnetic field is not close to a confinement induced resonance (see eq.(2.2)) [36]. We consider pure magnetic trapping for the bosons and the fermions such that the fermions are fully spin-polarized and their s -wave interaction can be neglected. The axial confinement is approximated by a harmonic potential,

$$V_{T,B}(x) = m_B \frac{1}{2} \omega_B^2 x^2, \quad (8.6)$$

$$V_{T,F}(x) = m_F \frac{1}{2} \omega_F^2 x^2. \quad (8.7)$$

If the bosons and the fermions are trapped in the same magnetic state, then $\omega_F/\omega_B = (m_B/m_F)^{1/2}$ so that the two potentials coincide, $V_B(x) = V_F(x)$. Their harmonic oscillator lengths differ however. The optical lattice potentials along the axial direction is produced by a far off-resonant laser for both species,

$$V_{0,B}(x) = V_{0,F}(x) = V_0 \sin^2(\pi x/a). \quad (8.8)$$

For sufficiently strong optical potentials the lowest band analysis of section 2.1 readily generalizes to the present situation. Expanding the field operators in the Wannier functions leads to the Bose-Fermi Hubbard Hamiltonian,

$$\begin{aligned} H &= -t_B \sum_{\langle i,j \rangle} b_i^\dagger b_j - t_F \sum_{\langle i,j \rangle} f_i^\dagger f_j \\ &+ \frac{U_{BB}}{2} \sum_i n_i(n_i - 1) + U_{BF} \sum_i n_i m_i \\ &+ \sum_i \epsilon_i^B n_i + \sum_i \epsilon_i^F m_i, \end{aligned} \quad (8.9)$$

where the boson annihilation operator is denoted by b_i , the boson density by n_i , the fermion annihilation operator by f_i and the fermion density by m_i . The first line in the Bose-Fermi Hubbard model describes nearest neighbor hopping of bosons and fermions with amplitudes t_B and t_F , respectively. The boson-boson on-site repulsion has strength U_{BB} , while the boson-fermion on-site interaction can be repulsive or attractive, depending on the sign of U_{BF} . The third line describes the harmonic trapping with strength ϵ_i^B for the bosons and strength ϵ_i^F for the fermions, analogously as for the Bose-Hubbard Hamiltonian. The discussion given here is limited to the homogeneous system, $\epsilon_i^B = \epsilon_i^F = 0$.

8.2 General properties of the Bose-Fermi Hubbard Hamiltonian

In this section we focus on the special case $t_B = t_F$, which can be a good approximation when the masses of the bosonic and fermionic atoms are approximately equal. An interesting symmetry of the Bose-Fermi Hubbard Hamiltonian is the particle-hole symmetry for the fermions,

$$f_j \rightarrow (-1)^j f_j^\dagger, \quad (8.10)$$

which leaves the fermionic kinetic energy invariant, but changes $U_{BF} \rightarrow -U_{BF}$. This means that instead of studying the attractive model with fermions, we can equally well study the repulsive model with fermionic holes. For the experiment, this makes all the difference: sympathetic cooling of the fermions with the bosons is much easier for attractive boson-fermion interactions because the larger bosonic cloud overlaps with the fermionic cloud. This symmetry is no longer valid in a trapped system.

Secondly, we focus on the limits of the Bose-Hubbard model. When there is no coupling between the bosons and the fermions, the Hamiltonian factorizes into the Bose-Hubbard model and a system of non-interacting fermions. We can expect that for very low U_{BF} and low $U_{BB} > U_{BF}$ the system consists of a bosonic and a fermionic Luttinger liquid.

In the limit of very high U_{BB} the bosons behave as effective hard-core bosons (Tonks bosons). The Hamiltonian then reduces to the one-dimensional Fermi Hubbard model,

$$H = -t \sum_{j,\sigma} c_{j,\sigma}^\dagger c_{j,\sigma} + \frac{U_F}{2} \sum_j n_{j,\uparrow} n_{j,\downarrow} \quad (8.11)$$

where $c_{j,\sigma}$ annihilates a fermion of spin σ on site j . The Tonks bosons can then be thought of as spin-up particles, and the fermions of spin-down particles (or vice-versa). At half filling the Fermi Hubbard model has a total symmetry group $SU(2) \times SU(2) = SO(4)$ as a consequence of the hidden charge symmetry resulting from the symmetry eq.(8.10). For large U_F (i.e. large U_{BF}) the system is equivalent to a Heisenberg chain with an exchange constant $J \sim 4t^2/U_F$. For repulsive and large U_F the system is dominated by antiferromagnetic long range order (spin density wave). For attractive and large U_F , pairs of opposite spins form a singlet on a site. Away from half filling, the Fermi-Hubbard model is metallic for large $U_F > 0$. In the Bose-Fermi Hubbard model we thus expect to see a Mott phase at half filling for high U_{BB} and reasonably high U_{BF} .

The other limit, $U_{BF} \gg U_{BB} > 0$ induces a phase separation between the bosons and the fermions. As we want to study correlations between bosons and

fermions in the first place, this phase is not extensively discussed here.

The case of a small kinetic coupling $t \ll U$ and $(U_{BB} - U_{BF}) \ll U_{BB}$ has low energy states where on each site the bosonic and fermionic density are equal, $n_i = (1 - m_i)$. These are separated from other states by a large gap $\approx U$. We arrive at the description in terms of boson-hole pairs $b_j^\dagger f_j$. In second-order perturbation theory in t/U , the dynamics of pairs is given by the effective Hamiltonian [120]

$$H_{\text{eff}} = -t_{\text{eff}} \sum_{\langle i,j \rangle} f_i^\dagger \bar{f}_j + K_{\text{eff}} \sum_{\langle i,j \rangle} \bar{m}_i \bar{m}_j. \quad (8.12)$$

The effective parameters t_{eff} and K_{eff} are the strengths of nearest neighbor hopping of composite fermions and nearest neighbor composite fermion-fermion repulsion/attraction. The coefficients K_{eff} and t_{eff} can be written in terms of t, U_{BB} , and U_{BF} where t_{eff} acquires a different form depending on the parameter regime. The effective model is equivalent to that of spinless interacting fermions, whose physics are well known. For sufficiently strong and positive K_{eff} the composite fermions form a density wave (one composite fermion every two sites), while for sufficiently strong and negative K_{eff} the composite fermions form a superconducting phase. Translated to the Bose-Fermi Hubbard model, we expect for sufficiently large $U_{BB} \approx U_{BF}$ a phase characterized by boson-hole pairs. Note that this phase corresponds to the super-counter-fluid of Ref. [44, 45] for $U_{BF} > 0$ (when the superfluid bosons and the holes propagate in opposite directions in phase) or to the paired superfluid vacuum for negative U_{BF} when $U_{BB} \neq |U_{BF}|$ (when the superfluid bosons and the holes propagate in the same direction in phase). This pairing between bosons and fermions is one of the most interesting features of mixtures of ultracold atoms in optical lattices.

8.3 Canonical boson-fermion worm

The Bose-Fermi Hubbard model can be studied exactly by quantum Monte Carlo algorithms in one dimension when the fermions are treated as hard-core bosons (since we cannot impose anti-periodic boundary conditions). As we have seen in Chapter 6, the fermionic Green function differs from the hard-core bosonic one, but

quantities like the energy and the density remain equal. All results in this chapter are for hard-core bosons, the phase factors for the fermions have not been taken into account. The algorithm we propose is in the canonical ensemble and is a direct generalization of the canonical worm algorithm of section 7.1.

First, we have to discuss the extension of the canonical worm algorithm to the case of hard-core bosons, for which the worm operator does no longer commute with an interaction. At first this looks like a serious problem, but inspecting the algorithm, we notice that when the worm passes an interaction nothing changes, since the norm of all possible new configurations is equal to the norm of the reverse step. There is a difference however at the beginning and at the end of a worm update, when the norms for moving to the left and moving the right are no longer equal to each other. This is no problem either since the acceptance factors do not change. The conclusion is that the canonical worm algorithm can be applied to hard-core bosons.

For the Bose-Fermi Hubbard model we propose a two-particle worm of the form

$$W = \sum_{\alpha,\beta} W_{\alpha,\beta} = b_i^\dagger b_j f_i^\dagger f_{j'}, \quad (8.13)$$

where the b_i are the soft-core boson annihilation operators and the f_i the hard-core boson (fermion) annihilation operators. The worm allows for changing both the bosonic and the fermionic configuration, meaning that a boson can efficiently tunnel in a fermionic configuration at all times (and vice versa). Such a worm offers the possibility to compute the equal time soft-core boson Green function, the equal time hard-core boson (fermion) Green function and the Green function of the composite fermionic particles (boson+fermion). For repulsive U_{BF} we compute the Green function for the composite boson+fermionic hole instead. When the worm is diagonal in both the bosonic and fermionic operators, we can compute observables like the bosonic and fermionic density, the boson density-density correlation function, the boson-fermion density-density correlation, etc. The bosonic superfluid fraction and the fermionic charge stiffness can be obtained by measuring their respective winding numbers W_B and W_F , while the super-counter-fluid and the paired su-

perfluid vacuum fractions can be obtained by measuring $W_B \pm W_F$.

The resulting algorithm is now a straightforward extension of the canonical worm algorithm of section 7.1. There are only a lot more possibilities to consider. We opted again for an approach consisting of accepting all Monte Carlo steps, irrespective of the acceptance factor.

The two-particle worm allows the computation of the order parameter of all phases mentioned in the previous section. The worm is very efficient in the Luttinger liquid phase. In case of a Mott phase at half filling for both species with $U_{BB} \gg U_{BF} \gg 0$, the worm locates the fermions alternating with the bosons with little effort. The algorithm does not converge to one specific ground state with broken translational symmetry, but oscillates between all equivalent ground states. This property holds for any parameter regime where one (or both) of the species develop density wave order. There are, however, serious efficiency problems for the phase where the bosons and fermions are separated. The algorithm quickly converges to one ground state, but then tries to oscillate to another ground state (that can be obtained from the first ground state by translation). The worm is inefficient for this process, as the worm does not allow half of the bosons (fermions) to tunnel at the same time between the fermionic (bosonic) configuration.

To end this section, we make some remarks: First, we experienced serious problems when trying to simulate the Bose-Fermi Hubbard model in the grand-canonical ensemble using the directed loop algorithm in the stochastic series expansion framework, where the updates for the bosons and for the fermions are performed one after the other. Finetuning two chemical potentials proved to be too difficult, and for most parameter regimes one of the species disappeared from the system. With fixed density however, the phase diagram of the Fermi-Bose Hubbard model is much richer. A grand-canonical approach is thus less favourable (although it is possible), and this forced us to think about canonical algorithms. Second, we report the failure of the simulation of the Bose-Fermi Hubbard model with the canonical worm algorithm of section 7.1, where an update consists of two steps (similar to what we have tried with the directed loop algorithm): First, the

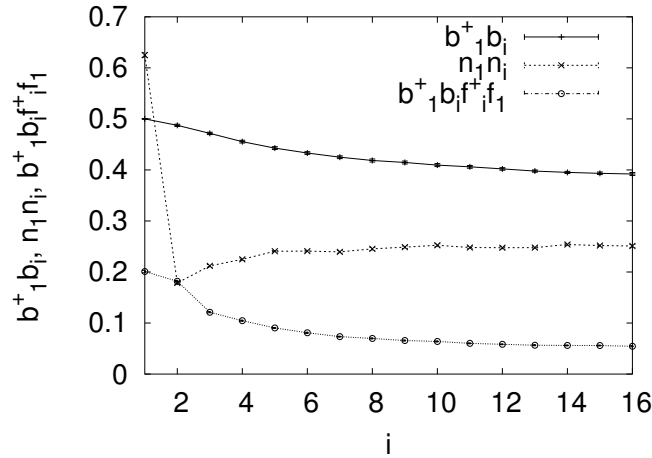


Figure 8.1 Bosonic Green function ($b_1^\dagger b_i$), bosonic density-density correlation function ($n_1 n_i$) and composite boson-hole Green function ($b_1^\dagger b_i f_i^\dagger f_1$) for a mixture with $U_{BB} = U_{BF} = 1$ at half filling for each of the species. This behavior occurs in the phase characterized by two interacting Luttinger liquids (Luttinger liquid-Luttinger liquid phase).

bosonic configuration is changed with a fixed fermionic configuration until a new diagonal configuration is obtained. In the second step, a fermionic worm changes only the fermionic configuration. With these updates, the tunneling for a boson in a fixed fermionic configuration was found to be too inefficient (and vice versa).

8.4 Monte Carlo simulations

8.4.1 Half filling

First we consider the case where we have half filling for both the bosons and the fermions. All simulations were done for a lattice with $L = 32$ sites with periodic boundary conditions at an inverse temperature $\beta = 32$, and with equal hopping amplitudes, $t_B = t_F = 1$. We distinguish three cases:

- The Luttinger liquid-Luttinger liquid phase, where the bosonic and fermionic Green function behave as a power-law at large distances. This is shown in Fig. 8.1.
- A phase where the bosonic Green function decays exponentially and the composite boson-hole Green function with a power law. The bosonic density-

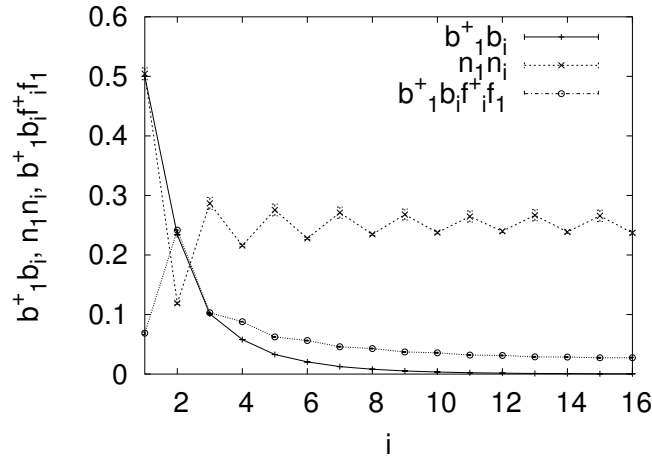


Figure 8.2 Bosonic Green function ($b_1^\dagger b_i$), bosonic density-density correlation function ($n_1 n_i$) and composite boson-hole Green function ($b_1^\dagger b_i f_i^\dagger f_1$) for a mixture with $U_{BB} = 40$, $U_{BF} = 5$. This behavior corresponds to the Mott phase.

density correlation function also decays with a power-law and shows clear oscillations, as can be seen in Fig. 8.2. This phase corresponds to the Mott-phase. This is also reflected in the compressibility of the system, and in the bosonic structure factor which is the Fourier transform of the boson density-density correlation function and has a peak at momentum $k = \pi$.

- The region where phase separation occurs. As already explained, we experienced convergence problems in this limit. However, this is only the case for the diagonal observables. We expect exponential decay of the bosonic Green function and of the composite boson-hole Green function, as is illustrated in Fig. 8.3. Additional evidence is provided by the (bosonic) structure factor that shows a peak at momentum $k = \pi/L$ and a minimum at $k = \pi$. The transition to the phase separated phase is a first order transition.

8.4.2 Doped system

For the doped system with $n_B = (1 - m_F) \neq 0.5$, the description in terms of the composite particles of eq.(8.12) applies. This parameter-regime can equally as well be described by the bosonization theories of Ref. [121] and Ref. [122], where in

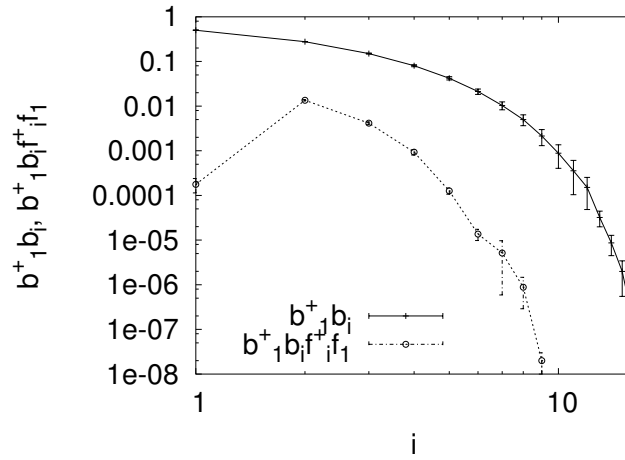


Figure 8.3 Bosonic Green function ($b_1^\dagger b_i$) and composite boson-hole Green function ($b_1^\dagger b_i f_i^\dagger f_1$) for a mixture with $U_{BB} = 5, U_{BF} = 45$. This behavior corresponds to phase separation.

the latter a polaron picture was suggested. For large U_{BB} and U_{BF} the composite particles develop density wave order. When looking at the bosonic structure factor, which is the Fourier transform of the boson density-density correlation factor, one would expect a peak at momentum $k = \pi$. In Fig. 8.4 this peak was indeed observed for a mixture with system parameter $U_{BB} = 30, U_{BF} = 35$. The simulation was done on a lattice of 16 sites at inverse temperature $\beta = 32$. The bosonic Green function decays exponentially, while the Green function of the composite boson-hole particles has power-law asymptotic behavior. The computation of the density-density correlation function is complicated due to its oscillatory nature. At lower values of $U_{BF} = 5$, the maximum of the bosonic structure factor is not found at exactly $k = \pi$, while the mentioned correlation functions behave quantitatively similarly as for $U_{BF} = 35$. These are only the first results, and it remains to be seen how the ideas presented here can be further quantified.

8.4.3 Bosons at integer filling

When the bosonic density exactly matches the number of sites and when the fermions are at half filling, the bosons can form a Mott phase while the fermions behave as a normal Luttinger liquid, as in Fig. 8.5. This regime roughly occurs for sufficiently

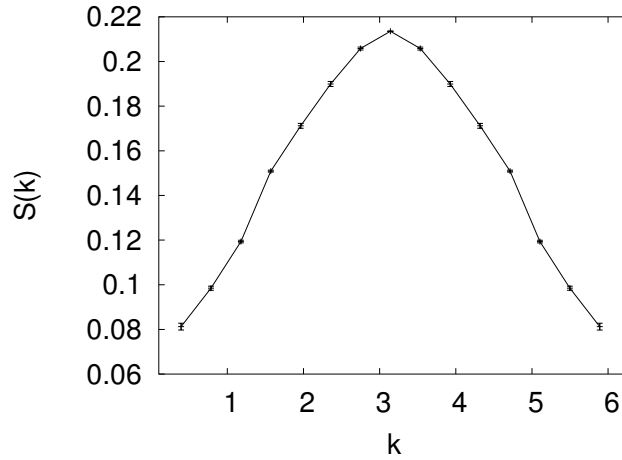


Figure 8.4 Bosonic structure factor $S(k)$ as a function of momentum k for a mixture consisting of 16 sites and at inverse temperature $\beta = 32$. The system parameters are $U_{BB} = 30$ and $U_{BF} = 35$, while there are 9 bosons and 7 fermions in the system.

large $U_{BF} < U_{BB}$. From the exact diagonalizations of Ref. [119], we know that the fermions can form density wave order, or become phase separated with the holes. Unfortunately, the worm algorithm exhibits huge autocorrelation times for these parameter regimes, and for the moment it is not possible to study these phases for large lattice sizes. This shows that a further refinement of the algorithm is necessary.

8.5 Outlook

In this chapter we have made a first step towards the study of mixtures of bosons and fermions in one-dimensional optical lattices. The presented worm algorithm allows the computation of the composite boson-fermion correlation function, and it can distinguish between localized phases and phases characterized by (composite particle) Luttinger behavior. However, when the interaction strength between the bosons and the fermions becomes of the same order as the interaction strength between the bosons, the integrated autocorrelation times increase substantially, and at present it is not clear how this can be overcome. At present, it is already possible to obtain clear signals for every phase using parallel computer facilities, and the

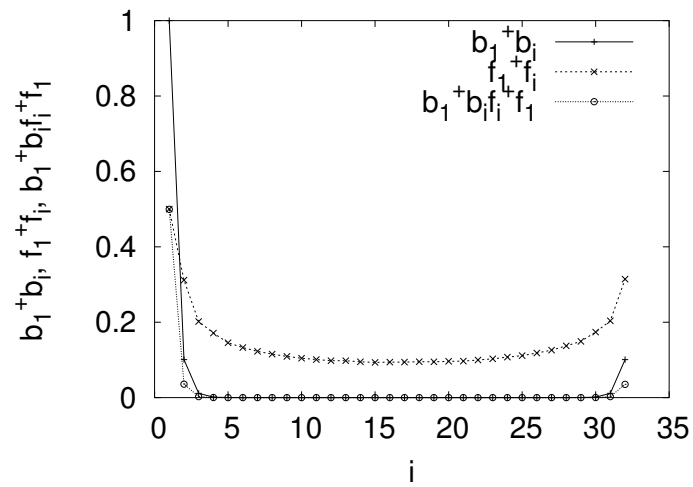


Figure 8.5 Bosonic correlation function ($b_1^\dagger b_i$), fermionic (hard-core bosonic) correlation function ($f_1^\dagger f_i$) and composite boson-fermionic hole correlation function ($b_1^\dagger b_i f_i^\dagger f_1$) for a system consisting of 32 bosons and 16 fermions on a lattice of $L = 32$ sites at an inverse temperature $\beta = 32$. The system parameters are $U_{BB} = 40$ and $U_{BF} = 15$.

determination of a phase diagram should be feasible on a supercomputer.

Chapter 9

Conclusions

This thesis provides a numerical approach to our understanding of the physics of ultracold bosonic atoms in optical lattices. When a Bose-Einstein condensate is transferred to an optical lattice, the unique controllability over the underlying periodic structure and the interactions between the atoms offer the possibility to simulate a whole range of fundamental phenomena that are impossible to study in real materials.

Ultracold bosonic atoms loaded in an optical lattice are described by the discrete Bose-Hubbard model, and can undergo a quantum phase transition from a weakly interacting superfluid phase to a strongly interacting Mott insulating phase. This transition was first observed by M. Greiner *et al.* [6].

Optical lattices have also been used to investigate aspects of one-dimensional quantum gases. When the repulsion between one-dimensional bosonic atoms increases, they undergo a process called fermionization. Atoms tend to separate from one another, mimicking the Pauli principle for fermions. In the limit of infinite repulsion, bosonic atoms behave like (free) fermions in many respects and are said to form a Tonks-Girardeau gas [11]. The Tonks-Girardeau gas has experimentally first been demonstrated in Ref. [13].

The central aim of this thesis is the numerical modeling and simulation of these two experiments. Furthermore, the validity of the Bose-Hubbard model was discussed, and we studied its quantum critical properties. The numerical methods we

used are the real-space renormalization group and quantum Monte Carlo methods based on a local sampling of the Green function in the world line representation. In the more technical parts of the thesis, we propose new quantum Monte Carlo algorithms and discuss their numerical efficiency along the lines of 'locally optimal Monte Carlo'. These developments allow us to study more complex systems, such as one-dimensional mixtures of bosons and fermions in an optical lattice. Now follows a short summary of every chapter.

After a short overview of recent developments in the fields of optical lattices and quantum Monte Carlo methods based on world line representations and a lattice-description in Chapter 1, the Bose-Hubbard model was shown to describe the physics of ultracold bosonic atoms in an optical lattice. In the Bose-Hubbard model, the Bogoliubov approximation is a good approximation to the superfluid phase, while perturbation theory provided a picture of gapped quasiparticles and quasiholes as the lowest energy excitations in the Mott phase. The transition between the superfluid and the Mott phase can either be driven by density fluctuations or by phase fluctuations, each of them belonging to a different universality class. In one dimension the concept of a Luttinger liquid applies. All these field theories are discussed in Chapter 2.

The experiment on the superfluid-Mott phase transition by Greiner *et al.* [6] was studied using a numerical renormalization group + mean field approach. We were able to obtain variationally accurate results at a low computational cost. In the experiment the cross-over (rather than the phase transition) is signaled by a change in the width and intensity of the central interference peak. The results of Chapter 3 have been published as *L. Pollet, S. Rombouts, K. Heyde, and J. Dukelsky, Phys. Rev. A* **69**, 043601 (2004).

Monte Carlo methods are introduced in Chapter 4. We spent some time on the efficiency of Markov Chain Monte Carlo, and introduced the notion of 'locally optimal Monte Carlo'. Rather than offering the 'optimal' Monte Carlo strategy, it provides a framework on how the efficiency of existing algorithms might be improved. The new results in this chapter appeared in *L. Pollet, S. M. A. Rombouts, K.*

Van Houcke, and K. Heyde, Phys. Rev. E **70**, 056705 (2004).

In Chapter 5, the directed loop algorithm in the stochastic series expansion and the worm algorithm are discussed. It is shown that the former is a limiting case of the latter. The notion of 'locally optimal Monte Carlo' was applied to spin-systems and the Bose-Hubbard model using the directed loop algorithm and shown to yield roughly optimal solutions. Subsequently, a new formulation of the worm algorithm was given. The formulation incorporates the ideas of locally optimal Monte Carlo from the onset. We have called this algorithm the hybrid worm. Parts of this chapter appeared in *L. Pollet, S. M. A. Rombouts, K. Van Houcke, and K. Heyde, Phys. Rev. E* **70**, 056705 (2004).

When one-dimensional bosons become strongly interacting, they behave like fermions in many respects. In the limit of infinite repulsion, the bosons are effectively fermionized and are said to form a Tonks-Girardeau gas. This limit has been realized experimentally and the experiment has been described by B. Paredes *et al.* [13]. In Chapter 6, we checked whether the atoms are better described by soft-core or by hard-core bosons. We found that in all cases the soft-core description is more accurate. The strongly interacting regime indeed sets in for values of the repulsion for which the fermionization theory yields good agreement with the experiment. However, the discrepancy between the momentum profiles for hard-core and soft-core bosons was still found to be large for these values of the repulsion. The results of Chapter 6 have been published as *L. Pollet, S. M. A. Rombouts, and P. J. H. Denteneer, Phys. Rev. Lett.* **93**, 210401 (2004).

In Chapter 7, a worm algorithm for the Bose-Hubbard model in the canonical ensemble is described in detail. It offers the possibility to study the Berezinskii-Kosterlitz-Thouless quantum phase transition and determine the exact transition point, since the amount of statistics is significantly improved at the same computational cost using the approach presented here.

Chapter 8, which is the final chapter in this thesis, is intended as an outlook and as a direction indicator for future research. The technical aspects for a Monte Carlo

study of mixtures of bosons and fermions in a one-dimensional optical lattice are discussed. The canonical worm algorithm of Chapter 7 is readily generalized to a two-particle worm algorithm. The simulations allowed to study phases that are not presented in the Bose-Hubbard model, although current calculations are still in an initial stage of the research project. Most spectacularly, the atoms can form a charge density wave where the density of the particles becomes modulated, and there are also phases possible where the bosons and the fermions form a composite fermionic particle.

Appendix A

Bosonizing one-dimensional bosons in a nutshell

In Appendix A, we study the long-range low-energy properties of the one-dimensional Bose-Hubbard model using the Luttinger Liquid concept. We show how the Mott phase transition can be studied using these concepts. As a model calculation, the asymptotic behavior of the single-particle Green function is explicitly calculated at zero temperature. The derivation is based on the presentation in Ref. [56].

A.1 Hamiltonian

The one-dimensional Bose-Hubbard Hamiltonian in the canonical ensemble

$$H = -t \sum_{\langle i,j \rangle} b_i^\dagger b_j + \frac{U}{2} \sum_i n_i(n_i - 1), \quad (\text{A.1})$$

with the notation explained in Chapter 2 can be studied in the long-range low-energy limit using Haldane's bosonization technique (harmonic fluid approach) [54, 55]. The boson field creation and density operators are represented as [56, 57]

$$\psi^\dagger(x) = n_0^{1/2} \sum_p e^{i2p(\pi n_0 x - \phi(x))} e^{-i\theta(x)}, \quad (\text{A.2})$$

$$n(x) = n_0 - \frac{1}{\pi} \nabla \phi(x) + n_0 \sum_{p \neq 0} e^{i2p(\pi n_0 x - \phi(x))}, \quad (\text{A.3})$$

where x is a continuous coordinate arising when the lattice spacing is approaching zero, $a \rightarrow 0$, and where n_0 is the mean density. The fields $\phi(x)$ and $\frac{1}{\pi} \nabla(\theta(x))$ are

canonically conjugated, $[\phi(x), \frac{1}{\pi} \nabla(\theta(x))] = i\delta(x - x')$.

In the continuum, the kinetic term becomes to lowest order

$$\begin{aligned} H_1 &= \int dx \frac{(\nabla\psi)^\dagger (\nabla\psi)}{2m} \\ &= \int dx \frac{n_0}{2m} (\nabla e^{i\theta})(\nabla e^{-i\theta}) = \int dx \frac{n_0}{2m} (\nabla\theta)^2. \end{aligned} \quad (\text{A.4})$$

For the interaction term we have

$$H_2 = \frac{U'}{2\pi^2} \int dx (\nabla\phi)^2, \quad (\text{A.5})$$

where the higher harmonics in eq.(A.3) have renormalized the coefficient. The total Hamiltonian has two contributions, and hence we can expect that the most general Hamiltonian describing the physical properties is of the form

$$H = \frac{1}{2\pi} \int dx \left[uK (\nabla\theta(x))^2 + \frac{u}{K} (\nabla\phi(x))^2 \right]. \quad (\text{A.6})$$

This is the so-called Luttinger Hamiltonian. It describes a free field theory and the Luttinger parameters u and K are treated phenomenologically. Using numerics it is possible to relate the Luttinger parameters u and K to the parameters of the underlying lattice model, in this case the parameters t and U of the Bose-Hubbard model. The Luttinger Hamiltonian describes the long-range low-energy properties of any non-interacting one-dimensional system.

The presence of a lattice has some pronounced effects however. A lattice potential can be written as

$$V_L(x) = \sum_m g_m \cos(Qmx), \quad (\text{A.7})$$

with $Q = 2\pi/a$. The lattice Hamiltonian $H_L = \int dx V_L(x)n(x)$ is non-oscillating for $mQ = 2\pi n_0 p$ or for $m/a = n_0 p$, where p denotes the commensurability ($p = 1$: one boson per site, $p = 2$: two bosons per site etc.). Hence, For $p = 1$ the lattice Hamiltonian is

$$H_L = g \int dx \cos(2\phi(x)). \quad (\text{A.8})$$

A.2 Correlation function

The Luttinger liquid concept is very powerful and allows to study the long-range behavior of correlation functions analytically. Here, we only compute the behavior of the bosonic one-body Green function and take the limit to zero temperature. First, we rewrite the Luttinger Hamiltonian as a free relativistic massless scalar theory.

The action corresponding to the Luttinger Hamiltonian is

$$-S = \int_0^\beta d\tau \int dx \left[i \frac{1}{\pi} \nabla \theta(x, \tau) \partial_\tau \phi(x, \tau) - \frac{1}{2\pi} \left(uK (\nabla \theta)^2 + \frac{u}{K} (\nabla \phi)^2 \right) \right]. \quad (\text{A.9})$$

By going to Fourier space and adopting the notations $r = (x, u\tau)$ and $q = (k, \omega_n/u)$,

$$\phi(r) = \phi(x, \tau) = \frac{1}{\sqrt{\beta L}} \sum_q e^{iq \cdot r} \phi(q) = \frac{1}{\sqrt{\beta L}} \sum_{k, \omega_n} e^{i(kx - \omega_n \tau)} \phi(k, \omega_n), \quad (\text{A.10})$$

and analogously for $\theta(x, \tau)$. So, we obtain for the action

$$-S = \frac{1}{\beta L} \sum_q \left[-i \frac{k\omega_n}{\pi} \phi(q) \theta(-q) - \frac{uK}{2\pi} k^2 \theta(q) \theta(-q) - \frac{u}{2\pi K} k^2 \phi(q) \phi(-q) \right]. \quad (\text{A.11})$$

Completing the square for the θ field gives

$$\begin{aligned} -S &= \frac{1}{\beta L} \sum_q -\frac{uK}{2\pi} k^2 \left[\theta(q) + \frac{i\omega_n}{uKk} \phi(q) \right] \left[\theta(-q) + \frac{i\omega_n}{uKk} \phi(-q) \right] \\ &\quad - \frac{u}{2\pi K} k^2 \phi(q) \phi(-q) - \frac{\omega_n^2}{2\pi uK} \phi(q) \phi(-q). \end{aligned} \quad (\text{A.12})$$

The integration over the field $\theta(q) + \frac{i\omega_n}{uKk} \phi(q)$ is Gaussian, yielding the action

$$S_\phi = \frac{1}{\beta L} \sum_{k, \omega_n} \frac{1}{2\pi K} \left(\frac{-\omega_n^2}{u} + uk^2 \right) \phi(k, \omega_n) \phi^*(k, \omega_n) \quad (\text{A.13})$$

$$= \frac{1}{2\pi K} \int dx \int_0^\beta d\tau \left[\frac{1}{u} (\partial_\tau \phi(x, \tau))^2 + u (\partial_x \phi(x, \tau))^2 \right]. \quad (\text{A.14})$$

Equivalently, since the Hamiltonian is invariant under $\phi(x, \tau) \rightarrow \theta(x, \tau)$ and $K \rightarrow 1/K$,

$$S_\theta = \frac{1}{\beta L} \sum_{k, \omega_n} \frac{K}{2\pi} \left(\frac{-\omega_n^2}{u} + uk^2 \right) \theta(k, \omega_n) \theta^*(k, \omega_n) \quad (\text{A.15})$$

$$= \frac{K}{2\pi} \int dx \int_0^\beta d\tau \left[\frac{1}{u} (\partial_\tau \theta(x, \tau))^2 + u (\partial_x \theta(x, \tau))^2 \right]. \quad (\text{A.16})$$

For the single particle bosonic Green function the lowest order harmonics require evaluation of

$$\begin{aligned}\psi^\dagger(r)\psi(0) &\sim \langle e^{i(\theta(r)-\theta(0))} \rangle \\ &\sim e^{-\frac{1}{2}\langle(\theta(r)-\theta(0))^2\rangle},\end{aligned}\quad (\text{A.17})$$

where the second line is a consequence of the quadratic nature of the Luttinger Hamiltonian. The computation is easiest in Fourier space,

$$\langle(\theta(r)-\theta(0))^2\rangle = \frac{1}{\beta L} \sum_{q_1, q_2} \langle \theta(q_1)\theta(q_2) \rangle (e^{iq_1 \cdot r} - 1) (e^{iq_2 \cdot r} - 1) \quad (\text{A.18})$$

The expectation value $\langle \theta(q_1)\theta(q_2) \rangle$ can readily be obtained using Gaussian integrals,

$$\frac{1}{Z_\theta} \int \mathcal{D}\theta(x, \tau) e^{-S_\theta} \theta(q_1)\theta(q_2) = \frac{\pi\beta L}{K(\frac{1}{u}\omega_n^2 + uk^2)} \delta_{-q_1, q_2} \quad (\text{A.19})$$

Inserting eq.(A.19) in eq.(A.18) yields

$$\langle(\theta(r)-\theta(0))^2\rangle = \frac{1}{\beta L} \sum_q \frac{2\pi}{K(\frac{\omega_n^2}{u} + uk^2)} (1 - \cos(qr)) \quad (\text{A.20})$$

$$= \frac{1}{K} F_1(r) \quad (\text{A.21})$$

The summation is divergent for large momenta, meaning that we have to introduce a finite bandwidth α . When $\beta = \infty$ and $L = \infty$ the integral $F_1(r)$ can easily be evaluated,

$$F_1(r) = \int \frac{d\omega}{2\pi} \int \frac{dk}{2\pi} e^{-\alpha k} (1 - \cos(kx - \omega\tau)) \frac{2\pi u}{\omega^2 + u^2 k^2} \quad (\text{A.22})$$

$$= \int \frac{dk}{k} \left(1 - e^{-u|\tau|k} \cos(kx)\right) e^{-\alpha k} \quad (\text{A.23})$$

$$= \frac{1}{2} \ln \left[\frac{x^2 + (u|\tau| + \alpha)^2}{\alpha^2} \right]. \quad (\text{A.24})$$

Consequently, the long range behavior of the Green function $\mathcal{G}(r)$ is

$$\begin{aligned}\mathcal{G}(r) &\sim e^{-\frac{1}{2K}F_1(r)} \\ \mathcal{G}(x) &\sim x^{-\frac{1}{2K}},\end{aligned}\quad (\text{A.25})$$

where $\mathcal{G}(x)$ denotes the equal time Green function. The Green function decays as a power-law with an exponent that depends on the interaction strength. This is a highly non-perturbative result.

Appendix B

Renormalization Group Approach to the superfluid-Mott transition

B.1 Commensurate case

Appendix B deals with the functional renormalization group of the Berezinskii-Kosterlitz-Thouless transition (BKT) [50, 51] in the Wilson-Kadanoff sense [64]. The renormalization flow equations are derived. The calculation is based on the $(1 + 1)$ dimensional renormalization of the sine-Gordon Hamiltonian, which is a standard topic in many field-theory textbooks [56].

The Kadanoff-Wilson renormalization approach consists schematically of the following steps [124]:

- We have a theory with momentum cut-off Λ to start with.
- The cut-off is varied from Λ to $\Lambda' = \Lambda/s$, $s > 1$. The field is decomposed into fast and slow modes (=only momenta smaller than Λ' in magnitude).
- The integration over the fast modes leads to an effective theory with the new momentum cut-off Λ' .
- By the scale change $k \rightarrow sk$, the cutoff is brought back to $\Lambda' \rightarrow \Lambda$. The original theory is recovered but with renormalized coupling strengths. Varying the cutoff infinitesimally slowly, $s = 1 + \epsilon$, yields the flow equations (differential equations) for the coupling constants.

This renormalization procedure is applied to the action (see eq.(A.8) and eq.(A.14))

$$S = \frac{1}{2\pi K} \int dx d\tau \left[\frac{1}{u} (\partial_\tau \phi)^2 + u (\partial_x \phi)^2 \right] + \frac{g}{(2\pi\alpha)^2} \int dx d\tau \cos(2\phi(x, \tau)). \quad (\text{B.1})$$

The first two terms describe a Gaussian field theory. The parameter α is the cutoff parameter of the theory. The factor 2 in front of the field under the cosine matters: the action (B.1) is the continuum-limit of the Bose-Hubbard model with commensurate $n = 1$ filling. Higher commensurate filling factors lead to other prefactors ($2n$).

The field $\phi(x, \tau)$ can be expanded in Fourier modes (see eq.(A.10)),

$$\phi(x, \tau) = \frac{1}{\sqrt{\beta L}} \sum_{k, \omega_n} e^{i(kx - \omega_n \tau)} \phi(k, \omega_n). \quad (\text{B.2})$$

For simplicity we take $\beta = \infty$. We will also adopt the shorthand notation $r = (x, u\tau)$ and $q = (k, \omega_n/u)$, as in Appendix A.

The initial sharp momentum cutoff Λ is varied between Λ and Λ' and the field ϕ is decomposed into fast and slow Fourier modes,

$$\phi(r) = \phi^>(r) + \phi^<(r), \quad (\text{B.3})$$

where

$$\begin{aligned} \phi^>(r) &= \frac{1}{\beta L} \sum_{\Lambda' < \|q\| < \Lambda} e^{iqr} \phi(q) \\ \phi^<(r) &= \frac{1}{\beta L} \sum_{\|q\| < \Lambda'} e^{iqr} \phi(q). \end{aligned} \quad (\text{B.4})$$

The quadratic part of the action

$$S_0 = \frac{1}{2\pi K} \frac{1}{\beta L} \sum_q [\omega_n^2/u + uk^2] \phi^*(q) \phi(q) \quad (\text{B.5})$$

can immediately be written as

$$S_0 = S_0^< + S_0^>. \quad (\text{B.6})$$

The Luttinger Hamiltonian corresponds to a fixed point, and when the cosine is expanded to second order in the field, the coupling g is marginal. The partition

function can be expanded in powers of the cosine, which gives up to second order (Z_0 is the partition function for $g = 0$)

$$\begin{aligned} \frac{Z}{Z_0} &= \frac{1}{Z_0} \int \mathcal{D}\phi e^{-S_0^>-S_0^<} \left[1 - \frac{g}{(2\pi\alpha)^2} \int d^2r \cos(2(\phi^>(r) + \phi^<(r))) \right. \\ &\quad \left. + \frac{g^2}{2(2\pi\alpha)^4} \int d^2r_1 \int d^2r_2 \cos(2(\phi^>(r_1) + \phi^<(r_1))) \cos(2(\phi^>(r_2) + \phi^<(r_2))) \right]. \end{aligned} \quad (\text{B.7})$$

The average over the fast modes can be done using $\langle e^{i\phi(r)} \rangle = e^{-\frac{1}{2}\langle\phi^2(r)\rangle}$ for quadratic theories, yielding

$$\begin{aligned} \frac{Z}{Z_0} &= \frac{1}{Z_0^<} \int \mathcal{D}\phi e^{-S_0^<} \left[1 - \frac{g}{(2\pi\alpha)^2} \int d^2r \cos(2\phi^<(r)) e^{-2\langle(\phi^>(r))^2\rangle} \right. \\ &\quad \left. + \frac{g^2}{4(2\pi\alpha)^4} \sum_{\epsilon=\pm} \int d^2r_1 \int d^2r_2 \cos(2(\phi^<(r_1) + \epsilon\phi^<(r_2))) e^{-2\langle(\phi^<(r_1) + \epsilon\phi^<(r_2))^2\rangle} \right]. \end{aligned} \quad (\text{B.8})$$

An effective action is found by reexponentiating this expression. This is equivalent to the standard cumulant expansion, $\langle e^\Omega \rangle = e^{[\langle\Omega\rangle + \frac{1}{2}\langle(\Omega^2) - \langle\Omega\rangle^2]}$. To second order we have

$$\begin{aligned} \frac{Z}{Z_0} &= \frac{1}{Z_0^<} \int \mathcal{D}\phi e^{-S_0^< - \frac{g}{(2\pi\alpha)^2} \int d^2r \cos(2\phi^<(r)) e^{-2\langle(\phi^>(r))^2\rangle}} \\ &\quad e^{\frac{g^2}{4(2\pi\alpha)^4} \int d^2r_1 \int d^2r_2 \left[\sum_{\epsilon=\pm} \cos(2(\phi^<(r_1) + \epsilon\phi^<(r_2))) e^{-2\langle(\phi^<(r_1) + \epsilon\phi^<(r_2))^2\rangle} \right]} \\ &\quad e^{-\frac{g^2}{2(2\pi\alpha)^4} \int d^2r_1 \int d^2r_2 \left[\cos(2\phi^<(r_1)) e^{-2\langle(\phi^>(r_1))^2\rangle} \cos(2\phi^<(r_2)) e^{-2\langle(\phi^>(r_2))^2\rangle} \right]}. \end{aligned} \quad (\text{B.9})$$

The last term cancels the square of the term linear in g , i.e. it cancels the disconnected parts for which the points r_1 and r_2 are very far away from each other. The first term is like the original cosine but for the slow fields only, with the smaller cutoff Λ' . The original action with the cutoff Λ is found back by the transformation

$$dk = \frac{\Lambda'}{\Lambda} dk' \quad (\text{B.10})$$

and an analogous one for ω . Space and time coordinates rescale as

$$dx = \frac{\Lambda}{\Lambda'} dx', \quad d\tau = \frac{\Lambda}{\Lambda'} d\tau'. \quad (\text{B.11})$$

The new coupling constant is

$$g(\Lambda') = \left(\frac{\Lambda}{\Lambda'} \right)^2 g(\Lambda) e^{-2\langle(\phi^>(r))^2\rangle} = \left(\frac{\Lambda}{\Lambda'} \right)^2 g(\Lambda) e^{-\frac{2}{\beta L} \sum_{\Lambda' < \|q\| < \Lambda} \frac{\pi K u}{\omega_n^2 + u^2 k^2}}, \quad (\text{B.12})$$

where the average over the fast $\phi^>(r)$ field is done by going to Fourier space and applying the formulae for Gaussian integrals. For $\beta \rightarrow \infty$ and $L \rightarrow \infty$ the sum can be converted into an integral,

$$\begin{aligned} g(\Lambda') &= \left(\frac{\Lambda}{\Lambda'}\right)^2 g(\Lambda) e^{-\int_{\Lambda' < \|q\| < \Lambda} dq \frac{K}{q}} \\ &= \left(\frac{\Lambda}{\Lambda'}\right)^2 g(\Lambda) e^{-2K \ln(\Lambda/\Lambda')} \end{aligned} \quad (\text{B.13})$$

The cutoff is usually parametrized as $\Lambda(l) = \Lambda_0 e^{-l}$ where Λ_0 is the bare cutoff. With the infinitesimal change $\Lambda' = \Lambda_0 e^{-l-dl}$ one gets

$$g(l+dl) = g(l) e^{(2-K)dl}. \quad (\text{B.14})$$

Hence, the renormalization equation is

$$\frac{dg(l)}{dl} = g(l)(2 - K(l)). \quad (\text{B.15})$$

This flow equation cannot be the end of story, because when $|K - 2| \sim g$ this equation acquires contributions which are quadratic. This equation could also have been derived in another way [9]. Because of relativistic invariance of the Luttinger Hamiltonian, the quantum time scales linearly with position. For $g = 0$ we have scale invariance, and by the powerlaw decay of the Green function, eq.(A.25), the line $g = 0$ is a line of critical points along which the exponents vary continuously as a function of the Luttinger parameter K . A direct generalization of the reasoning behind eq.(A.25) to the higher commensurate case (an integer number p bosons per site) shows that

$$e^{ip\theta(x)} e^{-ip'\theta(0)} \sim \delta_{p,p'} x^{-\frac{1}{2K}}. \quad (\text{B.16})$$

The scaling dimension of the operator is thus

$$\dim \left[e^{ip\theta} \right] = \frac{p^2}{4K}. \quad (\text{B.17})$$

Applying this scaling dimension for $p = 2$ gives $\dim[g] = (2 - K)$ along the $g = 0$ line and yields eq.(B.15) immediately.

To quadratic order, the main contribution comes from the region where r_1 and r_2 are close to each other. Depending on the sign of ϵ there are two contributions. For

$\epsilon = 1$ the term $\cos(2(\phi^<(r_1) + \phi^<(r_2)))$ is essentially a term $\cos(4\phi^<)$ that is less relevant than the original cosine and can be dropped close to the point where the cosine becomes relevant ($K \sim 2$). The terms with $\epsilon = -1$ generate gradients on $\phi^<$ and lead to a renormalization of K . The relevant term is

$$\frac{g^2}{4(2\pi\alpha)^4} \int d^2r_1 \int d^2r_2 \cos(2(\phi^<(r_1) - \phi^<(r_2))) \left[e^{-2\langle(\phi^>(r_1) - \phi^>(r_2))^2\rangle} - e^{-4\langle(\phi^>)^2\rangle} \right] \quad (\text{B.18})$$

which leads to the renormalization equation

$$\frac{dK}{dl} = -\delta g^2, \quad (\text{B.19})$$

where δ is a positive, regularization dependent constant also depending on K , but we can set $K = 2$ to this order. The renormalization equations are perturbative in g but exact in K .

B.2 Commensurate-Incommensurate transition. Doping

The natural extension of the renormalization group approach would be to treat a term like

$$H_{IC} = g \int dx \cos(2\phi(x) - \delta x) \quad (\text{B.20})$$

where the doping δ is the mismatch in density with the commensurate case. For very small doping, the system essentially behaves as a commensurate system, while for high doping the cosine is highly oscillating and irrelevant. Hence, δ^{-1} is the lengthscale at which the system realizes that it is not commensurate. Eq.(B.20) breaks the equivalence between time and space, and the speed u renormalizes as well. The renormalization group equations for K , u , g and δ can be derived in the same way as in the previous section. Unfortunately, the renormalization group approach does not allow to extract the critical properties of the commensurate-incommensurate transition. Close to the transition ($\delta \rightarrow 0$) the flow goes to the strong coupling regime before the renormalization of the cosine is stopped, and one has to resort to other methods.

However, without being rigorous, it is not difficult to understand the physics of

this transition in $d = 1$ exploiting the absence of statistics in one dimension. Let us focus on the commensurate-incommensurate (generic) transition in the neighborhood of the $n = 1$ Mott lobe. It means a chemical potential μ is needed. Measuring the density with respect to the $n = 1$ filling, we have that the charge $Q = \langle \psi^\dagger \psi \rangle = 0$ for $\mu < 0$ and $Q > 0$ for $\mu = 0$. The ground state at the quantum critical point $\mu = 0$ is the empty vacuum with no particles. Any interactions that appear are due to particles created by external fields (ladder diagrams only). The bosonic Green function is hence the free field one (at temperature $T = 0$ and chemical potential $\mu \leq 0$),

$$\mathcal{G}^0(k, \omega) = \frac{1}{\omega - k^2/(2m) + \mu + i\eta}, \quad (\text{B.21})$$

and the density can readily be obtained

$$\langle \psi^\dagger \psi \rangle = \int \frac{dk}{2\pi} \frac{d\omega}{2\pi} (i\mathcal{G}^0(k, \omega)) = \begin{cases} \frac{1}{\pi}(2m\mu)^{1/2}, & \mu > 0 \\ 0, & \mu < 0 \end{cases}. \quad (\text{B.22})$$

Exactly at the transition the doping is zero and by comparing the decay of the free bosonic Green function to the generic one in a Luttinger Liquid (see eq.(A.25)), we find that $K = 1$ is the critical Luttinger exponent at the transition, exactly one half of its value at the Berezinskii-Kosterlitz-Thouless point. Values of K lower than one cannot be obtained in the Bose-Hubbard Hamiltonian with on-site repulsion only.

Bijlage C

Nederlandstalige Samenvatting

Dit proefschrift bestaat uit twee grote pijlers, die in het eerste hoofdstuk kort behandeld worden.

Ten eerste is er de studie van ultrakoude atomen in optische roosters. Sinds de experimentele realisatie van Bose-Einstein condensatie (BEC) in ultrakoude bosonische alkali-gassen, heeft dit vakgebied, dat zich op de scheidingslijn van de atomaire en vaste stof fysica bevindt, een enorme bloei gekend. Een condensaat van ultrakoude atomen is inherent een zwak interagerend systeem, beschreven door de Gross-Pitaevskii theorie en de Bogoliubov benadering. Door een laser aan te wenden op de condensaatwolk kan echter overgegaan worden op een sterk interagerend systeem. Naargelang de intensiteit van de laser zullen de atomen meer gelokaliseerd zijn in de minima van de optische potentiaal. Op dat moment gaat de fase-coherentie tussen de bosonische atomen verloren en veranderen de waargenomen interferentie patronen sterk: de intensiteit van de nulde orde piek wordt veel minder en de breedte van de piek neemt gevoelig toe, zoals te zien is in Fig. 1.2. Door de intensiteit van de laser terug te verminderen, wordt de positie van de atomen minder gelokaliseerd en kan fasecoherentie terug hersteld worden. Op het interferentiepatroon zal de centrale piek opnieuw helderder en smaller zijn. De zopas beschreven fase-overgang tussen de superfluide en de Mott fase wordt beschreven door het discrete Bose-Hubbard model. Experimenteel werd ze het eerst verwezenlijkt door M. Greiner *et. al* [6] en betekende dé doorbraak voor de wereld van ultrakoude gassen in optische roosters. De mogelijkheden van deze techniek liggen voor de hand: vele discrete modellen uit de vaste stof fysica kun-

nen op een uiterst controleerbare en zuivere manier bestudeerd worden. Een van de grote uitdagingen betreft het observeren van Cooper-paren. Een interessant limietgeval van ultrakoude bosonen is de Tonks-Girardeau limiet: ultrakoude bosonen in één dimensie gedragen zich in veel opzichten als fermionen wanneer de repulsie tussen de bosonen oneindig sterk wordt. In een optisch rooster kan dit als volgt begrepen worden: wanneer de repulsie tussen de bosonen sterker wordt, zal het systeem streven om maximaal één deeltje per site te plaatsen. Bosonen met maximaal één deeltje per site worden hard-core bosonen genoemd, in tegenstelling tot (soft-core) bosonen waarvoor geen bovengrens voor de bezetting geldt. Hard-core bosonen volgen dus dezelfde statistiek als fermionen, en de verwachtingswaarde van grootheden zoals de energie en de dichtheid is identiek wanneer men de fermionische dan wel de hard-core bosonische grondtoestandsgolffunctie gebruikt. Voor een grootheid als de ééndeeltjes-Greense functie, gedragen de fermionen zich niet langer identiek aan de hard-core bosonen, maar moeten de fasefactoren ten gevolge van de antisymmetrie van de fermionische golffunctie terug in rekening gebracht worden. De Tonks-Girardeau limiet werd experimenteel het eerst in een optisch rooster waargenomen en beschreven door B. Paredes *et al.* [13]. Beide experimenten worden kort toegelicht in het eerste hoofdstuk, en de verklaring ervoor vormt een van de belangrijkste drijfveren voor dit proefschrift.

De tweede pijler van dit proefschrift betreft de ontwikkeling en implementatie van nieuwe numerieke algoritmes en behoort tot de computationele fysica. Daar de analytische theorieën in het Bose-Hubbard model perturbatief van aard zijn, dient men numerieke methodes aan te wenden voor de exacte berekening van correlatiefuncties. A fortiori geldt dit wanneer men de kritische exponenten van de kwantum fase overgang wil bestuderen. Daarnaast kende de ontwikkeling van (discrete) kwantum Monte Carlo algoritmes die zich baseren op wereldlijnrepresentaties de laatste jaren een enorme toename. Met de komst van het 'loop'-algoritme en van het 'worm'-algoritme en later van het 'directed-loop' algoritme werd een ongekeerde efficiëntie voor kwantum Monte Carlo algoritmes bereikt, wat toeliet om bijzonder grote systemen bij extreem lage temperatuur te bestuderen. Recentelijk werd aangetoond dat deze algoritmes in feite dezelfde idee vertolken. Dit proefschrift bouwt verder op deze ideeën en heeft een bijdrage geleverd tot het

verder uitbreiden, catalogeren en efficiënter maken van deze algoritmes.

In het tweede hoofdstuk wordt eerst uitgelegd hoe men een bosonisch condensaat in een optisch rooster aan de hand van het discrete Bose-Hubbard model beschrijft, door enkel de laagstliggende energieband te beschouwen en de veldoperatoren te ontwikkelen in de Wannier basis. Vervolgens worden de algemene eigenschappen van het Bose-Hubbard model besproken met aandacht voor de bestaande analytische benaderingen. De gemiddeld-veld Gutzwiller ansatz wordt besproken, alsook de (equivalente) ontkoppelingsbenadering. De Mott fase wordt besproken in storingstheorie, en de superfluide fase wordt behandeld door middel van de Bogoliubov benadering. Speciale aandacht is er voor de twee verschillende types van kwantum fase overgangen, namelijk de overgang die gedreven wordt door fasefluctuaties en deze die gedreven wordt door dichtheidsfluctuaties. Er wordt uitgelegd hoe de fysica in één dimensie essentieel verschillend is van de fysica in drie dimensies. Sterk interagerende ééndimensionale bosonen kunnen als fermionen beschouwd worden aan de hand van de fermionizatietheorie. In het tweede hoofdstuk ligt de nadruk op de afleiding van het analytische raamwerk die verderop in het proefschrift gebruikt worden.

Het derde hoofdstuk legt zich specifiek toe op de studie van de fase-overgang tussen de superfluide fase en de Mott fase zoals die experimenteel is waargenomen door M. Greiner *et al.* [6]. Er wordt een gemiddeld veld + numerieke renormalisatiegroep methode voorgesteld, die een verbetering inhoudt op vroegere numerieke renormalisatiegroepmethodes. De methode laat toe om grote roosters bij temperatuur $T = 0$ te bestuderen op een manier die weinig computertijd vraagt, maar toch veel verder gaat dan een gemiddeld-veld benadering. De kostprijs is dat de methode niet exact is, en dat het moeilijk is om de nauwkeurigheid systematisch op te drijven. Dit wordt uitgebreid behandeld in hoofdstuk 3. Tenslotte worden berekeningen getoond bij parameters die de experimentele situatie heel goed benaderen. De belangrijkste conclusies zijn dat de overgang tussen de superfluide en Mott fase experimenteel inderdaad bereikt werd, maar dat het verdwijnen van de eerste orde diffractie-piek gebeurt wanneer de repulsie veel sterker is dan de kritische repulsie die nodig is voor de (experimenteel geleidelijke) overgang tussen de superfluide en Mott fase. Met andere woorden, de eerste orde diffractie-piek

verdwijnt pas wanneer het systeem zich diep in de Mott fase bevindt, in overeenstemming met de resultaten van Ref. [78]. In tegenstelling tot de bevindingen van Ref. [78], vermoeden wij dat het optreden van 'satelliet'-pieken een gevolg is van de eindige uitgebreidheid van het systeem, en geen verband houdt met de overgang naar de Mott fase. De centrale piek in het diffractiepatroon echter, wordt minder intens en breder. Onze bevindingen werden intussen bevestigd door andere auteurs [75, 79, 80].

Daar het moeilijk bleek om de numerieke renormalisatiegroep van hoofdstuk 3 verder te verbeteren of uit te breiden naar andere systemen, werd uitgekeken naar kwantum Monte Carlo algoritmes, die het voordeel hebben statistisch exact te zijn. Het vierde hoofdstuk is technisch van aard, en overloopt kort de wiskunde die achter Markov keten Monte Carlo zit. Dit laat toe om een discussie over de efficiëntie van Markov keten Monte Carlo te voeren, en de belangrijkste bijdrage van dit hoofdstuk is het opstellen van de transitie-matrix die ons garandeert wat optimale sampling van een distributie is onder alle omstandigheden. Dit resultaat was gekend in de wiskundige literatuur, maar onbekend in de fysica-literatuur. Hoewel dit wiskundig resultaat op zich in de praktijk niet bruikbaar is omwille van de te grote dimensies, hebben we vastgesteld dat de efficiëntie van sommige bestaande algoritmes gevoelig verbeterd werd wanneer de transitie-matrix lokaal aangewend wordt. In dit verband werd de term 'lokaal optimale' Monte Carlo ingevoerd. Dit werd geïllustreerd voor het Potts model met zogenaamde Glauber dynamica. Dit hoofdstuk biedt een algemeen kader over hoe een algoritme efficiënter kan gemaakt worden, in tegenstelling tot de ad-hoc regels die tot nog toe bestonden.

Het vijfde hoofdstuk geeft de afleiding van het 'directe loop'-algoritme in de 'stochastic series expansion', met de nadruk op het feit dat dit algoritme een limietgeval is van het 'worm' algoritme. De rol van de terugbots-processen werd in verband gebracht met de commutator van de worm-operator en de interactieterm. Vervolgens werden de ideeën van 'lokaal optimale' Monte Carlo hier succesvol toegepast. Het 'directe loop'-algoritme wordt in de praktijk vooral toegepast op spin-systemen. Hier werd enkel een demonstratieberekening getoond, ter beves-

tig van Haldane's voorspellingen dat ééndimensionale Heisenbergketens met halfvallige spin kritisch zijn, terwijl die met heeltallige spin een gap vertonen [101, 102]. Vervolgens wordt een nieuwe variant van het 'worm'-algoritme gegeven. Uitgaande van vele simulaties hebben we de numerieke voordelen van het 'directe loop' algoritme enerzijds en van het 'worm' algoritme anderzijds proberen in te schatten en te combineren in een nieuwe, lokale formulering van het 'worm' algoritme. Deze nieuwe formulering noemen we het 'hybride worm' algoritme. Dit hoofdstuk eindigt met een bespreking over de efficiëntie van het 'directe loop' en van dit 'worm' algoritme.

Het zesde hoofdstuk gaat over het bereiken van de Tonks-Girardeau limiet voor ééndimensionale bosonen in een optisch rooster. Met behulp van het 'directe loop'-algoritme wordt nagegaan of het experiment beschreven door Paredes *et al.* [13] beter beschreven wordt door soft-core dan wel door hard-core bosonen. Door eveneens de Wannier states in rekening te brengen, werd een heel nauwkeurige overeenkomst tussen het experiment en onze simulaties gevonden voor soft-core bosonen. De verschillen tussen hard-core en soft-core bosonen worden geleidelijk kleiner naarmate de repulsie toeneemt. Het regime van sterk-interagerende bosonen wordt vrij snel bereikt. Verder bleek een Mott domein de geleidelijke overgang naar de Tonks-Girardeau limiet niet te versnellen, en bespraken we de rol van de temperatuur.

In hoofdstuk 7 legt zich toe op een verdere ontwikkeling van worm algoritmes tot het canonisch ensemble. Het algoritme wordt afgeleid en er wordt een numeriek procédé voor het Bose-Hubbard model voorgesteld. Voor het Bose-Hubbard model laat dit algoritme toe de superfluide - Mott faseovergang te bestuderen die optreedt bij vaste dichtheid en wordt gedreven door fasefluctuaties. In één dimensie is deze overgang van het Berezinskii-Kosterlitz-Thouless type. Steunend op de renormalisatiegroep-vergelijkingen wordt een methode voorgesteld ter bepaling van het kritische punt van de kwantumfaseovergang. De precieze bepaling van dit punt is een moeilijk onderwerp ten gevolge van de logaritmische correcties die een Berezinskii-Kosterlitz-Thouless overgang inhoudt, en waarden in de literatuur variëren sterk, zelfs binnen één methode. De voorgestelde aanpak is eenduidig en

robuust en de nauwkeurigheid is controleerbaar. Ondanks de beperkte statistiek waarover we beschikken, kregen we foutenvlaggen die kunnen wedijveren met de meest nauwkeurige methodes tot nog toe. Met het gebruik van parallele computers kunnen de foutenvlaggen ongetwijfeld nog gevoelig verbeterd worden.

In het achtste hoofdstuk gaan we over naar een 'ééndimensionaal systeem dat bestaat uit zowel bosonen als fermionen in een optisch rooster. De fysica is nu veel rijker. Zo is het mogelijk dat het systeem beschreven wordt door twee Luttinger vloeistoffen, of dat er fase-separatie tussen de bosonen en de fermionen optreedt, of er kunnen fases bestaan waar de bosonen en de fermionen alternerend optreden. Het meest spectaculair is het feit dat de bosonen en de fermionen kunnen paren tot composiet-fermionen. Voor de studie van al deze fenomenen werd een nieuw tweedeeltjes-worm algoritme ontwikkeld in het canonisch ensemble. Het asymptotisch gedrag van verschillende correlatiefuncties liet toe deze verschillende fases te identificeren, al is het duidelijk dat het huidig algoritme voor een aantal parameterregimes een verlies aan efficiëntie vertoont, en dat dit onderzoeksproject nog maar in een beginstadium verkeert.

In de Appendices wordt 'bosonizatie' besproken en wordt deze techniek toegepast om de laag-energetische lange-xafstandseigenschappen van het ééndimensionale Bose-Hubbard model te bestuderen. Verder worden de renormalisatiegroepvergelijkingen voor het 'sine-Gordon' model opgesteld. Dit zijn beide tekstboekonderwerpen.

De conclusie van dit proefschrift is dat de experimenten over de superfluide-Mott faseovergang [6] en het bereiken van de Tonks-Girardeau limiet door ultrakoude bosonische atomen in een ééndimensionaal optisch rooster [13] goed begrepen zijn. Numeriek-technisch werden enkele bijdragen geleverd aan kwantum Monte Carlo algoritmes die zich baseren op een wereldlijn-representatie op een discreet rooster, en werden enkele nieuwe algoritmes voorgesteld.

Bibliography

- [1] M. H. Anderson, J. R. Ensher, M. R. Matthews, C. E. Wieman, and E. A. Cornell, *Science* **269** (1995).
- [2] A. J. Leggett, *Rev. Mod. Phys.* **73**, 307 (2001).
- [3] C. J. Foot, *Atomic Physics* (Oxford Master Series in atomic, optical and laser physics, Oxford University Press, 2005).
- [4] L. Pitaevskii and S. Stringari, *Bose-Einstein Condensation* (Oxford University Press, 2003).
- [5] S. Rombouts, D. V. Neck, K. Peirs, and L. Pollet, *Mod. Phys. Lett. A* **17**, 1899 (2002).
- [6] M. Greiner, O. Mandel, T. Esslinger, T. Hänsch, and I. Bloch, *Nature* **415**, 39 (2002).
- [7] I. Bloch, *Physics World* **17**, 25 (2004).
- [8] D. Jaksch, C. Bruder, J. I. Cirac, C. W. Gardiner, and P. Zoller, *Phys. Rev. Lett.* **81**, 3108 (1998).
- [9] S. Sachdev, *Quantum Phase Transitions* (Cambridge University Press, 1999).
- [10] H. Moritz, T. Stöferle, M. Köhl, and T. Esslinger, *Phys. Rev. Lett.* **91**, 250402 (2003).
- [11] M. Girardeau, *J. Math. Phys* **1**, 516 (1960).
- [12] B. L. Tolra, K. M. O'Hara, J. H. Huckans, W. D. Phillips, S. L. Rolston, and J. V. Porto, *Phys. Rev. Lett.* **92**, 190401 (2004).

- [13] B. Paredes, A. Widera, V. Murg, O. Mandel, S. F.ölling, I. Cirac, G. V. Shlyapnikov, T. W. Hänsch, and I. Bloch, *Nature* **429**, 277 (2004).
- [14] T. Kinoshita, T. Wenger, and D. Weiss, *Science* **305**, 1125 (2004).
- [15] D. Schrader, I. Dotsenko, M. Khudaverdyan, Y. Miroshnychenko, A. Rauschenbeutel, and D. Meschede, *Phys. Rev. Lett.* **93**, 150501 (2004).
- [16] D. Jaksch, H.-J. Briegel, J. I. Cirac, C. W. Gardiner, and P. Zoller, *Phys. Rev. Lett.* **82**, 1975 (1999).
- [17] C. A. Regal, C. Ticknor, J. L. Bohn, and D. S. Jin, *Nature* **424**, 47 (2003).
- [18] R. Duine and H. T. C. Stoof, *Phys. Rep.* **396**, 115 (2004).
- [19] N. Metropolis, A. W. Rosenbluth, M. N. Metropolis, A. H. Teller, and E. Teller, *J. Chem. Phys.* **21**, 1087 (1953).
- [20] D. M. Ceperley, *Rev. Mod. Phys.* **67**, 279 (1995).
- [21] M. Suzuki, *Prog. of Theor. Phys.* **76**, 1454 (1976).
- [22] W. K. Hastings, *Biometrika* **57**, 97 (1970).
- [23] H. F. Trotter, *Proc. Am. Math. Soc.* **10**, 545 (1959).
- [24] M. Troyer, F. Alet, S. Trebst, and S. Wessel, *AIP Conf. Proc.* **690** (2003), see cond-mat/0306128.
- [25] R. H. Swendsen and J. S. Wang, *Phys. Rev. Lett.* **58**, 86 (1987).
- [26] H. G. Evertz, G. Lana, and M. Marcu, *Phys. Rev. Lett.* **70**, 875 (1993).
- [27] N. V. Prokofev, B. V. Svistunov, and I. S. Tupitsyn, *Pis'ma v Zh. Eks. Theor. Fiz.* **64**, 853 (1996), cond-mat/9612091.
- [28] A. W. Sandvik and J. Kurkijärvi, *Phys. Rev. B* **53**, 5950 (1991).
- [29] A. W. Sandvik, *J. Phys. A* **25**, 3667 (1992).
- [30] D. C. Handscomb, *Proc. Cambridge Philos. Soc.* **60**, 115 (1964).

- [31] N. V. Prokofev, B. V. Svistunov, and I. S. Tupitsyn, JETP Lett. **87**, 310 (1998).
- [32] A. W. Sandvik, Phys. Rev. B **59**, 14157 (1999).
- [33] O. Syljuåsen and A. Sandvik, Phys. Rev. E **66**, 046701 (2002).
- [34] M. Troyer, S. Wessel, and F. Alet, Phys. Rev. Lett. **90**, 120201 (2003).
- [35] C. J. Pethick and H. Smith, *Bose-Einstein Condensation in Dilute Gases* (Cambridge University Press, 2002).
- [36] M. Olshanii, Phys. Rev. Lett. **81**, 938 (1998).
- [37] G. Arfken, *Mathematical methods for Physicists* (Academic Press, Inc., 1985).
- [38] L. Fortunato (2005), private communication.
- [39] B. G. Wybourne, *Classical Groups for Physicists* (John Wiley & Sons, Inc., 1974).
- [40] L. Chaos-Cador and E. Ley-Koo, Revista Mexicana de Física **48**, 67 (2002).
- [41] W. Kohn, Phys. Rev. **115**, 809 (1959).
- [42] M. P. A. Fisher, P. B. Weichman, G. Grinstein, and D. S. Fisher, Phys. Rev. B **40**, 546 (1989).
- [43] D. van Oosten, P. van der Straten, and H. T. C. Stoof, Phys. Rev. A **63**, 053601 (2001).
- [44] A. Kuklov, N. Prokofev, and B. Svistunov, Phys. Rev. Lett. **92**, 030403 (2004).
- [45] A. B. Kuklov and B. V. Svistunov, Phys. Rev. Lett. **90**, 100401 (2004).
- [46] L. Balents, L. Bartosch, A. Burkov, S. Sachdev, and K. Sengupta (2005), cond-mat/0504692.
- [47] A. J. Leggett, Rev. Mod. Phys. **71**, 318 (1999).
- [48] R. Roth and K. Burnett, Phys. Rev. A **68**, 023604 (2003).
- [49] N. D. Mermin and H. Wagner, Phys. Rev. Lett. **17**, 1133 (1966).
- [50] V. L. Berezinskii, Sov. Phys. JETP **32**, 493 (1970).

- [51] J. M. Kosterlitz and D. J. Thouless, *J. Phys. C* **6**, 1181 (1973).
- [52] F. Alet and E. Sørensen, *Phys. Rev. B* **70**, 024513 (2004).
- [53] J. W. Negele and H. Orland, *Quantum Many-Particle Systems* (Addison-Wesley, 1998).
- [54] F. D. M. Haldane, *Phys. Rev. Lett.* **45**, 1358 (1980).
- [55] F. D. M. Haldane, *Phys. Rev. Lett.* **47**, 1840 (1981).
- [56] T. Giamarchi, *Quantum Physics in One Dimension* (Oxford University Press, 2004).
- [57] D. Senechal (1999), [cond-mat/9908262](https://arxiv.org/abs/cond-mat/9908262).
- [58] M. A. Cazalilla, *Journal of Physics B: AMOP* **37**, 1 (2004).
- [59] E. H. Lieb and W. Liniger, *Phys. Rev.* **130**, 1605 (1963).
- [60] P. Jordan and E. P. Wigner, *Z. Phys.* **47**, 631 (1928).
- [61] M. A. Cazalilla, *Phys. Rev. A* **70**, 041604 (2004).
- [62] M. D. Girardeau and E. M. Wright, *Laser Physics* **12**, 8 (2002).
- [63] M. A. Cazalilla, *Phys. Rev. A* **67**, 053606 (2003).
- [64] K. G. Wilson, *Rev. Mod. Phys.* **47**, 773 (1975).
- [65] J. W. Bray and S. T. Chui, *Phys. Rev. B* **19**, 4876 (1979).
- [66] R. Bulla, N.-H. Tong, and M. Vojta, *Phys. Rev. Lett.* **91**, 170601 (2003).
- [67] K. Sheshadri, H. R. Krishnamurthy, R. Pandit, and T. V. Ramakrishnan, *Europhys. Lett.* **22**, 257 (1993).
- [68] S. R. White, *Phys. Rev. Lett.* **69**, 2863 (1992).
- [69] U. Schollwöck, *Rev. Mod. Phys.* **77** (2005), to appear.
- [70] S. R. White and R. M. Noack, *Phys. Rev. Lett.* **68**, 3847 (1992).

- [71] S. R. White, *Phys. Rev. B* **48**, 10345 (1993).
- [72] T. D. Kühner, S. R. White, and H. Monien, *Phys. Rev. B* **61**, 12474 (2000).
- [73] N. Elstner and H. Monien, *Phys. Rev. B* **59**, 12184 (1999).
- [74] G. G. Batrouni, V. Rousseau, R. T. Scalettar, M. Rigol, A. Muramatsu, P. J. H. Denteneer, and M. Troyer, *Phys. Rev. Lett.* **89**, 117203 (2002).
- [75] S. Bergkvist, P. Henelius, and A. Rosengren, *Phys. Rev. A* **70**, 053601 (2004).
- [76] N. Prokof'ev and B. Svistunov, *Phys. Rev. Lett.* **92**, 015703 (2004).
- [77] J. K. Freericks and H. Monien, *Europhys. Lett.* **26**, 545 (1994).
- [78] V. A. Kashurnikov, N. V. Prokof'ev, and B. V. Svistunov, *Phys. Rev. A* **66**, 031601 (2002).
- [79] C. Kollath, U. Schollwöck, J. von Delft, and W. Zwerger, *Phys. Rev. A* **69**, 031601 (2004).
- [80] S. Wessel, F. Alet, M. Troyer, and G. Batrouni, *Phys. Rev. A* **70**, 053615 (2004).
- [81] G. H. Golub and C. F. V. Loan, *Matrix Computations* (The John Hopkins University Press, 1989).
- [82] ALPS collaboration (2004), [cond-mat/0410407](https://arxiv.org/abs/cond-mat/0410407).
- [83] J. S. Liu, *Monte Carlo Strategies in Scientific Computing* (Springer Verlag, 2001).
- [84] M. E. J. Newman and G. T. Barkema, *Monte Carlo Methods in Statistical Physics* (Oxford University Press, 1999).
- [85] S. M. A. Rombouts, Ph.D. thesis, Ghent University (1997), see <http://allserv.ugent.be/~srombout/thesis.ps.gz>.
- [86] P. H. Peskun, *Biometrika* **60**, 607 (1973).
- [87] J. S. Liu, *Statistics and Computing* **6**, 113 (1996).
- [88] J. S. Liu, *Biometrika* **83**, 681 (1996).

- [89] A. Frigessi, C. R. Hwang, and L. Younes, *Ann. of Appl. Prob.* **2**, 610 (1992).
- [90] P. Dayal, S. Trebst, S. Wessel, D. Würtz, M. Troyer, S. Sabhapandit, and S. N. Coppersmith, *Phys. Rev. Lett.* **92**, 097201 (2004).
- [91] S. Trebst (2004), private communication.
- [92] B. Berche and C. Chatelain, in *Order, Disorder and Criticality*, edited by Y. Holovatch (World Scientific, Singapore, 2004), see cond-mat/0207421.
- [93] U. Wolff, *Phys. Rev. Lett.* **62**, 361 (1989).
- [94] O. Syljuåsen, *Phys. Rev. E* **67**, 046701 (2003).
- [95] S. Wessel, Ph.D. thesis, University of Southern California (2001).
- [96] F. Alet, S. Wessel, and M. Troyer, *Phys. Rev. E* **71**, 036706 (2005).
- [97] W. H. Press, B. P. Flannery, S. A. Teukolsky, and W. T. Vetterling, *Numerical Recipes in C: The Art of Scientific Computing* (Cambridge University Press, 1992).
- [98] E. L. Pollock and D. M. Ceperley, *Phys. Rev. B* **36**, 8343 (1987).
- [99] A. Dorneich and M. Troyer, *Phys. Rev. E* **64**, 066701 (2001).
- [100] N. Kawashima and K. Harada, *J. Phys. Soc. Jpn.* **73**, 1379 (2004).
- [101] F. D. Haldane, *Phys. Rev. Lett.* **50**, 1153 (1983).
- [102] F. D. Haldane, *Phys. Lett.* **93 A**, 464 (1983).
- [103] S. Wessel, F. Alet, S. Trebst, D. Leumann, M. Troyer, and G. G. Batrouni (2004), cond-mat/0411473.
- [104] G. E. Astrakharchik, D. Blume, S. Giorgini, and B. E. Giorgini, *J. Phys. B: At. Mol. Opt. Phys.* **37**, 205 (2004).
- [105] G. E. Astrakharchik, J. Boronat, J. Casulleras, and S. Giorgini (2004), cond-mat/0405225.

- [106] C. Buggle, J. Leonard, W. von Klitzing, and J. T. M. Walraven, *Phys. Rev. Lett.* **93**, 173202 (2004).
- [107] L. Pollet, S. M. A. Rombouts, K. V. Houcke, and K. Heyde, *Phys. Rev. E* **70**, 056705 (2004).
- [108] M. Olshanii and D. Dunjko, *Phys. Rev. Lett.* **91**, 090401 (2003).
- [109] G. E. Astrakharchik and S. Giorgini, *Phys. Rev. A* **68**, 031602 (2003).
- [110] L. Pollet, S. Rombouts, K. Heyde, and J. Dukelsky, *Phys. Rev. A* **69**, 043601 (2004).
- [111] M. Troyer (2004), private communication.
- [112] D. M. Gangardt, P. Pedri, L. Santos, and G. V. Shlyapnikov (2004), [cond-mat/0408437](https://arxiv.org/abs/cond-mat/0408437).
- [113] W. Krauth, *Phys. Rev. B* **44**, 9772 (1991).
- [114] V. A. Kashurnikov and B. V. Svistunov, *Phys. Rev. B* **53**, 11776 (1996).
- [115] V. A. Kashurnikov, A. V. Krasavin, and B. V. Svistunov, *Pis'ma Zh. Eksp. Theo. Fiz.* **64**, 92 (1996), see *JETP Lett.* **64**, 99 (1996).
- [116] V. F. Elesin, V. A. Kashurnikov, and L. A. Openov, *Pis'ma Zh. Eksp. Theo. Fiz.* **60**, 174 (1994), see *JETP Lett.* **60**, 177 (1994).
- [117] K. Harada and N. Kawashima, *J. Phys. Soc. Jpn.* **67**, 2678 (1998).
- [118] M. Troyer and S. Sachdev, *Phys. Rev. Lett.* **81**, 5418 (1998).
- [119] R. Roth and K. Burnett, *Phys. Rev. A* **69**, 021601 (2004).
- [120] M. Lewenstein, L. Santos, M. A. Baranov, and H. Fehrmann, *Phys. Rev. Lett.* **92**, 050401 (2004).
- [121] M. A. Cazalilla and A. F. Ho, *Phys. Rev. Lett.* **91**, 150403 (2003).
- [122] L. Mathey, D.-W. Wang, W. Hofstetter, M. D. Lukin, and E. Demler, *Phys. Rev. Lett.* **93**, 120404 (2004).

[123] E. Pazy and A. Vardi (2004), `cond-mat/0408269`.

[124] R. Shankar, *Rev. Mod. Phys.* **66**, 129 (1994).